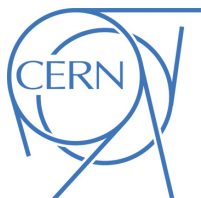




ATLAS Note

ANA-HDBS-2020-09-INT1

30th November 2022



Draft version 0.1

1

2 Search for $t\bar{b}$ resonance using boosted top-quark 3 topology in the lepton+jets final state at $\sqrt{s} = 13$ 4 TeV with the ATLAS detector

5

De La Torre Perez, Hector^a, Gombas, Jason Peter^a, Schwienhorst, Reinhard^a,
6 Sato, Koji^b, Hirose, Shigeki^b, Yamauchi, Hiroki^b, Salvador Salas, Adrian^c, Riu,
7 Imma^c, Mir Martinez, Lluisa Maria^c

8

^a*Michigan State University (US)*

9

^b*University of Tsukuba (JP)*

10

^c*The Barcelona Institute of Science and Technology (BIST) (ES)*

11

A search for $t\bar{b}$ resonances with a boosted top tagging technique is presented, focusing on a final state consisting of a single charged lepton and multiple jets as well as a top-tagged large- R jet. The analysis is based on the pp collision data at the centre-of-mass energy of 13 TeV collected with the ATLAS detector with an integrated luminosity of 139 fb^{-1} . As a hypothetical particle with spin-0(1), a charged Higgs boson (a W' boson) scenario is searched in the mass range from 1 TeV up to 5 TeV.

17

© 2022 CERN for the benefit of the ATLAS Collaboration.

18

Reproduction of this article or parts of it is allowed as specified in the CC-BY-4.0 license.

19 **Contents**

20	1 Object Reconstruction	6
21	1.1 Electrons	6
22	1.2 Muons	6
23	1.3 Taus	6
24	1.4 Small- R jets and b -tagging	6
25	1.5 Large- R jets and top-tagging	7
26	1.6 Overlap Removal	7
27	2 Analysis Strategy	9
28	2.1 Event Selection	9
29	2.1.1 Signal region (SR)	9
30	2.1.2 Control region (CR)	10
31	2.1.3 Summary	11
32	2.2 Multivariable analysis using BDT	12
33	2.2.1 Signal and background definition in BDT training	12
34	2.2.2 BDT training settings	13
35	2.2.3 Input variables in BDT	14
36	2.2.4 Results of BDT training	16
37	3 Background modeling	22
38	3.1 Blind strategy	22
39	3.2 Data/MC comparison for BDT input variables	22
40	3.3 Data/MC comparison for BDT distributions	24
41	3.4 Reweighting technique	28
42	4 Systematics Uncertainties	35
43	4.1 Luminosity and pile-up modeling	35
44	4.1.1 Luminosity	35
45	4.1.2 Pile-up modeling	35
46	4.2 Reconstructed objects	35
47	4.2.1 Charged leptons	35
48	4.2.2 Small- R jets, Large- R jets	37
49	4.3 Signal modeling	39
50	4.3.1 H^+ signal	39
51	4.4 Background modeling	39
52	4.4.1 $t\bar{t}$ +jets	39
53	4.4.2 Other backgrounds	41
54	5 Profile Likelihood Fit (Without reweighting)	43
55	5.1 Method	43
56	5.2 Pruning and smoothing of systematic uncertainties	43
57	5.3 Asimov fit results	44
58	5.4 Post-fit plots for Asimov fit	61
59	5.5 Asimov fit results summary	65
60	5.6 Upper cross-section limits as a function of the H^+ mass	66

61	Appendices	71
62	A TOPQ1 DAOD list	71
63	A.1 Data	71
64	A.2 $\bar{t}bH^+$	71
65	A.3 $t\bar{t}$ + jets	71
66	A.4 $t\bar{t}H$	72
67	A.5 $t\bar{t}V$	73
68	A.6 Single top	73
69	A.7 tH	74
70	A.8 Rare t processes	74
71	A.9 Vector bosons plus jets	74
72	A.9.1 W + jets	74
73	A.9.2 Z + jets	75
74	A.10 Diboson	77
75	B Signal/background comparisons	78
76	B.1 BDT input variables	78
77	B.2 BDT output	80
78	B.3 H_T^{jets} distribution in CR	86
79	C Pruning	87
80	C.1 Asimov fit	87
81	D Studies for systematic uncertainties	95
82	D.1 Systematics for the composition ratio of $t\bar{t}$ + HF events	95

83 List of contributions

De La Torre Perez, Hector	W' vs H+ comparisons, W' generation
Gombas, Jason Peter	W' NLO model, W' vs H+ comparisons, W' generation
Schwienhorst, Reinhard	W' NLO model, Jason supervision
Sato, Koji	Analysis contact, supervision of Hiroki
Hirose, Shigeki	Analysis contact, ntuple production, BDT training, MC production, supervision of Hiroki
84 Yamauchi, Hiroki	Main analyser: ntuple production, fit studies and limits extraction
Salvador Salas, Adrian	Main analyser of resolved analysis, providing technical support; ntuple production
Riu, Imma	Signal AODs and TOPQ1s production; provision of other technical support from resolved analysis
85 Mir Martinez, Lluisa Maria	Monte Carlo production

86 **Remaining to do**

87 **The reweighting method:** A complete proposal is to be discussed at the EB request (HBSM meeting) on
88 21st July, and incorporate comments and discussions there for the method, summarize them in the
89 note in 1-2 weeks after the meeting.

90 **W' MC production:** Validations are to be finalized by the end of July so that the MC generator can be
91 implemented into the ATLAS official software. We aim for finishing the MC production as well as
92 limit evaluations by the end of September. This is to be done in parallel to EB review, as agreed with
93 the HBSM / HDBS conveners.

94 **Theoretical interpretation:** Interpret limits in terms of the theoretical H+/W' scenarios, such as hMSSM
95 and XXX. This will be done by the end of September.

96 **Version log with major updates:**

97 **v1.1:**

- 98 • Filled the Section 3.4 that describes the reweighting technique.
99 • Added the Figures 64(a) to 64(j) in Appendix B.2 to show BDT output distributions of events used
100 for deriving reweighting factors.
101 • Updated the Table 11 and the Section 4.4 with the systematics source of $t\bar{t}$ + jets reweighting included.
102 (The original Section 5.4 that describes the reweighting systematics sources was put into the Section
103 4.4)

104 1 Object Reconstruction

105 1.1 Electrons

106 Electrons are reconstructed from energy clusters in the electromagnetic calorimeter matched to tracks
 107 reconstructed in the inner detector (ID) [1, 2], and are required to have $p_T > 10$ GeV and $|\eta| < 2.47$.
 108 Candidates in the barrel–endcap transition region of the calorimeter ($1.37 < |\eta| < 1.52$) are excluded.
 109 Electrons must satisfy the *tight* identification criterion based on a likelihood discriminant described in
 110 Ref. [2] and the following constraints in the longitudinal and transverse impact parameters: $|z_0| < 0.5$ mm
 111 and $|d_0|/\sigma_{d_0} < 5$. The impact parameters are defined with respect to beam line. Electrons are required to
 112 satisfy the *FCTight* isolate criteria [3].

113 1.2 Muons

114 Muons are reconstructed from either track segments or full tracks in the muon spectrometer which are
 115 matched to tracks in the ID [4]. Tracks are then re-fitted using information from both detector system.
 116 Muons are required to have $p_T > 10$ GeV and $|\eta| < 2.5$ and the following constraints in the longitudinal
 117 and transverse impact parameters: $|z_0| < 0.5$ mm and $|d_0|/\sigma_{d_0} < 3$. Muons should satisfy the *medium*
 118 identification and the *FCTightTrackOnly* isolation criteria [3].

119 1.3 Taus

120 Hadronically decaying tau leptons (τ_{had}) are distinguished from jets using the track multiplicity and the
 121 τ_{had} identification algorithm based on a recurrent neural network [5]. This algorithm exploits the track
 122 collimation, jet substructure, kinematic information and so son. These τ_{had} candidates are required to have
 123 $p_T > 25$ GeV, $|\eta| < 2.5$ and pass the *Medium τ* -identification working point. Although taus are not used in
 124 the analysis, the consistent configuration with the resolved analysis as well as the $t\bar{t}H(\rightarrow bb)$ analysis is
 125 kept.

126 1.4 Small- R jets and b -tagging

127 Jets are reconstructed using the anti- k_t clustering algorithm [6] on particle-flow objects [7] with a radius of
 128 $R = 0.4$. Jets are calibrated using the standard jet calibration procedure, which corrects the jet nergy to
 129 match on average the true jet energy at particle level and applies an in-situ correction for data [8]. The
 130 jet collection name in ATLAS is `AntiKt4EMPF1lowJets_BTagging201903`. Jets are required to have
 131 $|\eta| < 2.5$ such that they are within the acceptance of the ID and the recommended jet vertex tagging (JVT)
 132 requirement [9] is applied to jets with $p_T < 60$ GeV in order to remove jets originating from pile-up.

133 Small- R jets originating from the hadronisation of b -quarks (referred to as b -jets hereafter) are identified
 134 using an algorithm based on multivariate techniques to combine information from the impact parameters
 135 of displaced tracks as well as properties of secondary and tertiary decay vertices reconstructed within the
 136 jets. In this analysis, b -tagging relies on the *DL1r* tagger [10], trained on simulated $t\bar{t}$ events, and the event
 137 selection makes use of jets b -tagged with the *DL1r* algorithm at the 70% efficiency working point.

138 1.5 Large-*R* jets and top-tagging

139 Top quarks with high transverse momentum ($p_T \gtrsim 2m_t$) are expected to result in decay products that are
 140 collimated. For top quarks decaying hadronically (bqq'), the three quarks may not be resolved as three
 141 separate jets. In order to reconstruct these boosted hadronically-decaying top quarks, large-radius (large-*R*)
 142 jets are used. The large-*R* jets are formed from the topological clusters of calorimeter cells which are
 143 calibrated to the hadronic energy scale using the local calibration weighting method [11], and reconstructed
 144 using the anti- k_t algorithm with radius parameter of $R = 1.0$. The jet collection name in ATLAS is
 145 `AntiKt10LCTopoTrimmedPtFrac5SmallR20Jets`. These jets are further trimmed to remove the effects
 146 of pile-up and underlying event. The trimming [12] is done by reclustering the original constituents of a
 147 large-*R* jet into a collection of R_{sub} subjets using k_t algorithm [13]. The subjets are then discarded if they
 148 carry less than a specific fraction (f_{cut}) of the p_T of the original large-*R* jet. In this analysis, the optimized
 149 values ($R_{\text{sub}} = 0.2$, $f_{\text{cut}} = 5\%$) are used [14]. The large-*R* jet energy and mass scale are then calibrated
 150 using correction factors derived from simulation. The mass of the large-*R* jets is calculated using tracking
 151 and calorimeter information, so called combined mass technique [15]. Only the large-*R* jets that satisfy
 152 $200 < p_T < 3000 \text{ GeV}$, $|\eta| < 2.0$ and $40 < m_{\text{comb}} < 600 \text{ GeV}$ are considered in this analysis.

153 The identification of hadronically decaying top quarks that are reconstructed as large-*R* jets is performed
 154 using a multivariate classification algorithm employed in a deep neural network [16]. In the kinematic
 155 region of interest in this search, a single large-*R* jet captures the top quark decay products, resulting in a
 156 characteristic multi-core structure within the jet, in contrast to a typical single-core structure associated
 157 with jets in multijet. In order to exploit this characteristic behaviour for the top quark identification, a
 158 multivariate top-tagging classifier was developed. The tagger uses multiple jet-level discriminants as
 159 inputs, such as calibrated jet p_T and mass, information about the dispersion of the jet constituents such as
 160 N -subjettiness [17], splitting scales [18] and energy correlation functions [19].

161 Top-tagging, associated scale factors and uncertainties are only provided for jets with $350 < p_T < 2500$
 162 GeV. The tagger used is optimized for the contained top definition, in which the signal category is defined
 163 using jets matched to a truth top quark. In addition, a truth jet matched to the reconstructed jet is required
 164 to have a mass above 140 GeV and at least one *b*-hadron ghost matched to it.

165 In this analysis, large-*R* jets which pass the 80% efficiency working point of the contained top-tagging
 166 criterion ($J_{\text{top-tagged}}$) are chosen as the boosted top candidates. Especially, the leading boosted top candidate
 167 out of them is represented by $J_{\text{top-tagged}}^{\text{1st}}$ in the following sections.

168 1.6 Overlap Removal

169 In order to avoid counting a single detector response as more than one lepton or jet, the following overlap
 170 removal procedure is applied.

171 To prevent double-counting of electron energy deposits as jets, the small-*R* jet within $\Delta R_y = \sqrt{(\Delta y)^2 + (\Delta \phi)^2} =$
 172 0.2 of a selected electron is removed. Here, the rapidity is defined as $y = \frac{1}{2} \ln \frac{E+p_z}{E-p_z}$, where E is the energy
 173 and p_z is the longitudinal component of the momentum along the beam pipe. If the nearest small-*R* jet

¹⁷⁴ surviving that selection is within $\Delta R_y = 0.4$ of the electron, the electron is discarded. In the case that a
¹⁷⁵ large- R jet is found within $\Delta R = 1.0$ of the electron, the large- R jet is removed.¹

¹⁷⁶ Muons are removed if their distance from the nearest small- R jet is within $\Delta R_y < 0.4$. This treatment
¹⁷⁷ reduces the background from heavy-flavor decays inside small- R jets. However, if this small- R jet has
¹⁷⁸ fewer than three associated tracks, the muon is kept and the small- R jet is removed instead. This avoids an
¹⁷⁹ inefficiency for high-energy muons undergoing significant energy loss in the calorimeter.

¹⁸⁰ A τ_{had} candidate is rejected if it is within $\Delta R_y < 0.2$ from any selected electron or muon. Also, small- R
¹⁸¹ jets with $\Delta R_y < 0.2$ around a τ_{had} candidate are rejected. The overlap removal with τ_{had} is applied in order
¹⁸² to keep consistency with the $t\bar{t}H(\rightarrow bb)$ analysis as well as the $H^+ \rightarrow tb$ analysis.

¹⁸³ Small- R jets within $\Delta R < 1.0$ of a leading top-tagged large- R jet are removed⁶ to prevent double-counting
¹⁸⁴ of jet energy deposits.

¹⁸⁵ All of the above overlap removal procedures are summarized in Table 1.

Reject	Against	Criteria
Small- R jet	Electron	$\Delta R_y < 0.2$
Electron	Small- R jet	$0.2 < \Delta R_y < 0.4$
Small- R jet	Muon	$N_{track} < 3$ in jet and $\Delta R_y < 0.4$
Muon	Small- R jet	$\Delta R_y < 0.4$
τ_{had}	Electron	$\Delta R_y < 0.2$
τ_{had}	Muon	$\Delta R_y < 0.2$
Small- R jet	τ_{had}	$\Delta R_y < 0.2$
Large- R jet	Electron	$\Delta R < 1.0$
Small- R jet	Leading top-tagged large- R jet	$\Delta R < 1.0$

Table 1: Summary of overlap removal procedures in this analysis.

¹ Following the recommendation for ATLAS analyses in Run 2 [20], the overlap removal implemented in the *AssociationUtils* package [21] is based on ΔR_y . It is found more appropriate in the case of non-massless objects [22]. However, overlap removal for large- R jets is performed in the ttHOffline software, and is computed based on ΔR .

186 2 Analysis Strategy

187 2.1 Event Selection

188 In this analysis, two regions, “Signal region (SR)” and “Control region (CR)”, are defined according to the
 189 number of lepton, top tagged large- R jets and b -tagged small- R jets as following.

190 2.1.1 Signal region (SR)

191 Figure 1 show the schematic of boosted event topology in case of $H^+ \rightarrow tb$ event. An signal event is
 192 expected to have one $J_{\text{top-tag}}$, three b -jets and one lepton+MET. However, the b -jet originated from the
 193 gluon is typically not detected, because it tend to fly in the forward directions and therefore outside the
 194 detector acceptance. Threfore, at least two b -jets are required in this analysis.

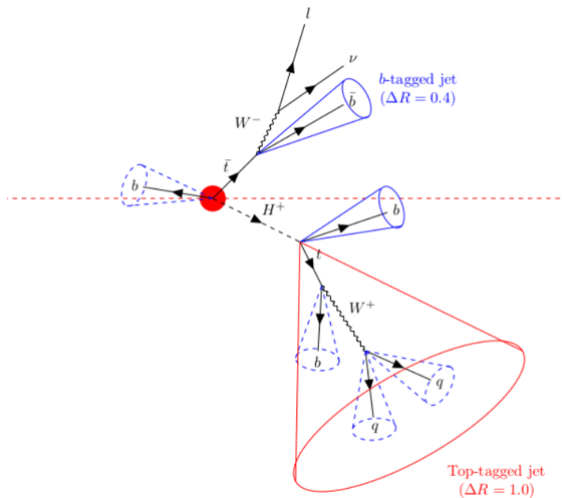


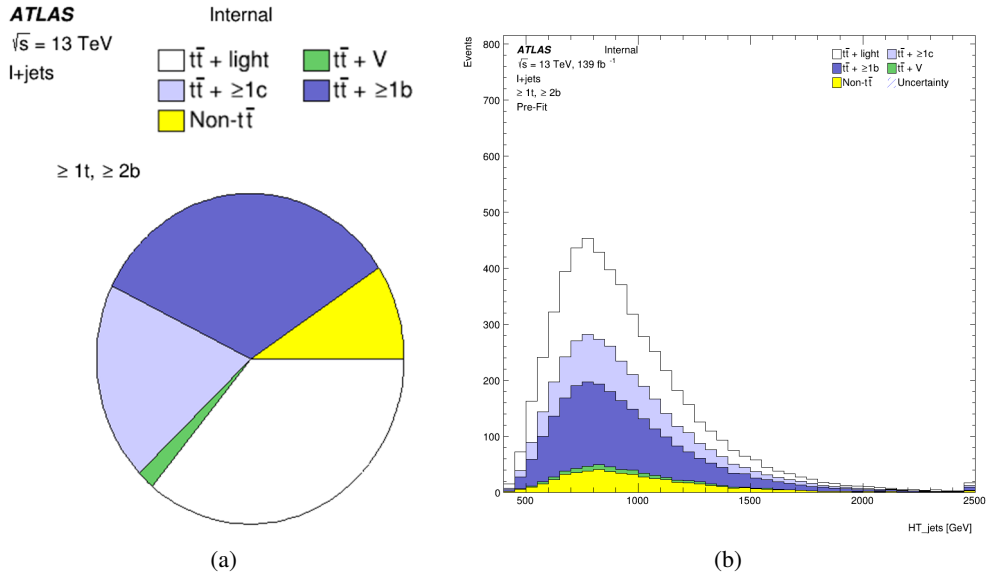
Figure 1: Schematic of boosted event topology. Signal event has at least one $J_{\text{top-tag}}$ and at least two b -tagged small- R jets.

195 To be consistent with the signal event as shown in Figure ??, events are required to have exactly one lepton
 196 (e or μ) that is matched to the one firing one of the single lepton triggers. Events are also required to have at
 197 least one top-tagged large- R jet and at least two b -tagged small- R jets. The b -jets must additionally satisfy
 198 $\Delta R(J_{\text{top-tag}}^{1st}, b\text{-jet}) > 1.0$ to ensure these b -jets are not consituent of the leading top-tagged jet. Missing E_T
 199 is not required in this analysis. These selections are summarized in Table 2.

Cut	Criteria
leptons	Exactly 1 lepton in event
	<u>Electron</u> <u>Muon</u>
	$p_T > 27 \text{ GeV}$ $p_T > 27 \text{ GeV}$
	$ \eta < 1.37 \text{ or } 1.52 < \eta < 2.47$ $ \eta < 2.5$
Top-tagged large- R jets	≥ 1 top-tagged large-R jets
	$350 \text{ GeV} < p_T < 2500 \text{ GeV}$
	$ \eta < 2.0$
b -tagged small- R jets	≥ 2 b-tagged small-R jets
	$p_T > 25 \text{ GeV}$
	$ \eta < 2.5$
	$\Delta R(J_{\text{top-tag}}^{1\text{st}}, b\text{-jet}) > 1.0$

Table 2: Event selections in the SR.

Events passing the event selections in Table 2 are expected to have the boosted-topology as shown in Figure ???. The expected background composition and distributions in the SR is illustrated in Figure 2. Events containing $t\bar{t}$ fully dominate the SR. In this figure, H_T^{jet} denotes the sum of p_T of $J_{\text{top-tag}}^{1\text{st}}$ and all small- R jets in event, and enhances the characteristics of the signal events which have high p_T jets from the heavy H^+ decay. Table ?? shows the cut flow for each signal sample.

Figure 2: Background composition in the SR is shown in the pie chart (a) and the H_T^{jets} distributions (b).

2.1.2 Control region (CR)

In order to constrain the yields of events with $t\bar{t}$ in association with at least one light-flavor jet, a dedicated control region (CR) is prepared. Requirements in the CR are identical to that in the SR, except the number of b -tagged small- R jets. Exactly one b -tagged small- R jet is required in the CR in order to keep orthogonality

209 to the SR where two or more b -tagged small- R jets are required. The selections in the CR are summarized
 210 in Table 3.

Cut	Criteria
leptons	Same as in the SR
Top-tagged large- R jets	Same as in the SR
b -tagged small- R jets	Exactly one b -tagged small- R jet Other kinematic requirements are the same as in the SR

Table 3: Event selections in the CR.

211 After applying the event selections for the CR, the events mostly contain $t\bar{t}$ in association with at least one
 212 light-flavor jet. The background composition is illustrated in Figure 3. This CR is included in the profile
 213 likelihood fit discussed in Section 5.

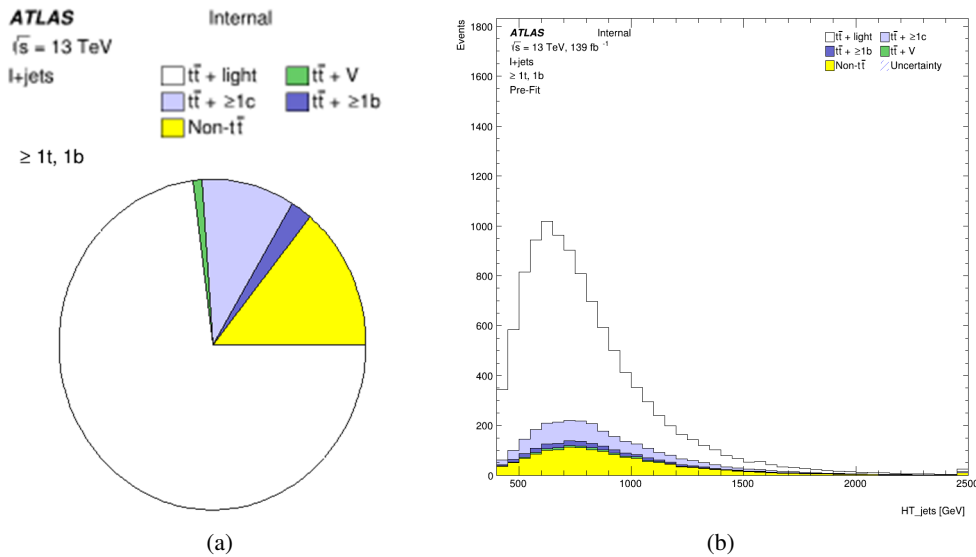


Figure 3: Background composition in the CR is shown in the pie chart (a) and the H_T^{jets} distributions (b).

2.1.3 Summary

214 The number of expected signal and background events in the SR and CR are shown in Table 4.
 215 The predicted number of H^+ signal events for the 1000 and 3000 GeV mass hypothesis assume
 216 $\sigma(pp \rightarrow tbH^+) \times Br(H^+ \rightarrow tb) = 0.046\text{pb}$. This is the upper limit at $M_{H^+} = 1000$ GeV obtained from
 217 the resolved analysis, the largest upper limit from the resolved analysis in the mass range $1000 \geq M_{H^+} \geq 2000$
 218 GeV where both resolved and our boosted analyses search for H^+ . We use the signal $\sigma \times Br$ in the decision
 219 of blinded regions.
 220

	SR	CR
$t\bar{t}$ + light	1979 ± 89	7848 ± 329
$t\bar{t}+ \geq 1c$	1070 ± 56	1052 ± 38
$t\bar{t}+ \geq 1b$	1840 ± 84	246 ± 11
$t\bar{t} + W$	38 ± 20	52 ± 27
$t\bar{t} + Z$	67 ± 34	49 ± 6
Wt channel	183 ± 93	422 ± 212
t channel	37 ± 3	63 ± 5
Other top sources	38 ± 15	11 ± 1
$VV, V+jets$	152 ± 55	1001 ± 342
$t\bar{t}H$	103 ± 4	18 ± 0
Total	5565 ± 256	10763 ± 566
H^+ 1000 GeV	58 ± 6	4 ± 0
H^+ 3000 GeV	67 ± 16	13 ± 3

Table 4: Number of expected and selected events split according to the analysis region. The quoted uncertainties include both statistical and systematic uncertainties before fitting.

221 2.2 Multivariable analysis using BDT

222 In this search, the most important background is $t\bar{t}$ + jets as discussed in Section 2.1.1. To enhance
 223 separation between signal and background, multivariable analysis is performed using Boosted Decision
 224 Trees (BDT) technique of TMVA [23]. Obtained BDT score distribution is used in the profile likelihood fit
 225 as a final discriminant (Section 5).

226 2.2.1 Signal and background definition in BDT training

227 To classify H^+ signal and $t\bar{t}$ + jets background events, BDTs are trained using the simulated H^+ signal and
 228 $t\bar{t}$ + jets background samples, as summarized in Table 5. Ten different H^+ mass hypotheses are considered
 229 in this analysis, and the training is performed on each H^+ mass hypothesis. On the other hand, the $t\bar{t}$ + jets
 230 background samples are common in each training. Since kinematics of H^+ signals become harder in higher
 231 mass hypotheses, as shown in Section 2.2.3, the BDTs trained using the higher H^+ mass samples typically
 232 have greater separation power.

H^+ mass point [GeV]	DSIDs
1000	450004
1200	450598
1400	450599
1600	450600
1800	450601
2000	450602
2500	451490
3000	451491
4000	508710
5000	508711

(a)

$t\bar{t} + \text{jets}$ sample type	DSIDs
Inclusive	410470, 410471
BBFilter	411073, 411076
BFilterBBVeto	411074, 411077
CFilterBVeto	411075, 411078

(b)

Table 5: List of signal (a) and background (b) samples used in BDT training. Training is performed on each H^+ mass hypothesis. On the other hand, the $t\bar{t} + \text{jets}$ background samples are common in each training.

2.2.2 BDT training settings

In order to make full use of statistics of simulation samples, we adopt the 4-fold cross-validation method in the BDT training (Figure 4). Each simulation sample is divided into four sub-datasets (Fold1, Fold2, Fold3 and Fold4). For each MC event, a random number is generated with the MC event number as a seed, and the event is categorized into one of the sub-datasets according to the generated number. Two of the four sub-datasets are labeled "TRAIN", which are used for BDT training. One of the other sub-datasets are labeled "VALID", and is used to optimize the BDT performance. The last sample, "TEST", is used to construct a fit template. Four combination of sub-dataset usage (Split1 to Split4 in Figure 4) are tried, and we obtain four statistically-independent BDTs and fit templates. They are combined into one fit template and is used in the profile likelihood fit (Section 5).

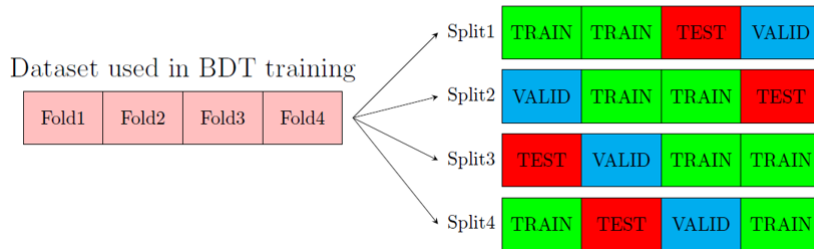


Figure 4: Scheme of 4-fold cross-validation in this analysis.

²⁴³ Hyperparamerters for the BDTs are summarized in Table. 6. Those hyperparameters are chosen to obtain
²⁴⁴ the best sensitivity.

Configuration	
Algorithm	Gradient boosting
<i>Hyperparameters</i>	
NTrees	100
MinNodeSize	2.5
MaxDepth	3
nCuts	20

Table 6: List of hyperparameters used in the trainging of a BDT

²⁴⁵ 2.2.3 Input variables in BDT

²⁴⁶ Jets originating from an H^+ decay have higher p_T comparing with $t\bar{t} + \text{jets}$ events due to its heavy mass.
²⁴⁷ Additionally, correlation among jets are different between H^+ and $t\bar{t} + \text{jets}$ events because H^+ creates a
²⁴⁸ resonance. The BDT is trained in order to fully exploit these kinematic characteristics. List of variables
²⁴⁹ used in BDT training is summarized in Table 7. Any variables for missing E_T are not used in BDT traning.
²⁵⁰ In Figure 5, each distribution in the H^+ sample with a mass of 3000 GeV is compared with the $t\bar{t} + \text{jets}$
²⁵¹ background. Table 8 shows the ranking of these variables.

Symbol	Description
HT_jets	Scalar sum of the transverse energy of all jets
LeadingJet_pt	Leading jet p_T
Mjjj_MaxPt	Invariant mass of the jet triplet with maximum p_T
Mbb_MaxPt	Invariant mass of the b-jet pair with maximum p_T
Muu_MinDR	Invariant mass of the untagged jet-pair with minimum ΔR
dRlepb_MindR	ΔR between the lepton and the pair of b -jets with smallest ΔR
dRbb_avg	Average ΔR between all b -jet pairs in the event
Centrality_all	Centrality calculated using all jets and leptons
H1_all	Second Fox-Wolfram moment calculated using all jets and leptons
LeadingTop_pt	Leading top-tagged jet p_T
LeadingTop_m	Invariant mass of leading top-tagged jet
Pt_tb	p_T of the pair of leading top-tagged jet and leading b -jet
M_tb	Invariant mass of the pair of leading top-tagged jet and leading b -jet
PtAsymm_tb	p_T asymmetry between leading top-tagged jet and leading b -jet

Table 7: List of variables included in the training of the BDT

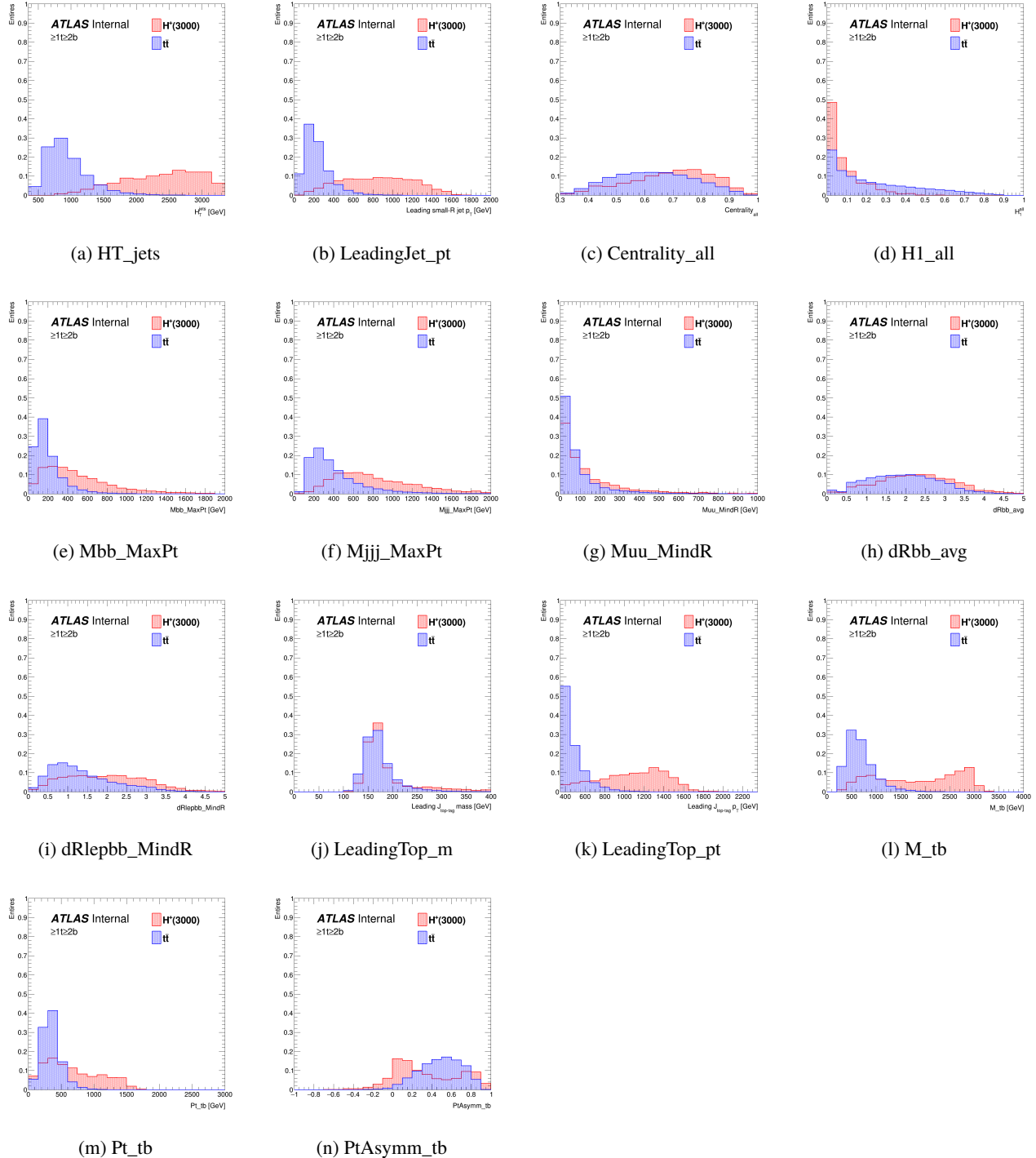


Figure 5: Comparison of input variables for BDT training between H^+ and $t\bar{t} + \text{jets}$ events under $3000 \text{ GeV } H^+$ mass hypothesis.

Ranking	Variable	Importance				Avg.
		Fold1	Fold2	Fold3	Fold4	
1	HT_jets	9.509E-02	1.118E-01	1.216E-01	1.073E-01	1.089E-01
2	Centrality_all	1.053E-01	9.995E-02	1.126E-01	1.012E-01	1.048E-01
3	M_tb	9.192E-02	9.473E-02	8.282E-02	8.014E-02	8.740E-02
4	LeadingTop_pt	8.710E-02	8.107E-02	6.472E-02	7.292E-02	7.645E-02
5	Pt_tb	7.944E-02	7.816E-02	7.888E-02	6.795E-02	7.611E-02
6	LeadingJet_pt	6.180E-02	7.860E-02	6.628E-02	7.577E-02	7.061E-02
7	dRlepb_MindR	6.997E-02	7.842E-02	6.968E-02	6.393E-02	7.050E-02
8	dRbb_avg	6.236E-02	6.435E-02	5.331E-02	7.843E-02	6.461E-02
9	Mbb_MaxPt	5.348E-02	6.657E-02	7.339E-02	5.552E-02	6.224E-02
10	PtAsymm_tb	5.209E-02	6.526E-02	5.843E-02	6.620E-02	6.050E-02
11	Mjjj_MaxPt	6.439E-02	6.248E-02	5.503E-02	5.577E-02	5.942E-02
12	H1_all	6.316E-02	4.577E-02	4.876E-02	6.291E-02	5.515E-02
13	LeadingTop_m	5.868E-02	3.864E-02	5.567E-02	5.748E-02	5.262E-02
14	Muu_MindR	4.438E-02	3.422E-02	5.889E-02	5.439E-02	4.797E-02

Table 8: Importance ranking of variables used in BDT training on 3000 GeV H^+ mass hypothesis. Importance values are output from TMVA.

2.2.4 Results of BDT training

The BDT output distributions for signal and background in the analysis region for different values of the H^+ mass are shown in Figure 6 to 13, together with receiver operating characteristic (ROC) curves.

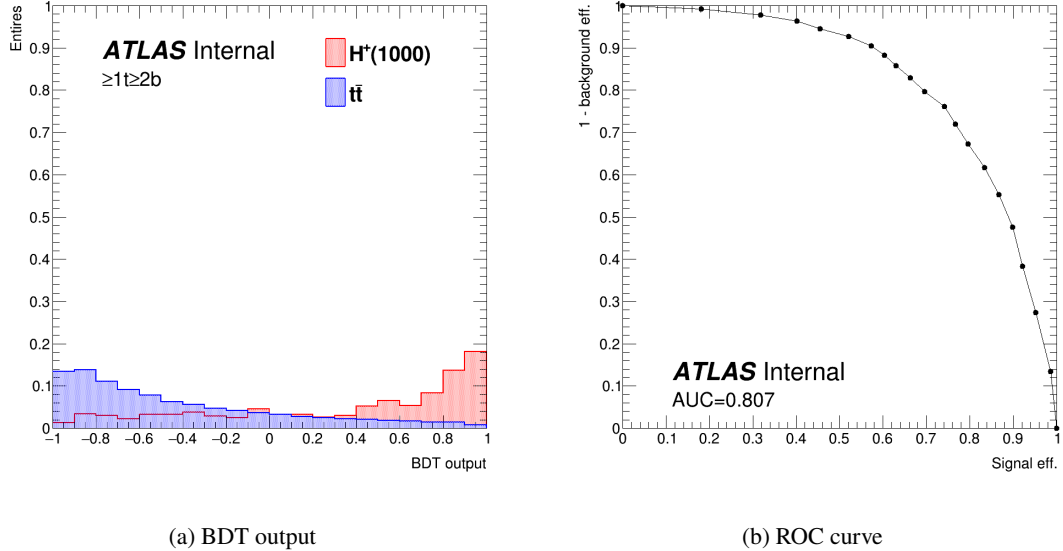


Figure 6: BDT distribution and ROC curve for the 1000 GeV H^+ mass hypothesis.

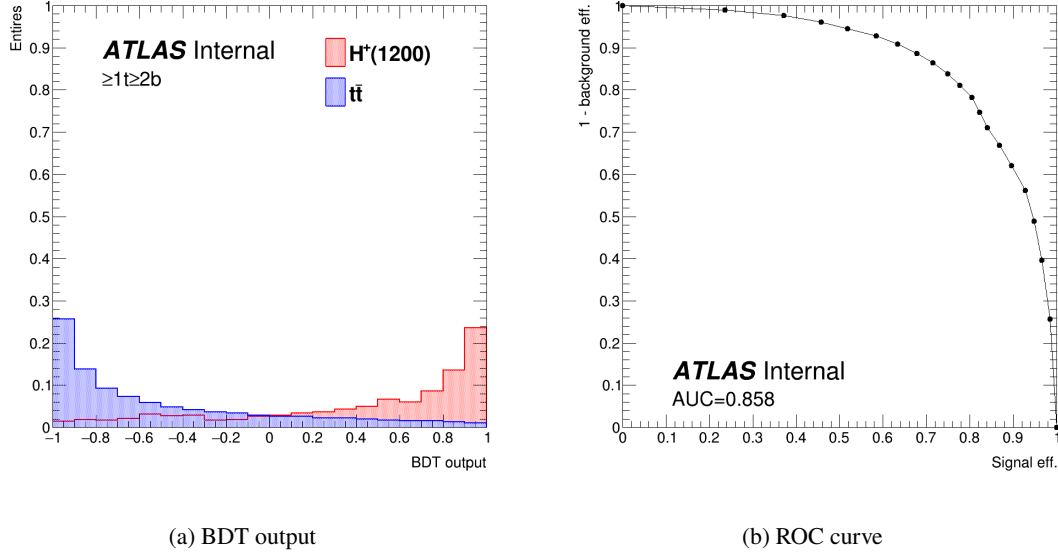


Figure 7: BDT distribution and ROC curve for the 1200 GeV H^+ mass hypothesis.

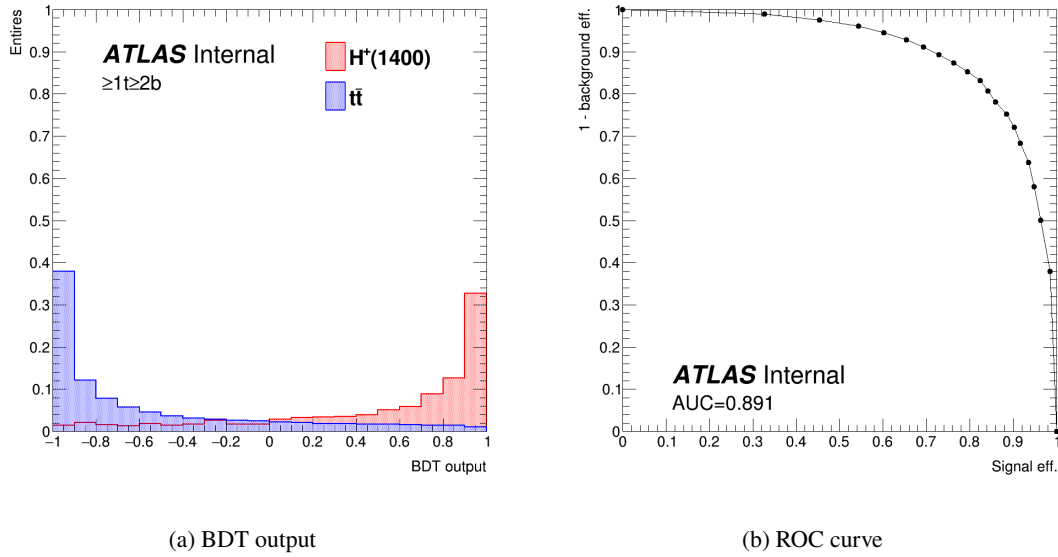


Figure 8: BDT distribution and ROC curve for the 1400 GeV H^+ mass hypothesis.

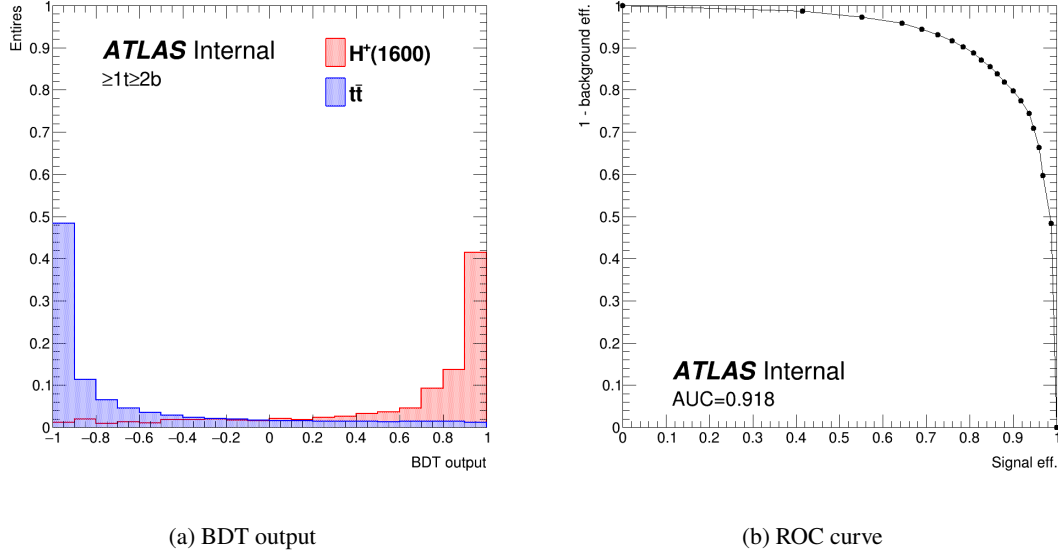


Figure 9: BDT distribution and ROC curve for the 1600 GeV H^+ mass hypothesis.

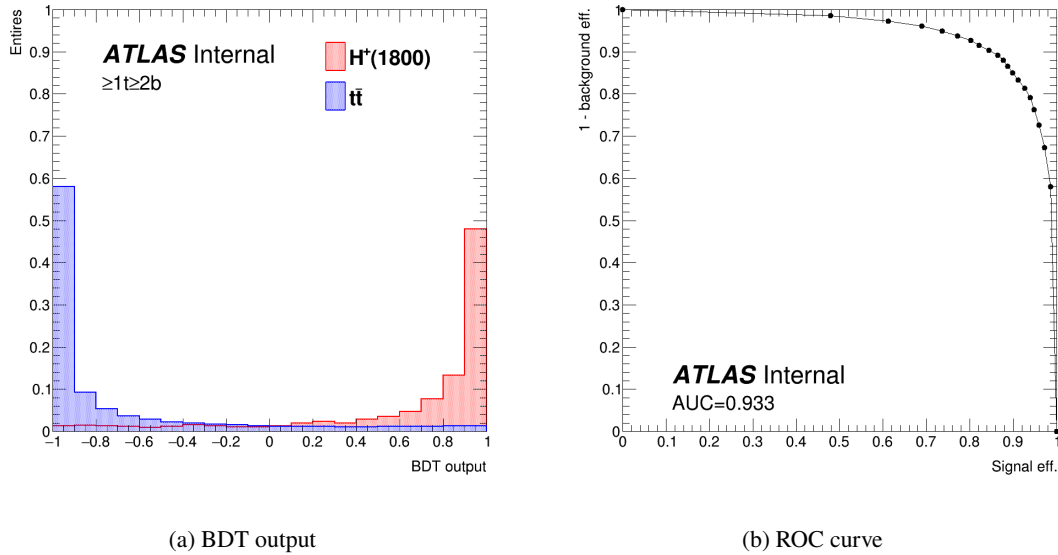


Figure 10: BDT distribution and ROC curve for the 1800 GeV H^+ mass hypothesis.

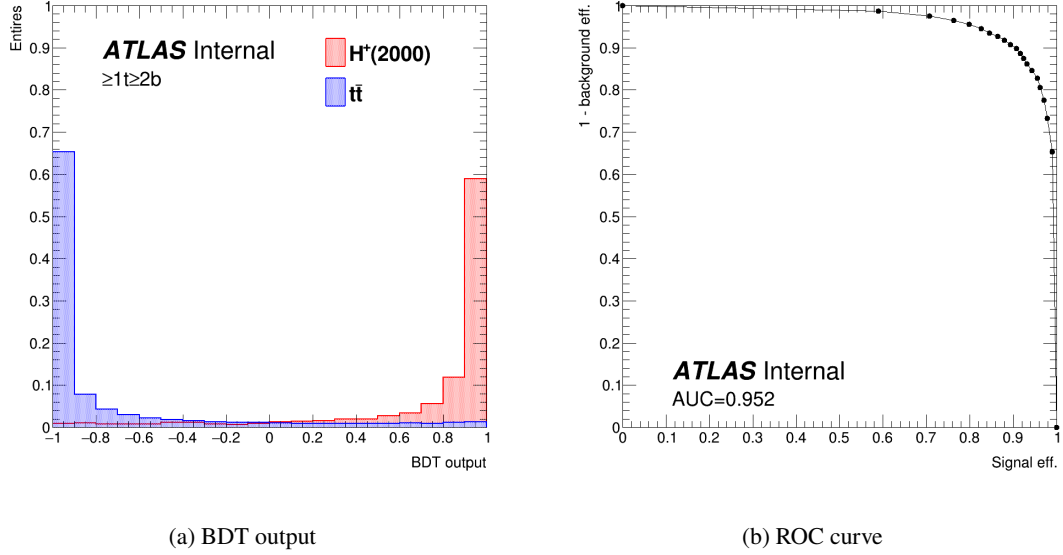


Figure 11: BDT distribution and ROC curve for the 2000 GeV H^+ mass hypothesis.

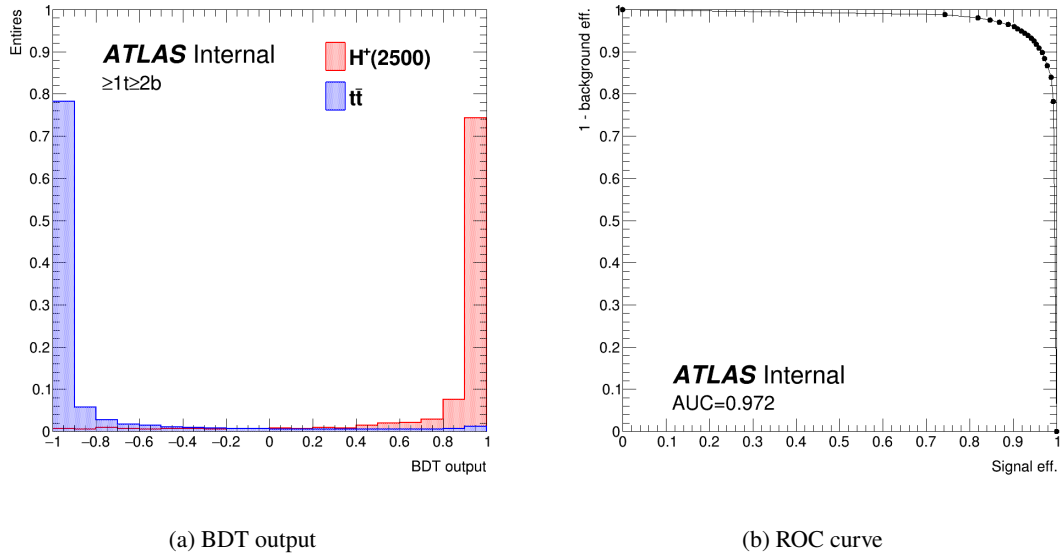


Figure 12: BDT distribution and ROC curve for the 2500 GeV H^+ mass hypothesis.

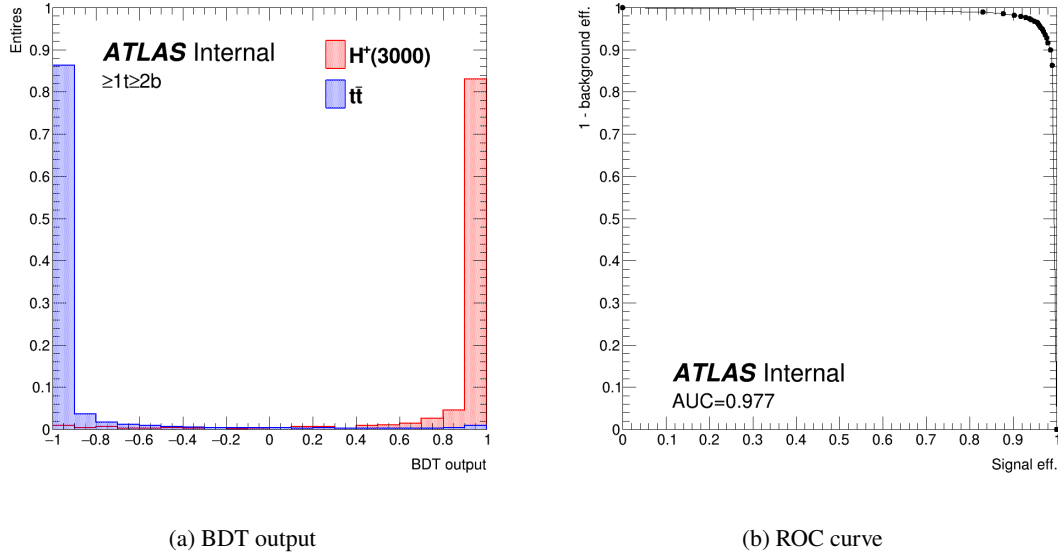


Figure 13: BDT distribution and ROC curve for the 3000 GeV H^+ mass hypothesis.

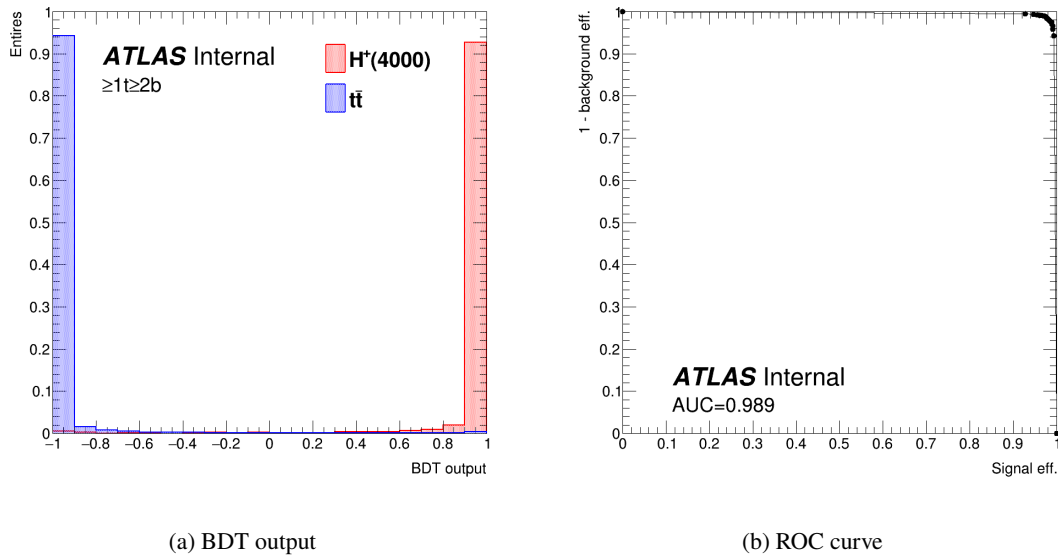
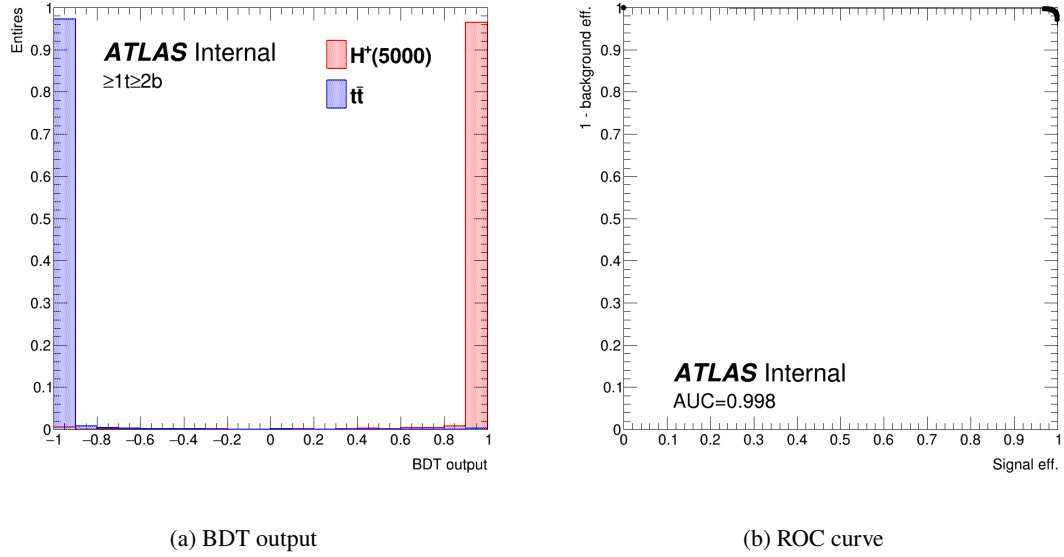


Figure 14: BDT distribution and ROC curve for the 4000 GeV H^+ mass hypothesis.



255 **3 Background modeling**

256 **3.1 Blind strategy**

257 In the following sections, modeling of kinematic distributions, in particular the ones used for BDT training,
258 of the $t\bar{t} + \text{jets}$ background is checked by comparing the data and MC. In order to avoid observing signals
259 or any other biases before fixing the analysis procedure, the following blinding strategy is applied. The
260 signal to noise ratio (S/B) is calculated in each bin of each distribution for all H^+ mass hypothesis (more
261 details in Appendix B). The signal cross section (σ_{signal}) on each H^+ mass hypothesis is set to 0.046 pb,
262 which is the upper limits at 1 TeV H^+ mass point obtained from the resolved $H^+ \rightarrow tb$ search [24], and
263 therefore it can be considered as the most conservative assumption. The data in bins with $S/B > 0.05$ in at
264 least one H^+ mass hypothesis are blinded when the data is compared with MC.

265 **3.2 Data/MC comparison for BDT input variables**

266 Figures 16 show the distributions of input variables for BDT training. Data are blinded according to
267 the blind strategy in Section 3.1. No significant difference between the data and MC is found in each
268 variable.

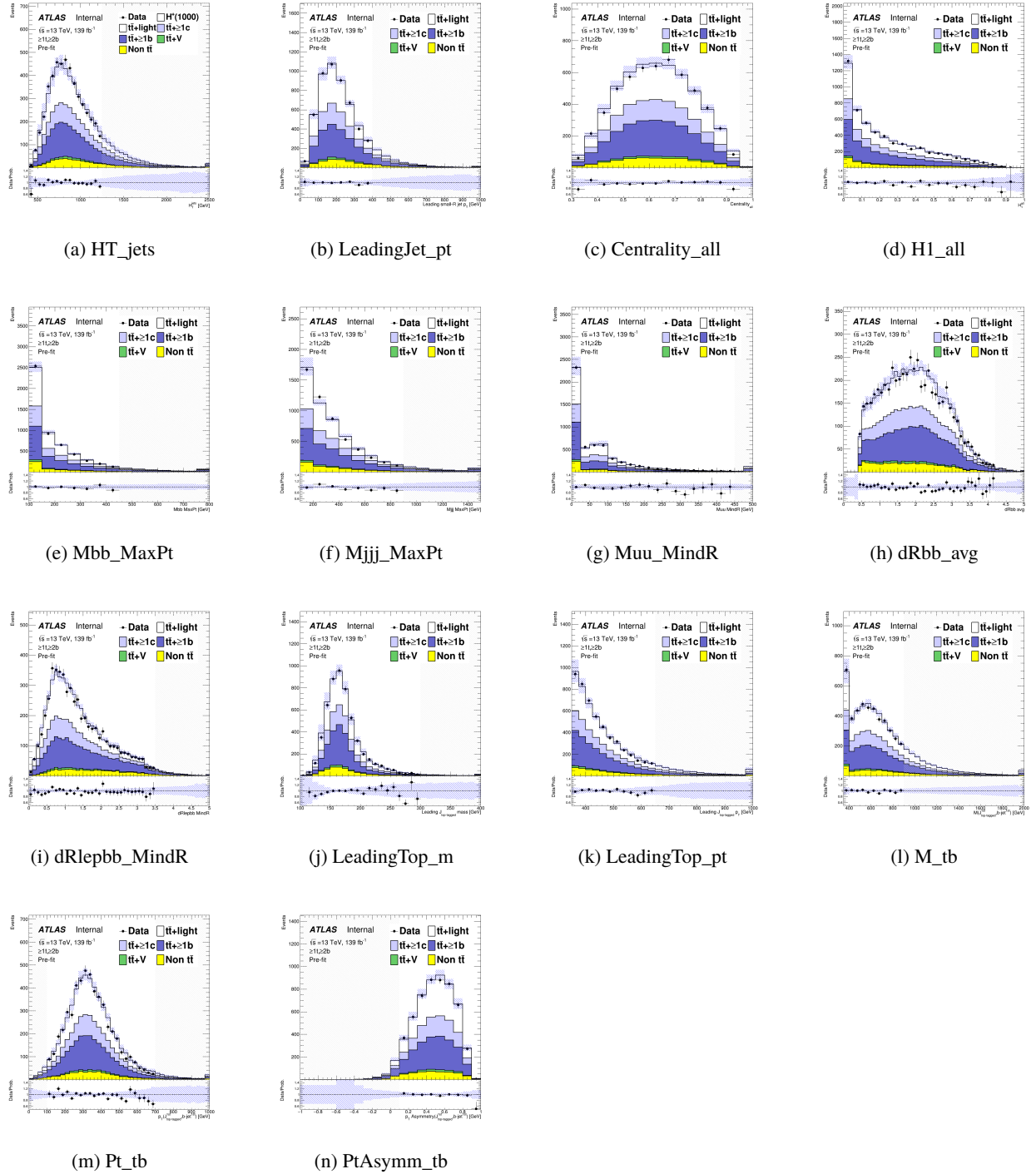


Figure 16: Comparison of the kinematic variables included in the BDT in the SR for the data and MC.

269 3.3 Data/MC comparison for BDT distributions

270 Figures 17 to 24 show the distributions of BDT output in SR and H_T^{jets} in CR. The binning of the BDT
 271 output is optimized for the search sensitivity by *TransfoD* algorithm [25]. Such binning results in extremely
 272 narrow bins towards high BDT scored, and makes the plot hard to see as shown in Figure 63 in Appendix
 273 **B.2**, when plotted in a usual manner. We rather show the distribution with equal interval for each bin. The
 274 distributions are input into the profile likelihood fit on each H^+ mass hypothesis as shown in Section 5. It
 275 is observed that the data/MC ratio tends to be lower for the high BDT score regions, which may bias search
 276 for the signal in the highest BDT bins. The reweighting to correct for the slope is discussed in Section 3.4.
 277 In H_T^{jets} distributions, there is no significant difference in the shape, while the normalization is significantly
 278 different. The $t\bar{t}$ + light yields are therefore determined by floating them in the fit.

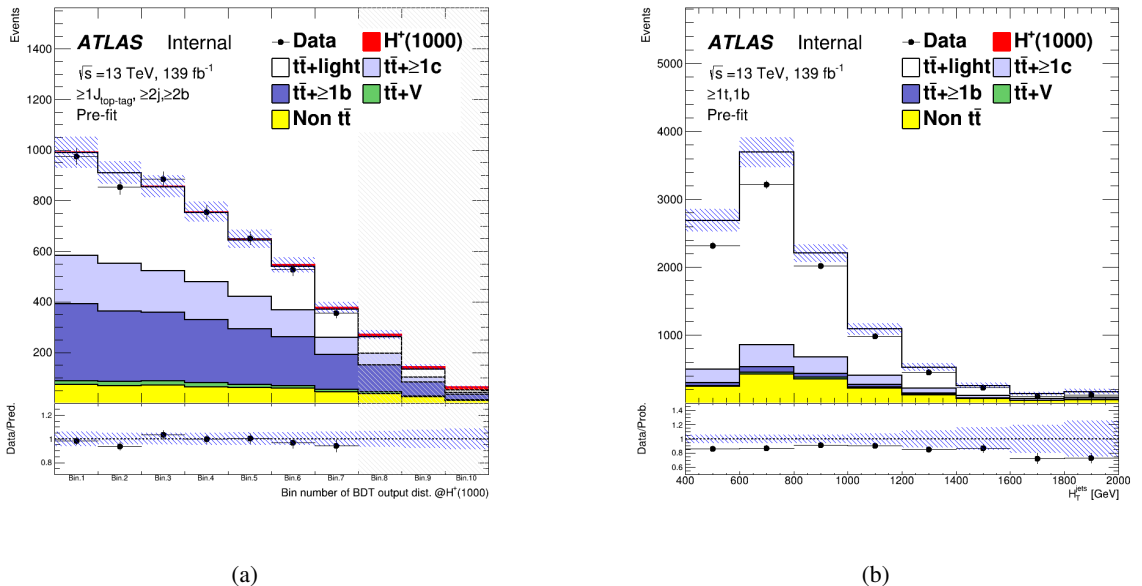


Figure 17: Pre-fit distribution of BDT output in the SR (a) and H_T^{jets} in the CR for the 1000 GeV H^+ mass hypotheses.

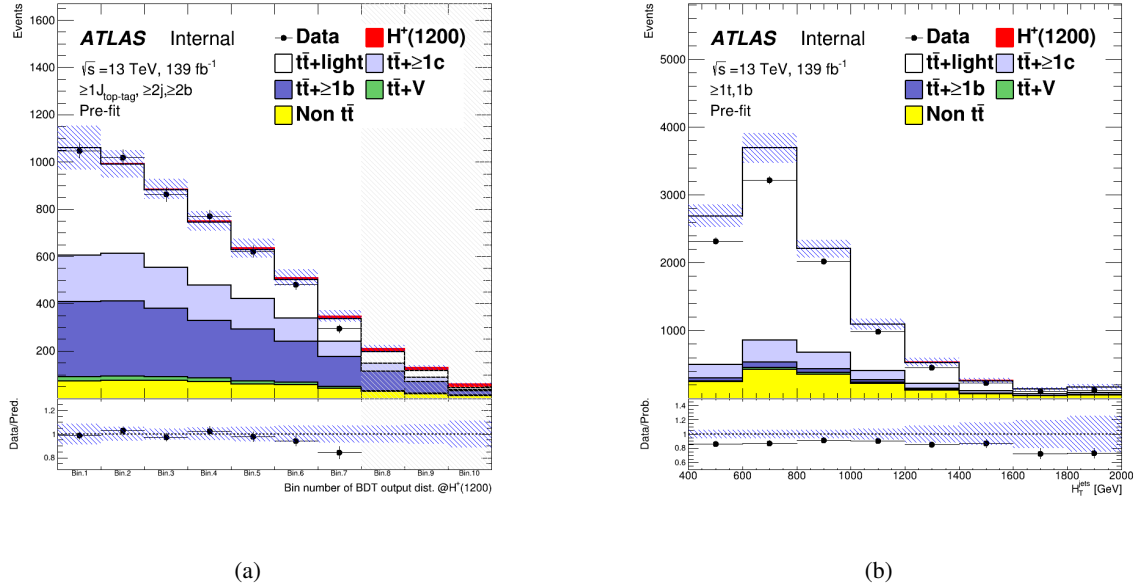


Figure 18: Pre-fit distribution of BDT output in the SR (a) and H_T^{jets} in the CR for the 1200 GeV H^+ mass hypotheses.

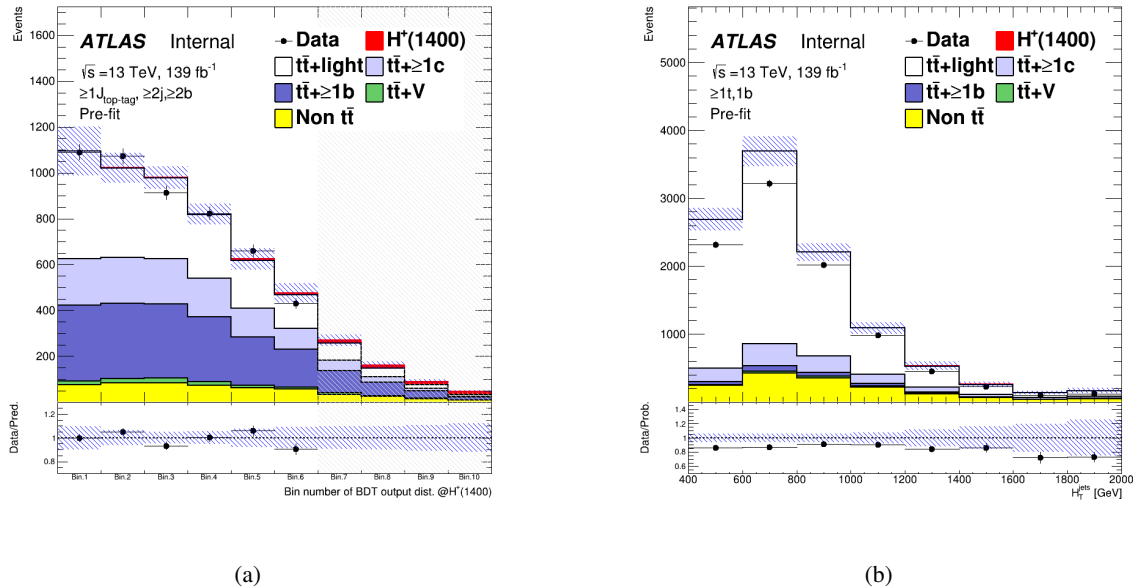


Figure 19: Pre-fit distribution of BDT output in the SR (a) and H_T^{jets} in the CR for the 1400 GeV H^+ mass hypotheses.

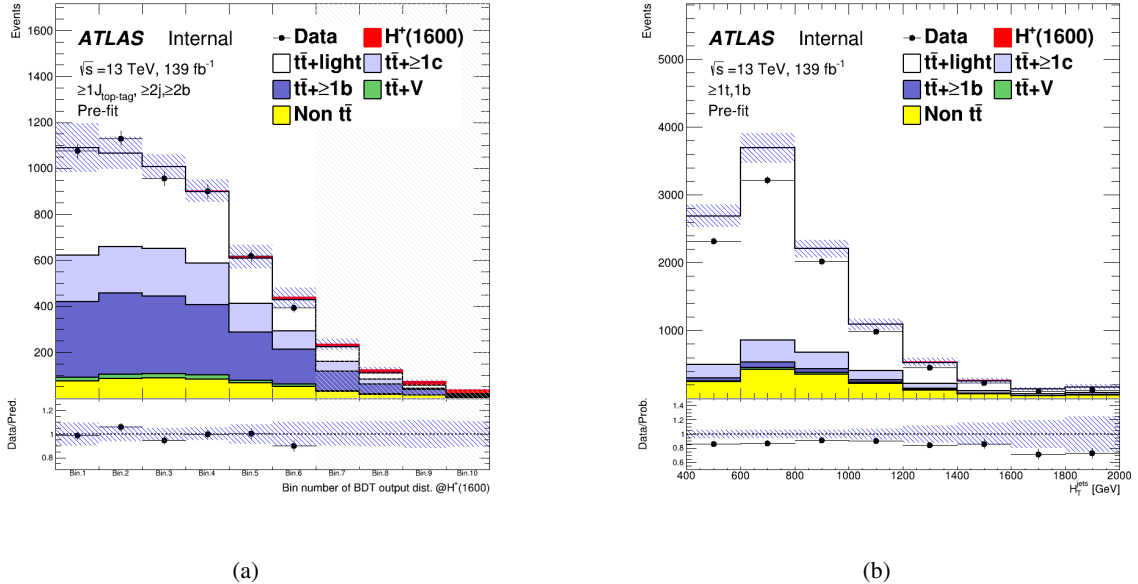


Figure 20: Pre-fit distribution of BDT output in the SR (a) and H_T^{jets} in the CR for the 1600 GeV H^+ mass hypotheses.

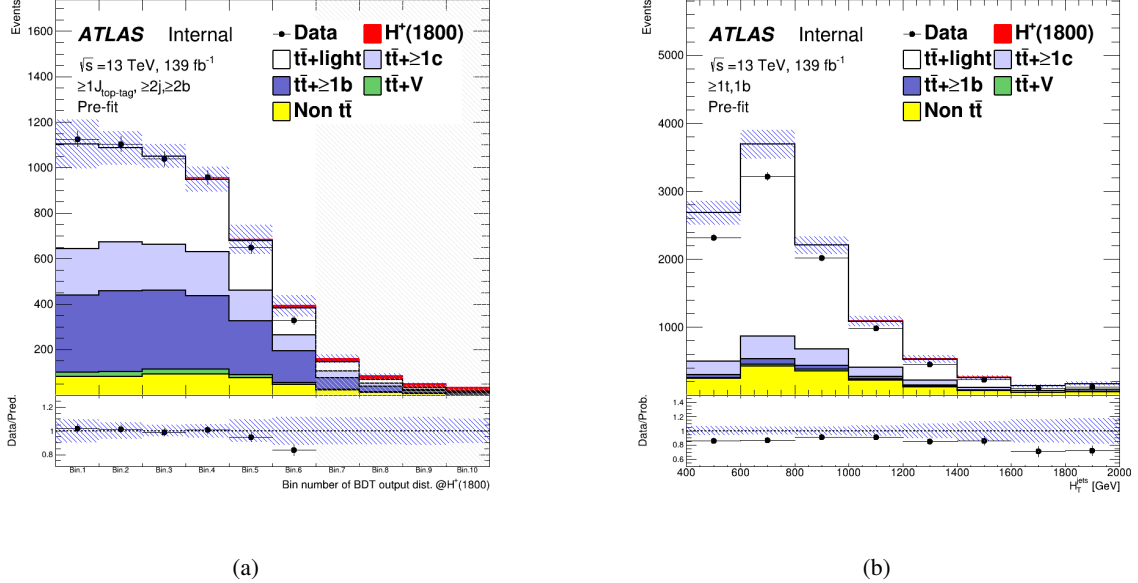


Figure 21: Pre-fit distribution of BDT output in the SR (a) and H_T^{jets} in the CR for the 1800 GeV H^+ mass hypotheses.

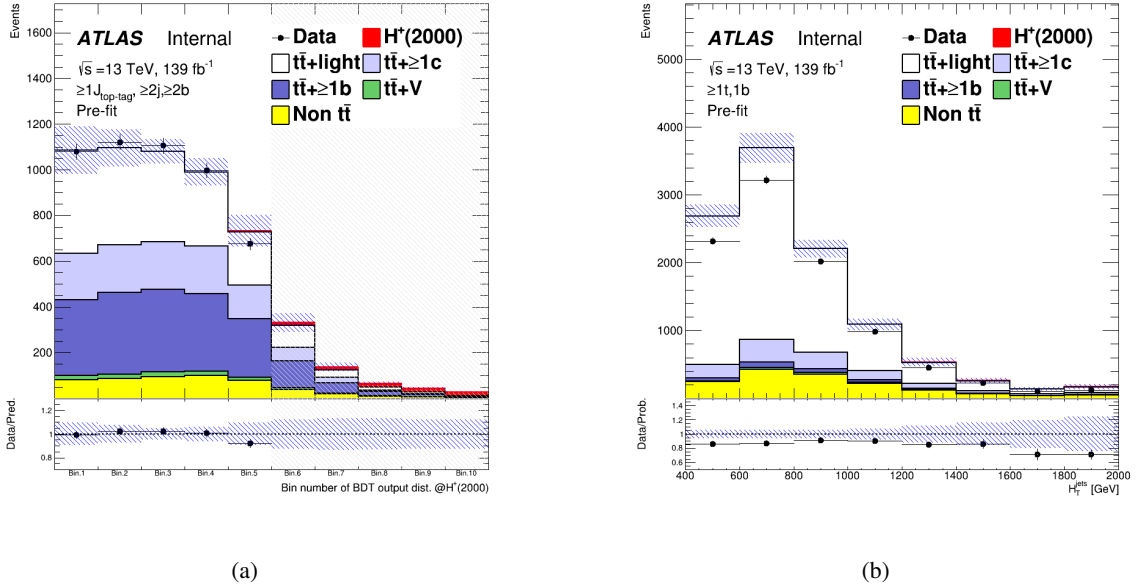


Figure 22: Pre-fit distribution of BDT output in the SR (a) and H_T^{jets} in the CR for the 2000 GeV H^+ mass hypotheses.

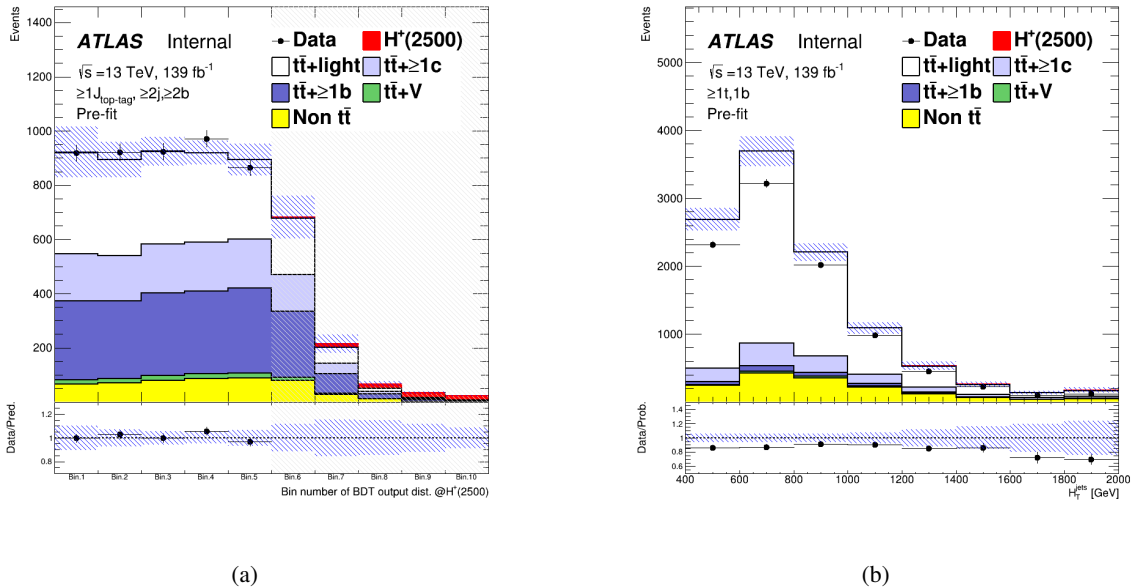


Figure 23: Pre-fit distribution of BDT output in the SR (a) and H_T^{jets} in the CR for the 2500 GeV H^+ mass hypotheses.

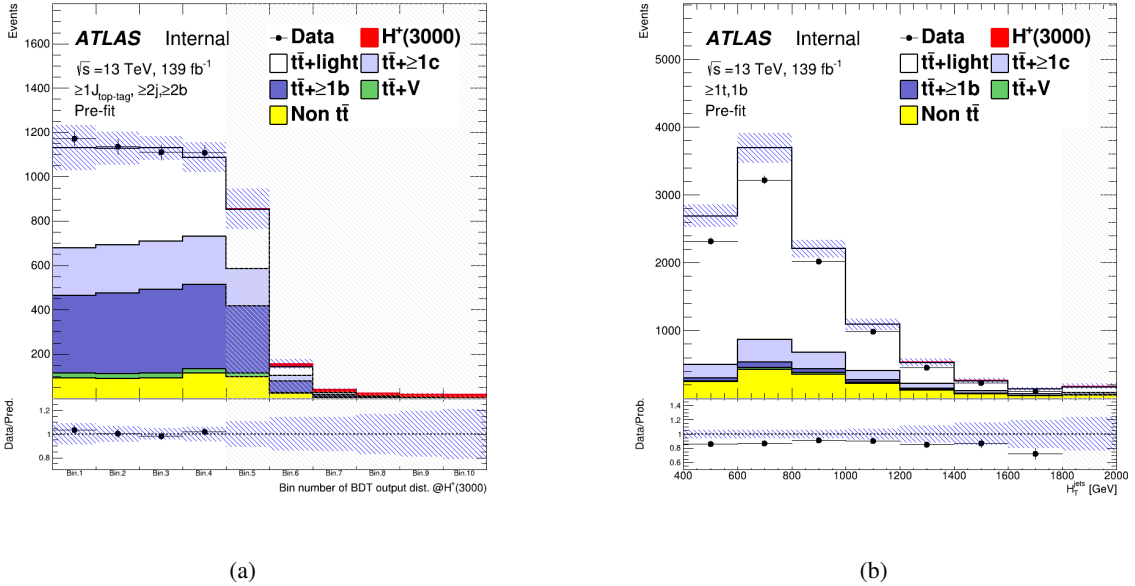


Figure 24: Pre-fit distribution of BDT output in the SR (a) and H_T^{jets} in the CR for the 3000 GeV H^+ mass hypotheses.

279 3.4 Reweighting technique

280 It is known that the $t\bar{t}$ Powheg+Pythia generator does not properly model data. Actually, BDT output
 281 distributions in the high score region are different between data and MC as shown in Figure 17 to 24. To
 282 improve the data/MC agreement, data-based corrections are applied to the MC prediction. Reweighting
 283 factors are derived by comparing the data and MC prediction in the SR. For deriving reweighting factors,
 284 events in the only low BDT score region are selected to avoid being reweighted signal events. These events
 285 are required to pass all BDT cuts under different mass hypotheses as shown in Table 9. The reweighting
 286 factors can be expressed as:

$$R(x) = \frac{\text{Data}(x) - \text{MC}^{\text{non-}t\bar{t}+\text{jets}}(x)}{\text{MC}^{t\bar{t}+\text{jets}}(x)} \quad (1)$$

287 where x is the variable mismodelled by the MC simulation. $t\bar{t} + \text{jets}$ includes the $t\bar{t} + \text{light}$, $t\bar{t}+ \geq 1c$ and
 288 $t\bar{t}+ \geq 1b$. Weights are calculated from the H_T^{jets} distribution in the SR region. Figure 25(a) shows the
 289 distribution of H_T^{jets} with BDT score cuts applied as shown in Table 9. Figure 25(b) shows the distribution
 290 of the weights derived from the H_T^{jets} distribution and a quadratic function form ($\omega = a + bx + cx^2$) obtained
 291 by fitting to the weight distribution. The function values are applied to $t\bar{t} + \text{light}$, $t\bar{t}+ \geq 1c$ and $t\bar{t}+ \geq 1b$.
 292 Table 10 includes the fitted values for all the parameters. The statistical errors of fitted parameters are
 293 included as systematic uncertainties in the profile likelihood. The weight values in $H_T^{\text{jets}} > 2057$ GeV
 294 region are extrapolated the value at $H_T^{\text{jets}} = 2057$ GeV, because the weight value of -1σ is negative at the
 295 point.

Mass point [GeV]	BDT score cut
1000	< 0.5
1200	< 0.5
1400	< 0.5
1600	< 0.5
1800	< 0.5
2000	< 0.5
2500	< 0.5
3000	< -0.2
4000	< -0.2
5000	< -0.2

Table 9: Events used for deriving weight factors are selected by cutting with BDT score under different mass hypotheses according to criterias in this tables. After the selection, S/B value at each bin is <0.05 for each BDT output distribution as shown in Figure 64

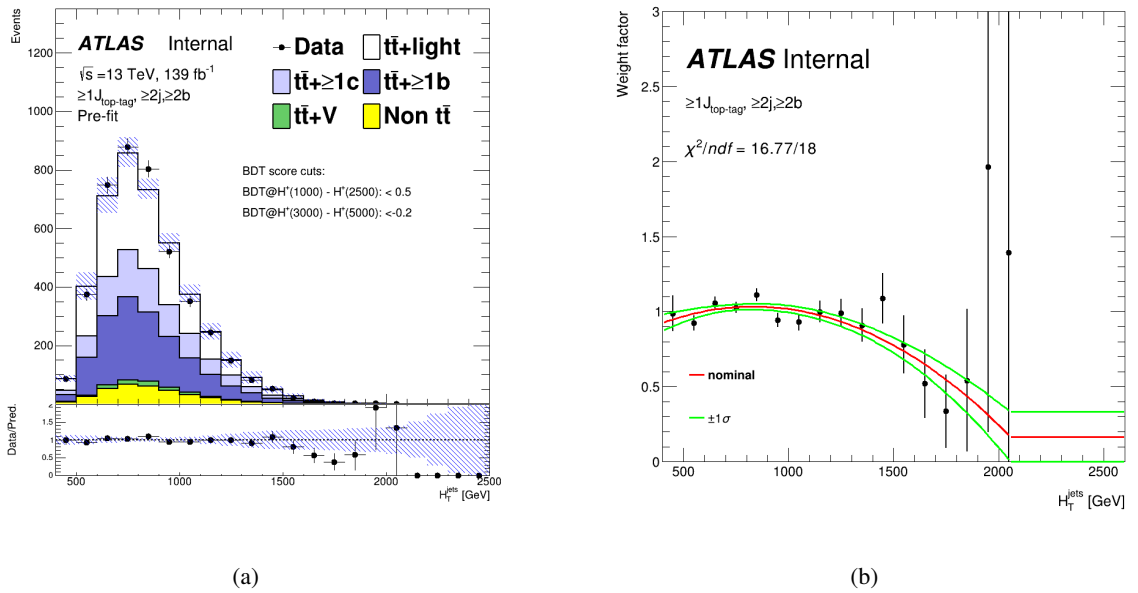


Figure 25: The H_T^{jets} distribution with BDT score cuts applied (left) and the weight distribution derived from the H_T^{jets} distribution (right) are shown. The red plot in the weight distribution is the quadratic function obtained by fitting to the weight distribution ($\omega = a + bx + cx^2$). The green ones are $\pm 1\sigma$ of the red function from the statistical errors of fitted parameters. These statistical errors are included as systematic uncertainties in the profile likelihood fit.

Parameter	Value
a	$(6.33 \pm 1.50) \times 10^{-1}$
b	$(9.63 \pm 3.04) \times 10^{-4}$
c	$(-5.78 \pm 1.46) \times 10^{-7}$

Table 10: Summary of parameters obtained by fitting to the weight distribution with a quadratic function ($\omega = a + bx + cx^2$). Error of each parameter is from statistical uncertainty.

Figure 26 to Figure 33 show the effect of the reweighting in BDT output distributions in the SR region. The data/MC improved after the reweighting for each H^+ mass hypothesis.

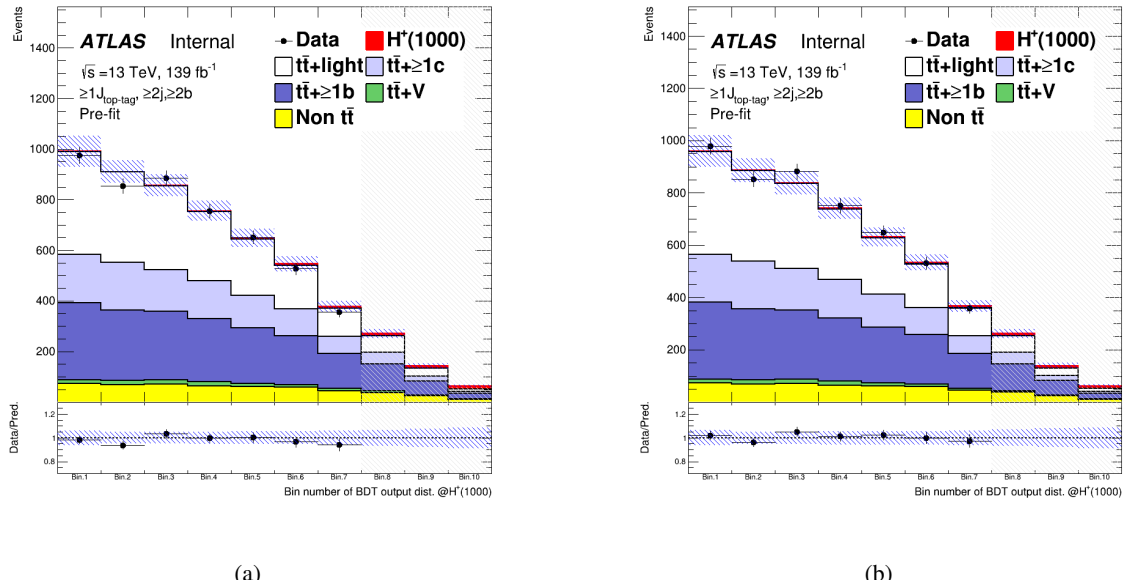


Figure 26: BDT output distribution for the 1000 GeV H^+ mass hypothesis before (left) and after (right) the reweighting.

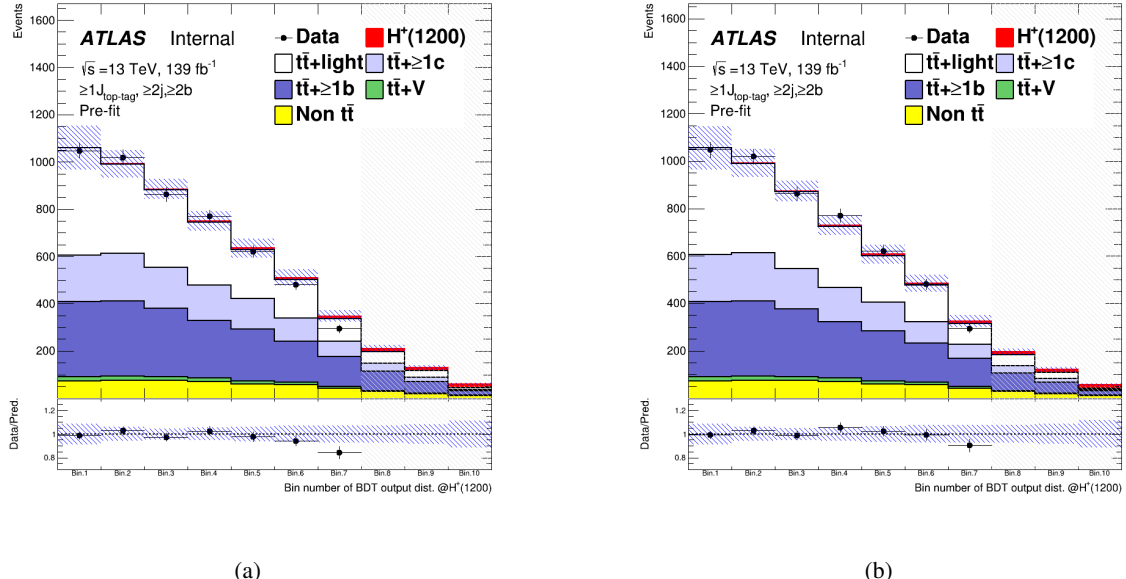


Figure 27: BDT output distribution for the 1200 GeV H^+ mass hypothesis before (left) and after (right) the reweighting.

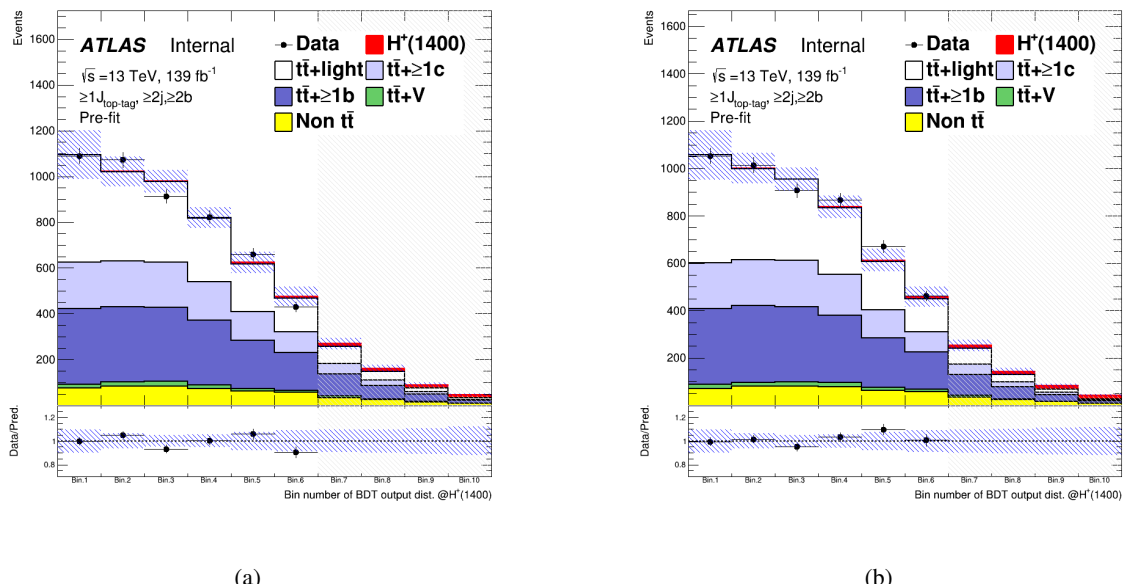


Figure 28: BDT output distribution for the 1400 GeV H^+ mass hypothesis before (left) and after (right) the reweighting.

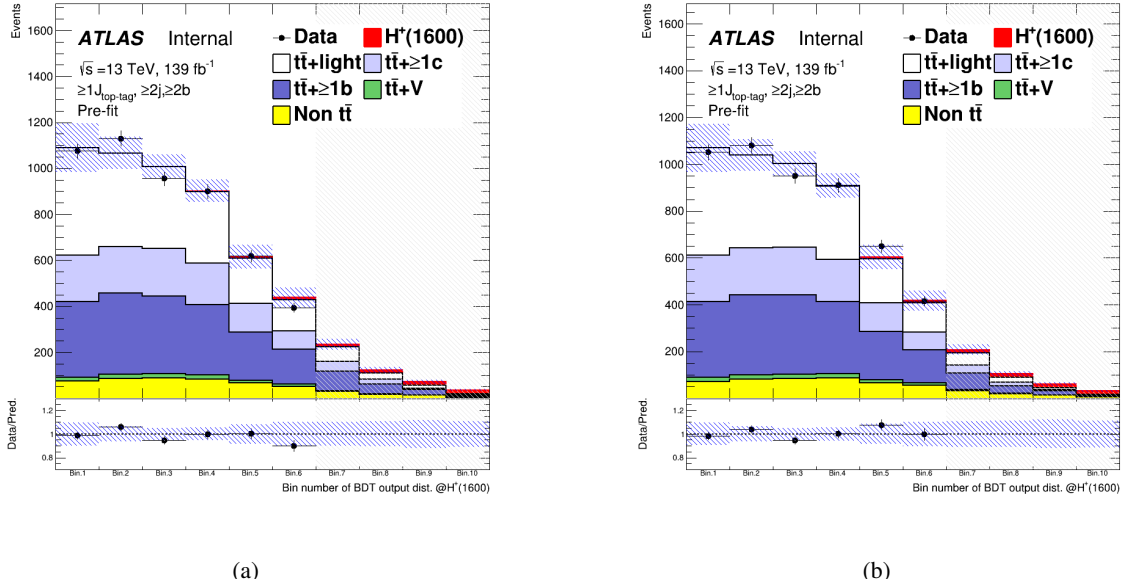


Figure 29: BDT output distribution for the 1600 GeV H^+ mass hypothesis before (left) and after (right) the reweighting.

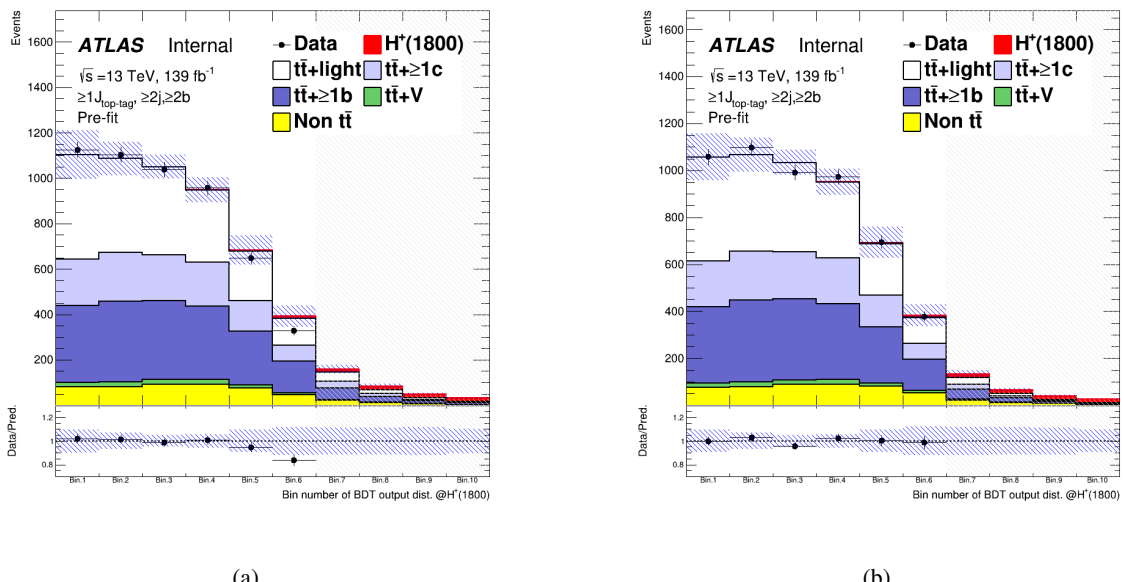


Figure 30: BDT output distribution for the 1800 GeV H^+ mass hypothesis before (left) and after (right) the reweighting.

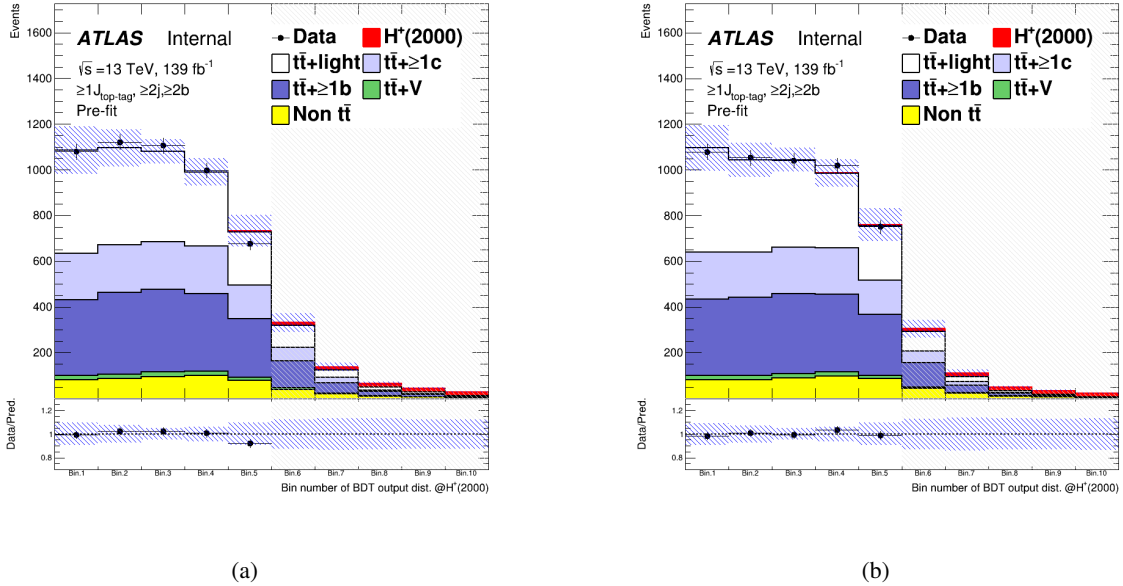


Figure 31: BDT output distribution for the 2000 GeV H^+ mass hypothesis before (left) and after (right) the reweighting.

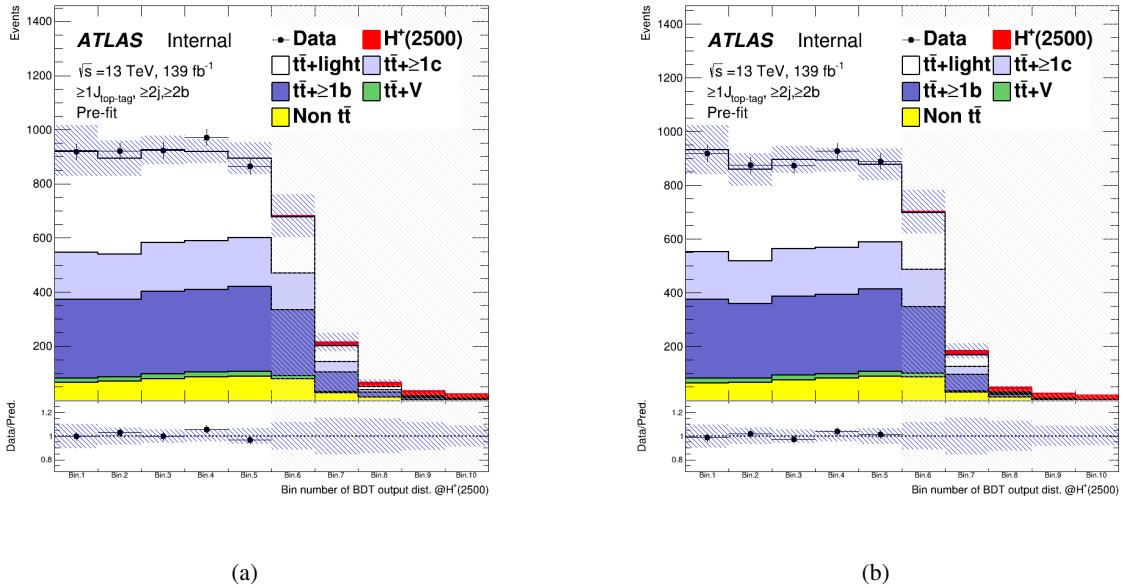


Figure 32: BDT output distribution for the 2500 GeV H^+ mass hypothesis before (left) and after (right) the reweighting.

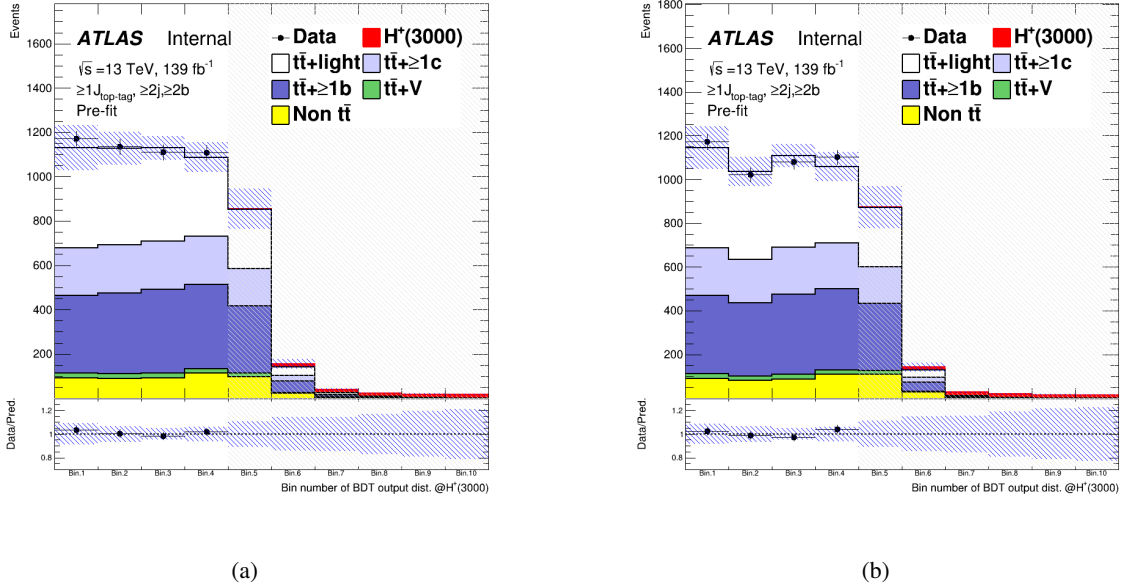


Figure 33: BDT output distribution for the 3000 GeV H^+ mass hypothesis before (left) and after (right) the reweighting.

298 4 Systematics Uncertainties

299 The uncertainties considered in the following may affect the overall normalization of the process, the shapes
 300 of the BDT and H_T^{jets} , or both. All the experimental uncertainties considered, with the exception of that in
 301 the luminosity, affect both normalization and shape in all the simulated samples. Uncertainties related
 302 to the modeling of the signal and background affect both normalization and shape, with the exception of
 303 cross-section and $t\bar{t}$ modeling uncertainties. The former only affect the normalization of the considered
 304 sample, while the latter only affect the shape of $t\bar{t}$ samples. Nevertheless, the noramlisation uncertainties
 305 modify the relative fractions of the different samples, leading to a shape uncertainty in the final BDT and
 306 H_T^{jets} distributions.

307 A single independet nuisance parameter is assigned to each source of systematic uncertainty in the statistical
 308 analysis. Some of the systematic uncertainties, in particular most of the experimental ones, are decomposed
 309 into several independent sources, as specified in the following. Each individual source then has a correlated
 310 effect across all analysis regions and signal and background samples. Table 11 presents a list of all
 311 systematic uncertainties considered and indicates for each category the number of independent components
 312 and whether they affect normalisaion of shape.

313 4.1 Luminosity and pile-up modeling

314 4.1.1 Luminosity

315 The uncertainty on the integrated luminosity for the full Run-2 data-set is 1.7% [26], obtained using
 316 LUCID-2 detector [27] for the primary luminosity measurement.

317 4.1.2 Pile-up modeling

318 A variation in the pile-up reweighting of the simulated events is included to cover the uncertainties in the
 319 ratio of the predicted and measured inelastic cross-sections in the fiducial volume defined by $M_X > 13$
 320 GeV, where M_X is the mass of the hadronic system [28].

321 cdi

322 4.2 Reconstructed objects

323 4.2.1 Charged leptons

324 Uncertainties associated with charged leptons arise from the trigger selection, the object reconstruction,
 325 identification and isolation criteria, as well as the lepton momentum scale and resolution. The reconstruction,
 326 identification and isolation efficiency of electrons and muons, as well as efficiency of the trigger used
 327 to record the events, differ slightly between data and simulation, which is compensated for by dedicated
 328 scale factors (SFs). Efficiency SFs are measured using tag-and-probe techniques on $Z \rightarrow l^+l^-$ data and
 329 simulated samples [4, 29], and are applied to the simulation to correct for the differences. The effect of
 330 these SFs as well as of their uncertainties are propagated as corrections to the MC event weight. In total,
 331 four independent components are considered for electrons and ten for muons.

Systematics uncertainty	Type	Components
Experimental uncertainties		
Luminosity	N	1
Pileup modeling	SN	1
<i>Physics objects</i>		
Electrons	SN	7
Muons	SN	15
Small-R jet energy scale	SN	31
Small-R jet energy resolution	SN	9
Small-R jet mass scale	SN	8
Large-R jet energy scale	SN	24
Large-R jet energy resolution	SN	12
Large-R jet mass scale	SN	18
Large-R jet mass resolution	SN	10
Jet vertex tagger	SN	1
<i>b</i> -tagging		
Efficiency	SN	45
Mis-tag rate (c)	SN	20
Mis-tag rate (light)	SN	20
<i>top</i> -tagging		
Signal efficiency	SN	9
p_T extrapolation signal efficiency	SN	1
background efficiency	SN	5
inefficiency	SN	3
Signal and background modeling		
<i>Signal</i>		
PDF variations	SN	30
Scales	SN	2
<i>t</i> $\bar{t} background$		
PDF variations	SN	90
<i>t</i> $\bar{t} + HF normalization$	N (free floating)	1
<i>t</i> $\bar{t} + light normalization$	N (free floating)	1
<i>t</i> $\bar{t} + light modeling$	S	6
<i>t</i> $\bar{t} + \geq 1c modeling$	S	6
<i>t</i> $\bar{t} + \geq 1b modeling$	S	7
<i>t</i> $\bar{t} + jets reweighting$	SN	1
<i>Other backgrounds</i>		
<i>t</i> $\bar{t}W cross-section$	N	2
<i>t</i> $\bar{t}Z cross-section$	N	2
<i>t</i> $\bar{t}W modeling$	SN	1
<i>t</i> $\bar{t}Z modeling$	SN	1
Single top cross-section	N	3
Single top modeling	SN	6
W+jets normalization	N	3
Z+jets normalization	N	1
Diboson normalization	N	1
<i>t</i> $\bar{t}t\bar{t} cross-section$	N	3

Table 11: List of systematic uncertainties included in the analysis.

332 Additional sources of uncertainty originate from the corrections applied to adjust the lepton momentum
 333 scale and resolution in the simulation to match those in data, measured using reconstructed distributions of
 334 the $Z \rightarrow l^+l^-$ and $J/\psi \rightarrow l^+l^-$ masses, as well as the E/p ratio measured in $W \rightarrow e\nu$ events, where E and p
 335 are the electron energy and momentum measured by the calorimeter and the tracker, respectively [4, 30].
 336 To evaluate the effect of momentum scale uncertainties, the event selection is redone with the lepton energy
 337 or momentum varied by $\pm 1\sigma$. For the momentum resolution uncertainties, the event selection is redone
 338 by smearing the lepton energy or momentum. In total, three independent components are considered for
 339 electrons and five for muons.

340 **4.2.2 Small- R jets, Large- R jets**

341 Uncertainties associated with jets arise from the efficiency of pile-up rejection by the JVT, from the jet
 342 energy scale (JES) and resolution (JER), from the jet mass scale (JMS) and resolution (JMR), and from b -
 343 and top-tagging.

344 **Jet vertex tagging:**

345 Scale factors are applied to correct for discrepancies between data and MC for JVT efficiencies.
 346 These SFs are estimated using $Z \rightarrow \mu^+\mu^-$ with tag-and-probe techniques similar to those in Ref.[9],
 347 and the effect of these SFs as well as of their uncertainties are propagated as corrections to the MC
 348 event weight.

349 **Small- R jet:**

350 The *R4_CategoryReduction_FullJER.config* jet uncertainties configuration is used. The JES and
 351 its uncertainty for small- R jets are derived by combining information from test-beam data, LHC
 352 collision data and simulation [31]. The uncertainties from these measurements are factorized into
 353 several independent sources. Additional uncertainties are considered, related to jet flavor (using the
 354 conservative default value of $50 \pm 50\%$ for the quark/gluon fraction for all MC samples), pile-up
 355 corrections, η dependence, high- p_T jets, and differences between full and fast simulation, yielding a
 356 total of 31 independence sources.

357 The JER was measured in Run-2 data and simulation as a function of jet p_T and rapidity using dijet
 358 events, using a similar method as that in Ref. [32]. The combined uncertainty is propagated by
 359 smearing the jet p_T in MC, yielding to nine independent sources.

360 The JMS uncertainties for small- R jets are derived using the RTrk uncertainties that compares the
 361 ratio of the jet mass for calorimeter jets to the jet mass of track-based jets in data and MC simulation
 362 [33]. The six NPs are provided related with baseline, modeling, tracking and total statistics. The
 363 technique takes advantage of two independent measures of the jets mass (in the calorimeter and
 364 using the ID), however this assumption breaks in the case of particle flow jets which uses both
 365 calorimeter and tracking information. For PFlow jets, the uncertainties derived for EMTopo jets are
 366 used and two additional uncertainties are provided. These uncertainties are derived by comparing
 367 the jet mass of EMTopo and PFlow jets in data and MC. Two NPs are provided similarly to the RTrk
 368 uncertainties related with baseline and modeling. The JMS uncertainties are intentionally derived
 369 after the application of the JES and JER smearing. This is different compared to large- R jets where
 370 no nominal JER smearing is applied. The JES corrects the overall energy scale, which impacts the
 371 mass as it is applied to the full four-vector. The JMS correction and uncertainties are then a residual

372 correction accounting for the distribution of energy within the jet. For this reason, the JES and JMS
 373 uncertainties are to first order uncorrelated effects.

374 **Large- R jet:**

375 The *R10_CategoryJES_FullJER_FullJMS.config* jet uncertainties configuration is used for JES,
 376 JER and JMS variation. JES uncertainties for large- R jets are derived using a similar approach as
 377 for small- R jets [33]. Correlation between these two objects are taken into account in uncertainty
 378 evaluation. Additional uncertainties related with a topology of an event are included.

379 The JER uncertainties for large- R jets are derived in the same way as the small- R jets uncertainties.
 380 The dijet balance asymmetry is used to evaluate the JER, which is sufficient to cover the fully
 381 supported kinematic regime for large- R jet usage. The nominal data/MC difference is found to
 382 be consistent with 1 within uncertainty. For this reason, no nominal JER smearing is applied.
 383 Instead, the nominal data/MC difference from 1 is taken as an additional uncertainty on top of the
 384 uncertainties related with limited statistics, detector effects, or modeling. The FullJER model with
 385 12 NPs is used. Both data and MC events are smeared to cover properly the correlations between jets
 386 different regions of the detector.

387 The JMS uncertainties for large- R jets are derived from the forward folding technique (FF) in the
 388 limited region of $200 \text{ GeV} < p_T < 1000 \text{ GeV}$ around the W and top mass peaks [33, 34]. The
 389 Rtrk technique is used to extend this region to $200 \text{ GeV} < p_T < 3000 \text{ GeV}$, $m < 600 \text{ GeV}$ and
 390 $|\eta| < 2.0$. The forward folding method is used to fit the W and top mass peaks in $t\bar{t}$ semileptonic
 391 events. The Rtrk method uses the double ratio of data/MC for calorimeter only quantities and
 392 track-only quantities. This technique can cover wider range in p_T , η and mass. However, forward
 393 folding technique is more precise in the lower p_T region and the mass around the top and W masses.
 394 The uncertainties from the two approaches are combined and fitted as a function p_T in a given mass
 395 bin. Interpolation between mass bins is used to provide smooth uncertainties. The full set of JMS
 396 NPs is used in the analysis in order to allow possible combinations with other measurements. The
 397 NPs are related with limited statistics of measurements, detector effects, modeling and selections. In
 398 addition, uncertainties related with interpolation between mass bins and uncertainties related with a
 399 difference between QCD and hadronic decay jet mass response are included.

400 Measurements of the JMR in the $t\bar{t}$ semileptonic events are also used to constrain the JMR uncertainties
 401 by using the forward folding method [33, 34]. Measurements are performed in two mass regions
 402 to cover W boson and top quark mass peaks. The W boson mass peak is fitted in a region of
 403 $50 \text{ GeV} < m_{\text{jet}} < 120 \text{ GeV}$ and $200 \text{ GeV} < p_{T,\text{jet}} < 350 \text{ GeV}$. The top mass peak is fitted in a region
 404 of $120 \text{ GeV} < m_{\text{jet}} < 300 \text{ GeV}$ and $350 \text{ GeV} < p_{T,\text{jet}} < 1000 \text{ GeV}$. Relative JMR uncertainty of 20%
 405 is used outside these regions. FullJMR uncertainty model with 10 nuisance parameters is used to
 406 cover uncertainties related with measurement of JMR using FF method, interpolation between bins
 407 and comparison between different MC models for events outside the two gions. This measurement is
 408 within top mass interval. However, $p_{T,\text{jet}}$ exceeds the p_T range provided by the FF method.

409 **b -tagging:**

410 b -tagging efficiencies in simulated samples are corrected to match efficiencies in data. Scale factors
 411 are derived as a function of p_T for jets containing b -jets, c -jets and for jets containing neither b -
 412 nor c -hadrons (light-jets) separately, in dedicated calibration analysis. For b -jets efficiencies, $t\bar{t}$
 413 events in the dilepton topology are used, exploiting the very pure sample of b -jets arising from the
 414 decays of the top quarks [10]. For c -jet mistag rates, $t\bar{t}$ events in signle-lepton topology are used,
 415 exploiting the c -jets from the hadronically decaying W bosons, using techniques similar as those in

Ref. [35]. For light-jets mistag rates, the so-called negative-tag method similar as that in Ref. [36] is used, but using $Z + \text{jets}$ events instead of di-jet events. In the three calibration analyses, a large number of uncertainty components are considered, and a principal component analysis is performed, yielding in 45, 20 and 20 eigenvariations, respectively, for b -, c and light-jets, which are taken as uncorrelated sources of uncertainties. The number of these eigenvariations correspond to the number of p_T bins, (9, 4 and 4, respectively, for b -, c - and light-jets) multiplied by the number of the tag weight bins ($\varepsilon \in [0\%, 60\%], [60\%, 70\%], [70\%, 77\%], [77\%, 85\%], [85\%, 100\%]$). The calibration used in this analysis is stored in following "CDI file":

`/cvmfs/atlas.cern.ch/repo/sw/database/GroupData/xAODTaggingEfficiency/13TeV/2020-21-13TeV-MC16-CDI-2021-04-16_v1.root.`

Top-tagging:

Uncertainties related with the top-tagging calibration are provided for the signal and the background jets [16, 37]. Jets are called signal if they passed contained top criteria. Otherwise, they are called background jet. Uncertainties for back ground jets are measured in two phase-spaces containing QCD multijet and gamma+jet processes. The signal jets uncertainties are measured in the boosted $t\bar{t}$ lepton+jets channel in the range of leading large-R jet $p_T \leq 1$ TeV, because there are too few $t\bar{t}$ events to extract scale factors for $p_T \geq 1$ TeV. Therefore, additional uncertainties are assigned to cover signal modeling effects and extrapolation beyond the phase-spaces. These uncertainties were released as part of the consolidated large- R jet uncertainties.

4.3 Signal modeling

4.3.1 H^+ signal

The H^+ signal uncertainty is modeled in two way: by using the PDF uncertainties and through the variation of μ_f and μ_r . The uncertainties from the modeling of the PDF, which is done with the NNPDF2.3 (3.0) PDF set for datasets simulated at ≤ 3.0 (≥ 4.0) TeV, is made using a symmetrized Hessian set, PDF4LHC15_nlo_30, following the PDF4LHC recommendations for LHC Run II [38]. The signal scale uncertainty is modeled by varying μ_f and μ_r up (and down) by a factor 2 (or 0.5).

4.4 Background modeling

4.4.1 $t\bar{t}+\text{jets}$

$t\bar{t} + \text{heavy flavor classification}$

The $t\bar{t} + \text{jets}$ background is categorized according to the flavor of additional jets in the event, using the same procedure as described in Ref. [39]. Generator-level particle jets are reconstructed from stable particles (mean lifetime $\tau > 3 \times 10^{-11}$ seconds) using the anti- k_t algorithm with a radius parameter $R = 0.4$, and are required to have $p_T > 15$ GeV and $|\eta| < 2.5$. The flavor of a jet is determined by counting the number of b - or c -hadrons within $\Delta R < 0.4$ of the jet axis. Jets matched to exactly one b -hadron, with p_T above 5 GeV, are labeled single- b -jets, while those matched to two or more b -hadrons are labeled b -jets (with no p_T requirement on the second hadron); single- c - and c -jets are defined analogously, only considering jets not already defined as single- b - or b -jets. Events that have at least one single- b - or b -jet, not counting heavy-flavor jets from top-quark or W -boson decays, are

454 labeled as $t\bar{t} + \geq 1b$; those with no single- b - or b -jet but at least one single- c - or c -jet are labeled
 455 as $t\bar{t} + \geq 1c$. Finally, events not containing any heavy-flavor jets aside from those from top-quark
 456 or W -boson decays are labeled as $t\bar{t}$ + light. This classification is used to define the background
 457 categories in the likelihood fit.

458 Systematic uncertainties

459 The systematic uncertainties affecting the $t\bar{t}$ + jets background modeling are summarized in Table 12.

460 The normalization of $t\bar{t}$ + light, $t\bar{t} + \geq 1c$ and $t\bar{t} + \geq 1b$ are allowed to vary freely in the fit. The
 461 normalization factors of $t\bar{t} + \geq 1c$ and $t\bar{t} + \geq 1b$ are estimated with a common parameter in the
 462 fit. However, since these distribution's shapes are different slightly each other in the signal region
 463 as shown in Figure 34, the uncertainty of the composition ratio of these events gives a bias to the
 464 estimation of the signal strength. Therefore, the difference between the nominal BDT output (H_T^{jets})
 465 distribution in the SR (CR) and the one fluctuated the ratio with the total events of $t\bar{t} + \geq 1c$ and
 466 $t\bar{t} + \geq 1b$ fixed is included as one nuisance parameter (ttb: $\pm 20\%$, ttc: $\pm 34\%$ ($\mp 5\%$) in the SR (CR)).
 467 Besides normalization, the $t\bar{t}$ + light, $t\bar{t} + \geq 1c$ and $t\bar{t} + \geq 1b$ processes are affected by different types
 468 of uncertainties: $t\bar{t}$ + light has additional diagrams and profits from relatively precise measurements
 469 in data; $t\bar{t} + \geq 1c$ and $t\bar{t} + \geq 1b$ can have similar or different diagrams depending on the flavor
 470 scheme used for the PDF, and different mass of the c - and b -quark contribute to additional differences
 471 between these two processes. For these reasons, all uncertainties in the $t\bar{t}$ + jets background modeling
 472 are assigned independent nuisance parameters for the $t\bar{t}$ + light, $t\bar{t} + \geq 1c$ and $t\bar{t} + \geq 1b$ processes.

473 The weights derived in Section 3.4 are varied within their statistical uncertainties. The difference
 474 between the BDT output distribution reweighted with the nominal weight factor and the one weighted
 475 with $\pm 1\sigma$ weight factor is included in the fit for each $t\bar{t}$ + jets. Threfore, 3 NPs are included as the
 476 reweighting systematics in total.

477 Systematic uncertainties on the acceptance and shapes are extracted from the comparison between
 478 the nominal and different MC samples and settings. For ISR and FSR the settings of the nominal
 479 Powheg+Pythia sample are varied, resulting in different event weight; the uncertainty due to ISR is
 480 estimated by changing μ_r and μ_f in the ME and α_S^{ISR} in the PS, while the uncertainty due to FSR is
 481 estimated by changing α_S^{FSR} in the PS. For the ISR, the amount of radiation is increased (descreased)
 482 by scaling μ_r and μ_f by a factor 0.5 (2.0) and by using the Var3cUp (Var3cDown) variation from the
 483 A14 tune [40], corresponding to $\alpha_S^{\text{ISR}} = 0.140(0.115)$ instead of the nominal $\alpha_S^{\text{ISR}} = 0.127$. For the
 484 FSR, the amount of radiation is increased (decreased) varying μ_r for QCD emission in the FSR by a
 485 factor of 0.5 (2.0), corresponding to $\alpha_S^{\text{FSR}} = 0.1423(0.1147)$ instead of the nominal $\alpha_S^{\text{FSR}} = 0.127$. The
 486 nominal Powheg+Pythia sample is compared to the Powheg+Herwig sample to access the effect
 487 of the PS and hadronisation models, and to the MG5_aMC sample to access the effect of the NLO
 488 matching technique.

489 The nominal prediction for the dominant $t\bar{t} + \geq 1b$ background, based on the Powheg+Phytia $t\bar{t}$ (5FS)
 490 sample in which all the additional partons are produced by the PS, is compared to the alternative
 491 Powheg+Phythia $t\bar{t}$ (4FS) sample, in which the $b\bar{b}$ pair is generated in addition to the $t\bar{t}$ pair at the
 492 ME level at NLO in QCD. A uncertainty resulting from the comparison of the shape of the two
 493 models is included.

Uncertainty source	Description	Components
$t\bar{t} + \text{jets}$ reweighting	Statistical uncertainties of weights	All $t\bar{t} + \text{jets}$
$t\bar{t} + \text{light}$ normalization	Free-floating	$t\bar{t} + \text{light}$
$t\bar{t} + \text{HF}$ normalization	Free-floating	$t\bar{t} + \geq 1c$ and $t\bar{t} + \geq 1b$
$t\bar{t} + \geq 1b$ flavor scheme	5FS vs 4FS	$t\bar{t} + \geq 1b$
NLO matching	MG5_aMC+Pythia	vs. Powheg+Pythia
PS & hadronisation	Powheg+Herwig	vs. Powheg+Pythia
α_S^{ISR}	$Var3cUp$ ($Var3cDown$)	in Powheg+Pythia
μ_f	scaling by 0.5 (2.0)	in Powheg+Pythia
μ_r	scaling by 0.5 (2.0)	in Powheg+Pythia
FSR	Varying α_S^{FSR} (PS)	in Powheg+Pythia

Table 12: Summary of the sources of systematic uncertainty for $t\bar{t} + \text{jets}$ modeling. The systematic uncertainties listed in the second section of the table are evaluated in such a way to have no impact on the normalization of the three, $t\bar{t} + \text{light}$, $t\bar{t} + \geq 1c$ and $t\bar{t} + \geq 1b$ components in the phase-space selected in the analysis. The last column of the table indicates the $t\bar{t} + \text{jets}$ components to which a systematic uncertainty is assigned. All systematic uncertainty sources are treated as uncorrelated across the three components.

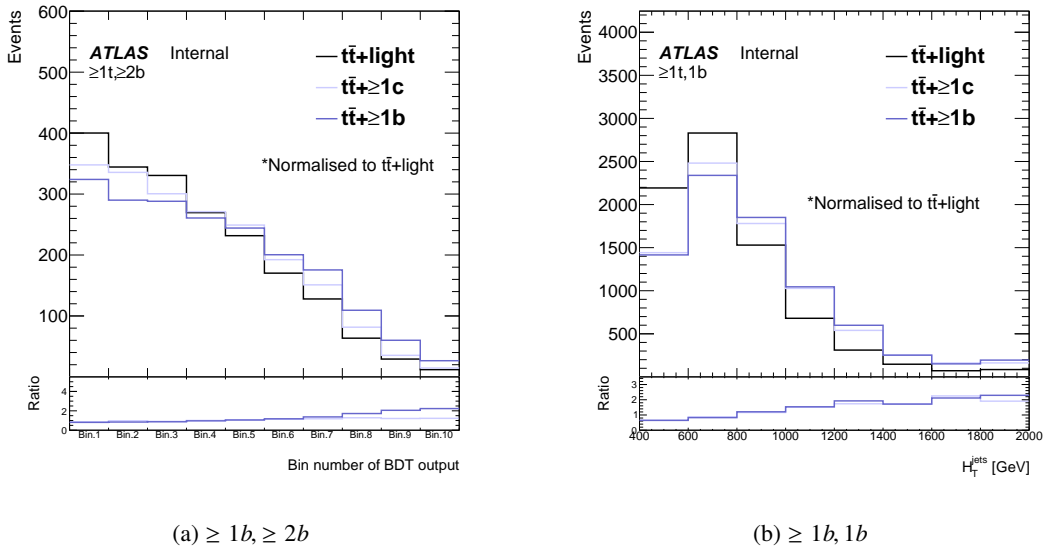


Figure 34: BDT output distribution in SR for the 1000 GeV H^+ mass hypothesis (left) and H_T^{jets} distribution in CR (right). Distributions of $t\bar{t} + \geq 1b$ and $t\bar{t} + \geq 1b$ are normalised to $t\bar{t} + \text{light}$. And the ratio to $t\bar{t} + \text{light}$ are computed for $t\bar{t} + \geq 1b$ and $t\bar{t} + \geq 1b$.

4.4.2 Other backgrounds

The predicted $t\bar{t}H$ signal cross-section uncertainty is $+5.8\%$ (QCD scale) $\pm 3.6\%$ (PDF + α_S) [41–46]. These two components are treated as uncorrelated in the fit. The effect of QCD scale and PDF variations on the shape of the distributions is found to be negligible. Uncertainties in the Higgs-boson branching fractions are also considered; these amount to 2.2% for the $b\bar{b}$ decay mode [41]. Uncertainties associated to the

499 modeling of $t\bar{t}H$ by the Powheg+Phythia sample are also considered, for a total of four independent
500 components. The uncertainty due to ISR is estimated by simultaneously changing μ_f and μ_r in the ME and
501 α_S^{ISR} in the PS, while the uncertainty due to ISR is estimated by changing α_S^{FSR} in the PS. For the ISR and
502 FSR, the amount of radiation is varied following the same procedure as for $t\bar{t}$. The nominal Powheg+Pythia
503 sample is compared to the Powheg+Herwig sample to access the uncertainty due to PS and hadronization,
504 and to the MG5_aMC+Phythia sample for the uncertainty due to the NLO matching.

505 A $\pm 5\%$ uncertainty is considered for the cross-sections of the three single-top production modes [47–51].
506 Uncertainties associated with the PS and hadronisation model, and with the NLO matching scheme are
507 evaluated by comparing, for each process, the nominal Powheg+Pythia sample to a sample produced using
508 Powheg+Herwig and MG5_aMC+Pythia, respectively. The uncertainty associated to the interference
509 between Wt and $t\bar{t}$ production at NLO [52] is assessed by comparing the nominal Powheg+Pythia sample
510 produced using the "diagram removal" scheme to an alternative sample produced with the same generator
511 but using the "diagram subtraction" scheme.

512 The uncertainty of the $t\bar{t}V$ NLO cross-section prediction is 15% [53, 54], split into PDF and scale
513 uncertainties as for $t\bar{t}H$. An additional $t\bar{t}V$ modeling uncertainty, related to the choice of PS and
514 hadronisation model and NLO matching scheme is assessed by comparing the nominal MG5_aMC+Pythia
515 samples with alternative ones generated with Sherpa.

516 A total 50% normalization uncertainty is considered for the 4 tops background, covering effects from
517 varying μ_f and μ_r , PDFs and α_S [55, 56]. The small backgrounds from tZq and tWH are each assigned
518 cross-section uncertainties: $\pm 7.9\%$ and $\pm 0.9\%$ for tZq , accounting for μ_f and μ_r variations, and for PDFs,
519 respectively, and $\pm 50\%$ for tWZ [55].

520 An uncertainty of 40% is assumed for the $W +$ jets cross-section, with an additional 30% normalization
521 uncertainty used for $W +$ heavy-flavor jets, taken as uncorrelated between events with two and more than
522 two heavy-flavor jets. These uncertainties are based on variations of the μ_f and μ_r and of the matching
523 parameters in the Sherpa samples. An uncertainty of 35% is then applied to the $Z +$ jets normalization,
524 uncorrelated across jet bins, to account for both the variations of the scales and matching parameters in the
525 Sherpa samples and the uncertainty in the extraction from data of the correction factor for the heavy-flavor
526 component. Finally, a total 50% normalization uncertainty in the diboson background is assumed, which
527 includes uncertainties in the inclusive cross-section and additional jet production [57].

5 Profile Likelihood Fit (Without reweighting)

5.1 Method

In order to test for the presence of an $H^+ \rightarrow tb$ ($W' \rightarrow tb$) signal, a binned maximum-likelihood fit to the data is performed simultaneously in all analysis regions, and each mass hypothesis is tested separately. The input to the fit is the BDT distribution for the SR and H_T^{jets} distribution for the CR. Two initially unconstrained fit parameters are used to model the normalization of the $t\bar{t}$ + light and $t\bar{t} + \geq 1$ HF jets background. The procedures used to quantify the level of agreement with the background-only or background-plus-signal hypothesis, and to determine exclusion limits, are based on the profile likelihood ratio test and the CL_s method. The parameter of interest is the signal strength, μ .

To estimate the signal strength, a likelihood function, $\mathcal{L}(\mu, \theta)$, is constructed as the product of Poisson probability terms. One Poisson term is included for every bin of the BDT and H_T^{jets} distribution in the analysis regions. Binning of BDT output distribution is defined by an automatic binning algorithm, *TransfoD*, implemented in TRexFitter [25]. The expected number of events in the Poisson terms is a function of μ , and a set of nuisance parameters, θ . The nuisance parameters encode effects from the normalization of backgrounds, including two free normalization factors for the $t\bar{t}$ + light and $t\bar{t} + \geq 1$ HF jets backgrounds, the systematic uncertainties and one parameter per bin to model statistical uncertainties in the simulated samples. All nuisance parameters are constrained with Gaussian or log-normal terms. There are about 400 nuisance parameters considered in the fit, the number varying slightly across the range of mass hypotheses.

To extract the exclusion limit on μ , the following test statistic is used:

$$\tilde{t}_\mu = \begin{cases} -2 \ln \frac{\mathcal{L}(\mu, \hat{\theta}(\mu))}{\mathcal{L}(0, \hat{\theta}(0))} & \mu < 0 \\ -2 \ln \frac{\mathcal{L}(\mu, \hat{\theta}(\mu))}{\mathcal{L}(\hat{\mu}, \hat{\theta})} & \mu \geq 0 \end{cases} \quad (2)$$

The values of the signal strength and nuisance parameters that maximize the likelihood function are represented by $\hat{\mu}$ and $\hat{\theta}$, respectively. For a given value of μ , the values of the nuisance parameters that maximize the likelihood function are represented by $\hat{\theta}(\mu)$.

5.2 Pruning and smoothing of systematic uncertainties

In the fits, pruning is applied at the threshold of 1%, meaning that if the effect of a nuisance parameter is smaller than 1% before fitting (separately for shape and normalisation) it is excluded from the fit. This pruning procedure reduces the CPU time and helps the fit to converge. Appendix C shows the systematic uncertainties that are pruned in Asimov fits.

Smoothing is applied for systematics uncertainties on $t\bar{t}$ modeling by *MaxVariation* algorithm implemented in TRexFitter, because these uncertainties are typically computed by comparing two different MC samples, or by applying MC generator weights on a MC sample, which dilutes the MC statistics and increases the fluctuations. No smoothing is applied for modeling systematic uncertainties on small backgrounds — given their small impact on the final result — or for experimental systematics — which are obtained either by

561 applying SFs typically close to unity (e.g. b -tagging), or by using the same simulated events but with
562 different calibrations of the objects (e.g. JES).

563 **5.3 Asimov fit results**

564 In the following, the results of fits to Asimov datasets generated from simulated samples are presented.
565 Figures 35 to 50 show the nuisance parameters, normalization factors, correlation matrices, the effect of
566 the different nuisance parameters before and after the fit and post-fit plots from the fits under each H^+ mass
567 hypotheses.

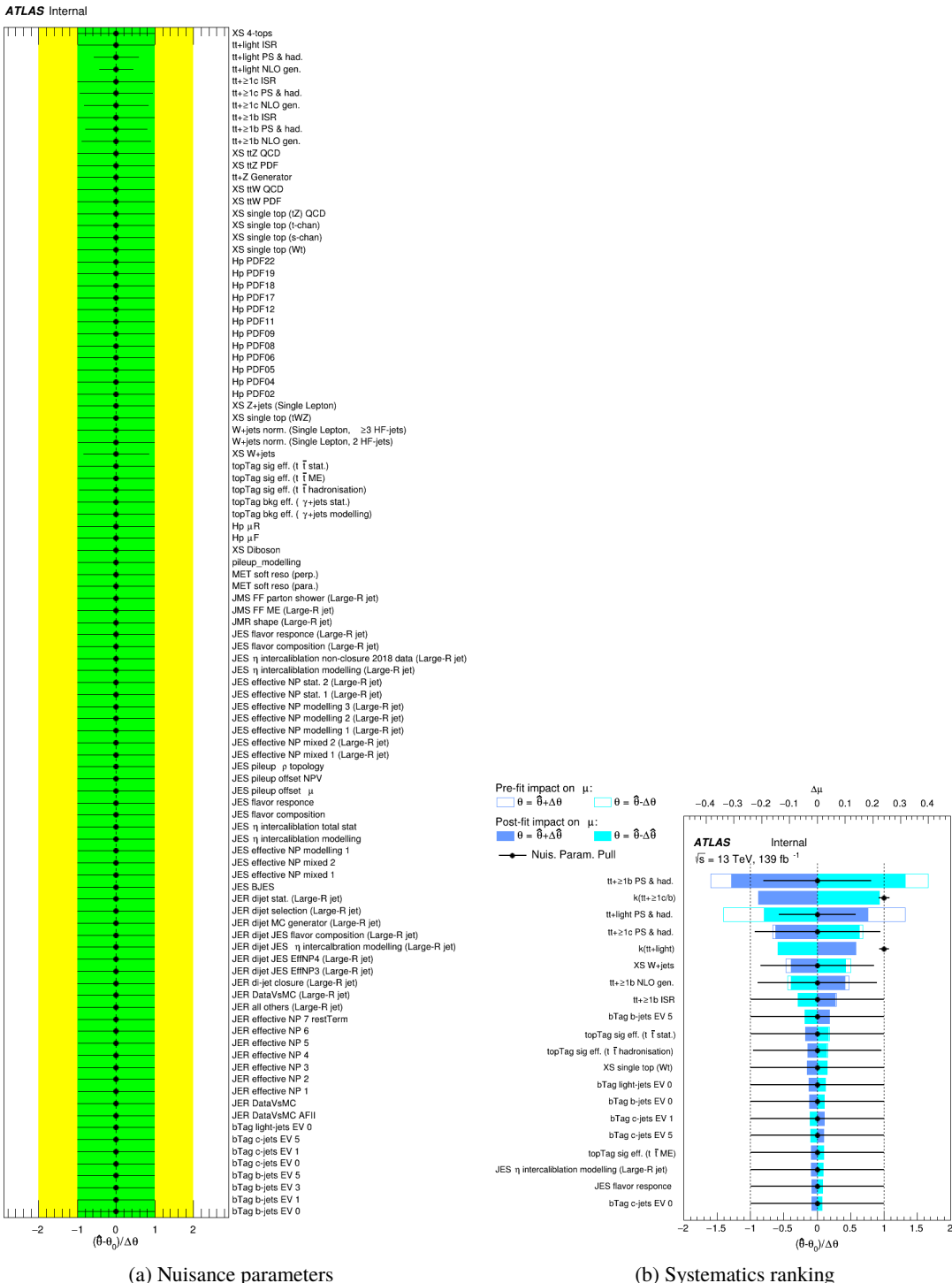


Figure 35: Nuisance parameters (left) and ranking plot (right) of the effect of various nuisance parameters before and after the fit for the 1000 GeV H^+ mass hypotheses.

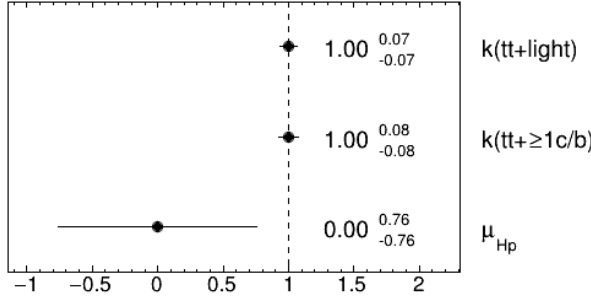
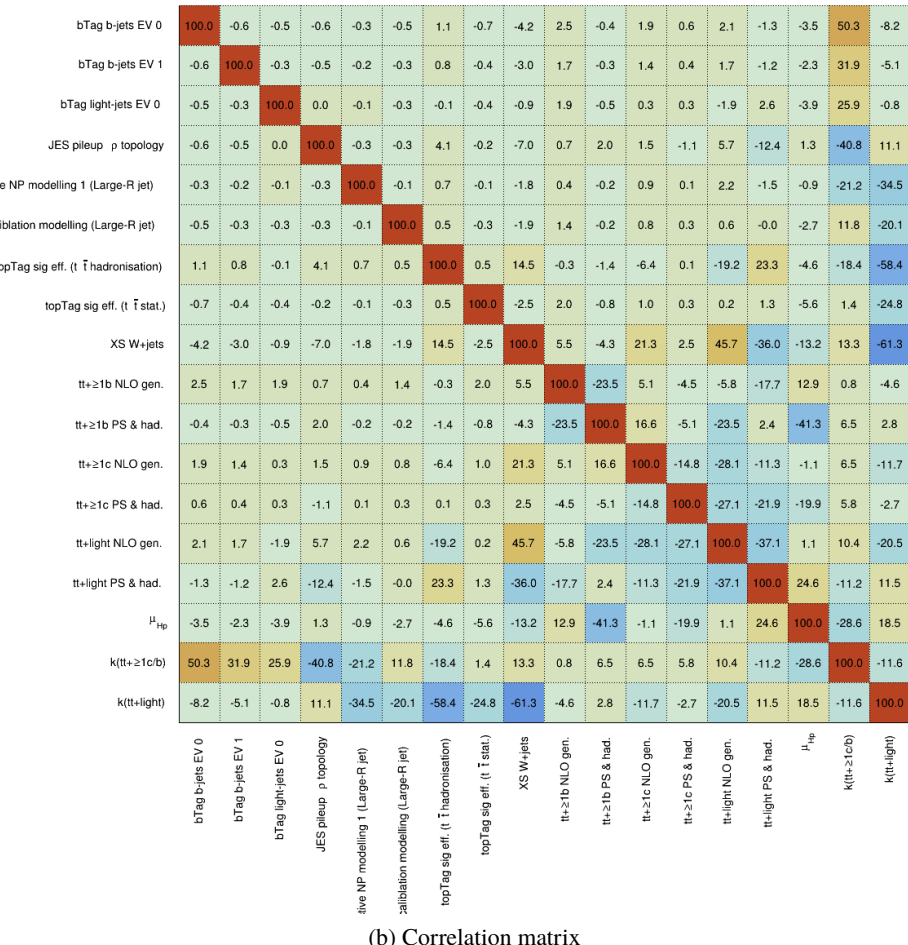
ATLAS Internal**ATLAS Internal**

Figure 36: Signal strength and normalization factors (top) and correlation matrix (bottom) for the 1000 GeV H^+ mass hypotheses.

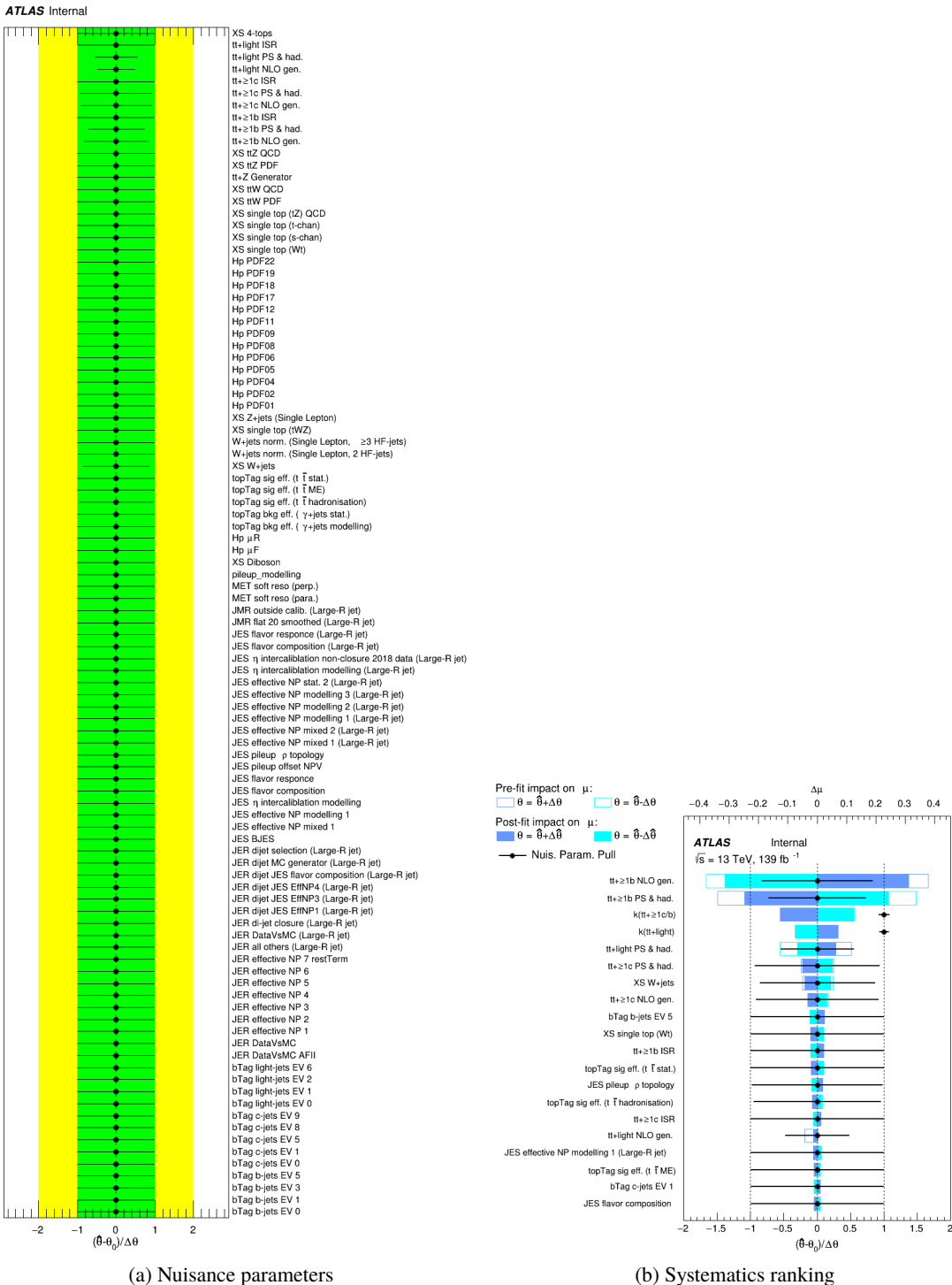
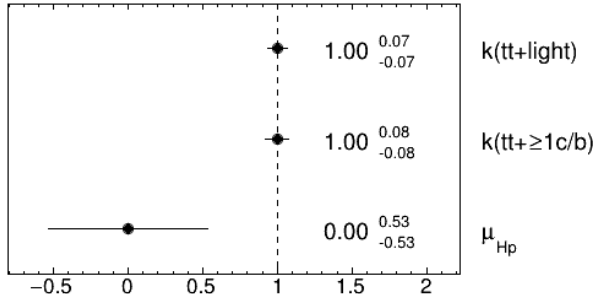


Figure 37: Nuisance parameters (left) and ranking plot (right) of the effect of various nuisance parameters before and after the fit for the 1200 GeV H^+ mass hypotheses.

ATLAS Internal

(a) Norm. factors

ATLAS Internal

	bTag b-jets EV 0	-0.4	0.0	-0.5	-0.3	-0.3	0.1	1.6	-0.4	-3.5	2.5	1.7	1.0	0.5	2.6	-2.6	-2.0	50.6	-9.0
bTag b-jets EV 1	-0.4	100.0	0.0	-0.4	-0.2	-0.2	0.0	1.1	-0.2	-2.5	1.6	1.0	0.7	0.4	2.2	-2.2	-1.1	32.1	-5.6
bTag light-jets EV 0	0.0	0.0	100.0	0.0	0.0	0.0	0.0	-0.1	0.0	0.5	0.3	1.6	0.6	0.0	-0.6	-1.2	1.6	25.7	-2.0
JES pileup p topology	-0.5	-0.4	0.0	100.0	-0.3	-0.2	-0.2	4.4	-0.1	-6.8	-0.3	0.6	1.6	-0.1	4.9	-12.3	3.3	-41.2	10.7
active NP modelling t (Large-R jet)	-0.3	-0.2	0.0	-0.3	100.0	-0.1	0.0	0.9	-0.1	-1.8	0.8	0.3	0.3	0.2	2.1	-1.2	-2.2	-21.0	-34.3
calibration modelling (Large-R jet)	-0.3	-0.2	0.0	-0.2	-0.1	100.0	0.0	0.8	-0.2	-1.5	1.4	1.0	0.4	0.2	0.9	-0.8	-1.9	11.9	-20.4
topTag bkg eff. (γ+jets modelling)	0.1	0.0	0.0	-0.2	0.0	0.0	100.0	0.2	0.1	-0.3	-0.3	-0.0	-0.4	-0.3	-1.8	-2.2	1.8	-20.1	-1.4
topTag sig eff. (t̄hadronisation)	1.6	1.1	-0.1	4.4	0.9	0.8	0.2	100.0	0.9	14.1	-8.0	-10.0	-4.9	-1.5	-15.5	16.4	-3.1	-18.5	-57.7
topTag sig eff. (t̄stat.)	-0.4	-0.2	0.0	-0.1	-0.1	-0.2	0.1	0.9	100.0	-1.7	2.0	1.3	0.3	0.2	0.9	-0.0	-4.1	1.4	-25.4
XS W+jets	-3.5	-2.5	0.5	-6.8	-1.8	-1.5	-0.3	14.1	-1.7	100.0	3.1	-2.9	7.5	2.7	51.1	-38.0	-8.5	13.9	-62.2
t̄t+≥1b NLO gen.	2.5	1.6	0.3	-0.3	0.8	1.4	-0.3	-8.0	2.0	3.1	100.0	-53.6	-8.7	-4.0	4.9	-24.3	59.0	-7.0	1.8
t̄t+≥1b PS & had.	1.7	1.0	1.6	0.6	0.3	1.0	-0.0	-10.0	1.3	-2.9	-53.6	100.0	-17.0	-0.4	2.4	-10.7	-46.3	12.6	4.0
t̄t+≥1c NLO gen.	1.0	0.7	0.6	1.6	0.3	0.4	-0.4	-4.9	0.3	7.5	-8.7	-17.0	100.0	-9.0	-41.8	-11.2	-5.9	4.1	-3.0
t̄t+≥1c PS & had.	0.5	0.4	0.0	-0.1	0.2	0.2	-0.3	-1.5	0.2	2.7	-4.0	-0.4	-9.0	100.0	-27.0	-28.9	-9.8	3.2	-1.6
t̄t+light NLO gen.	2.6	2.2	-0.6	4.9	2.1	0.9	-1.8	-15.5	0.9	51.1	4.9	2.4	-41.8	-27.0	100.0	-29.0	-1.7	12.7	-26.8
t̄t+light PS & had.	-2.6	-2.2	-1.2	-12.3	-1.2	-0.8	-2.2	16.4	-0.0	-38.0	-24.3	-10.7	-11.2	-28.9	-29.0	100.0	12.5	-10.5	17.1
μ_{H_p}	-2.0	-1.1	1.6	3.3	-2.2	-1.9	1.8	-3.1	-4.1	-8.5	59.0	-46.3	-5.9	-9.8	-1.7	12.5	100.0	-23.8	14.0
$k(t\bar{t}+\geq 1c/b)$	50.6	32.1	25.7	-41.2	-21.0	11.9	-20.1	-18.5	1.4	13.9	-7.0	12.6	4.1	3.2	12.7	-10.5	-23.8	100.0	-12.0
$k(t\bar{t}+\text{light})$	-9.0	-5.6	-2.0	10.7	-34.3	-20.4	-1.4	-57.7	-25.4	-62.2	1.8	4.0	-3.0	-1.6	-26.8	17.1	14.0	-12.0	100.0

(b) Correlation matrix

Figure 38: Signal strength and normalization factors (top) and correlation matrix (bottom) for the 1200 GeV H^+ mass hypotheses.

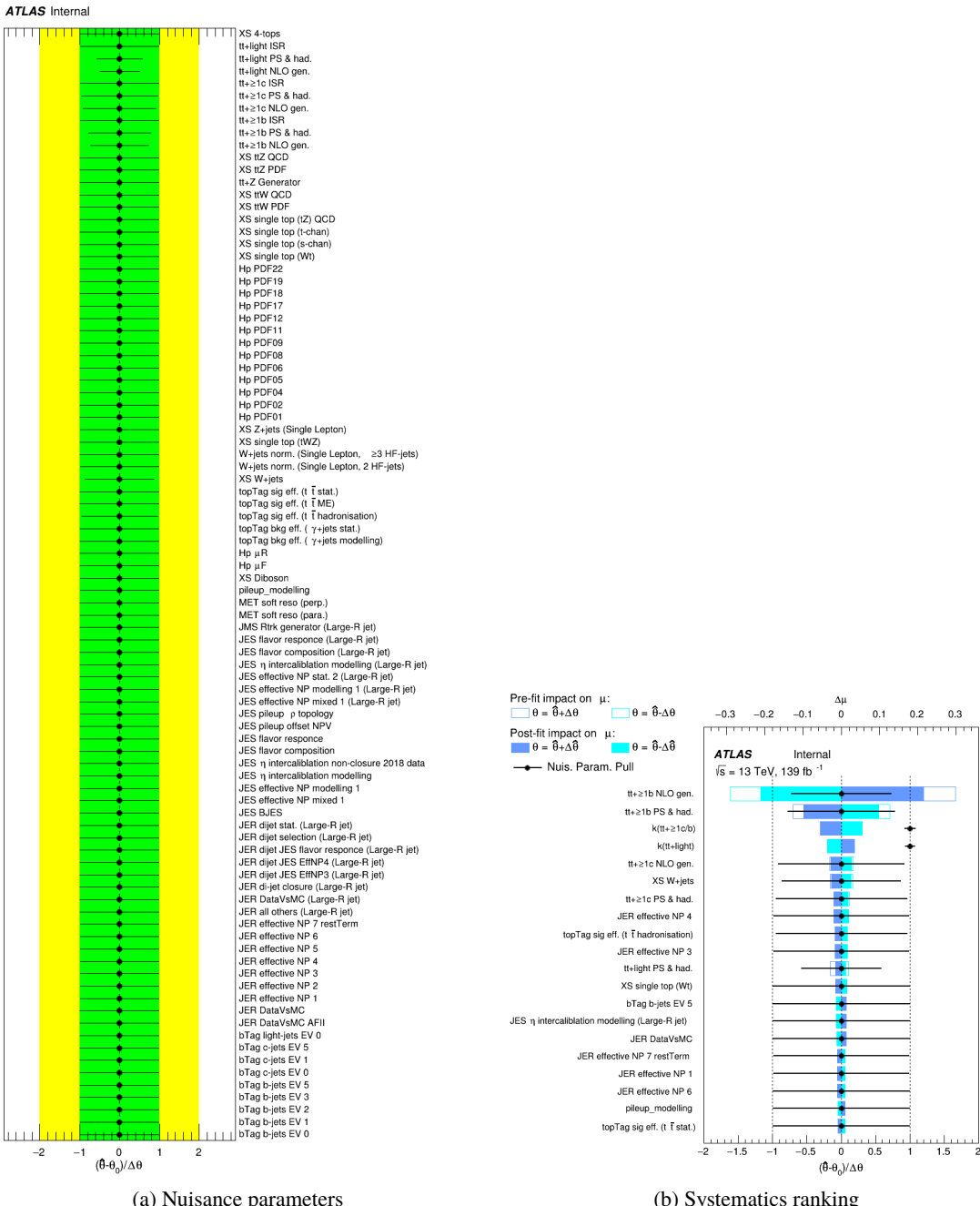
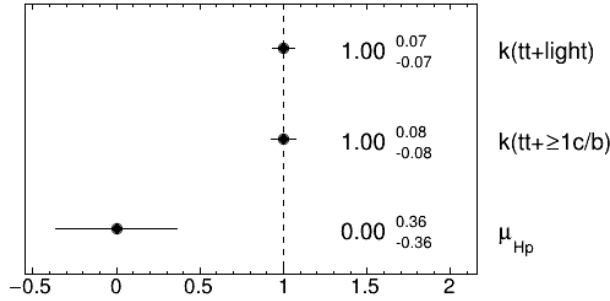


Figure 39: Nuisance parameters (left) and ranking plot (right) of the effect of various nuisance parameters before and after the fit for the 1400 GeV H^+ mass hypotheses.

ATLAS Internal

(a) Norm. factors

ATLAS Internal

	bTag b-jets EV 0	-0.2	-0.0	-0.5	-0.2	-0.1	0.1	1.3	-0.2	-2.5	2.7	1.6	1.0	0.1	3.6	-4.5	-0.4	51.4	-9.5
bTag b-jets EV 1	-0.2	100.0	-0.0	-0.4	-0.1	-0.1	0.0	1.0	-0.1	-1.9	1.7	1.0	0.7	0.1	2.8	-3.3	0.1	32.6	-6.0
bTag light-jets EV 0	-0.0	-0.0	100.0	0.1	0.0	-0.1	-0.1	-0.2	0.0	0.5	-0.5	1.0	0.5	0.0	-0.3	-1.2	0.7	26.2	-1.9
JES pileup p topology	-0.5	-0.4	0.1	100.0	-0.3	-0.2	-0.1	4.3	-0.2	-7.3	-1.2	-0.8	0.3	-0.9	5.4	-11.1	1.3	-41.4	11.0
active NP modelling 1 (Large-R jet)	-0.2	-0.1	0.0	-0.3	100.0	-0.0	0.0	0.7	-0.1	-1.5	0.9	0.1	0.3	-0.1	2.4	-1.9	-1.6	-21.4	-34.3
calibration modelling (Large-R jet)	-0.1	-0.1	-0.1	-0.2	-0.0	100.0	-0.0	0.8	-0.0	-0.4	1.4	3.3	0.9	0.3	1.4	-1.4	3.5	11.5	-21.0
topTag bkg eff. ($\gamma + \text{jets}$ modelling)	0.1	0.0	-0.1	-0.1	0.0	-0.0	100.0	-0.2	0.1	-0.2	-3.4	-0.7	-0.2	-0.6	-1.1	-3.5	2.2	-20.3	-1.3
topTag sig eff. ($t\bar{t}$ hadronisation)	1.3	1.0	-0.2	4.3	0.7	0.8	-0.2	100.0	0.7	13.0	-9.2	-7.9	-3.4	-0.4	-17.4	17.4	-4.3	-19.1	-56.7
topTag sig eff. ($t\bar{t}$ stat.)	-0.2	-0.1	0.0	-0.2	-0.1	-0.0	0.1	0.7	100.0	-1.1	2.7	1.0	0.4	-0.0	1.4	-1.4	-2.5	1.3	-25.6
XS W+jets	-2.5	-1.9	0.5	-7.3	-1.5	-0.4	-0.2	13.0	-1.1	100.0	-0.2	-5.5	6.2	-0.2	52.0	-42.4	-7.2	14.9	-62.7
$t\bar{t} + \geq 1b$ NLO gen.	2.7	1.7	-0.5	-1.2	0.9	1.4	-3.4	-9.2	2.7	-0.2	100.0	-52.6	-7.6	-5.6	3.1	-25.4	59.0	-3.1	3.3
$t\bar{t} + \geq 1b$ PS & had.	1.6	1.0	1.0	-0.8	0.1	3.3	-0.7	-7.9	1.0	-5.5	-52.6	100.0	-14.7	-4.8	-4.0	-5.9	-27.2	7.3	5.1
$t\bar{t} + \geq 1c$ NLO gen.	1.0	0.7	0.5	0.3	0.3	0.9	-0.2	-3.4	0.4	6.2	-7.6	-14.7	100.0	-7.1	-43.0	-5.0	-7.7	4.1	-3.2
$t\bar{t} + \geq 1c$ PS & had.	0.1	0.1	0.0	-0.9	-0.1	0.3	-0.6	-0.4	-0.0	-0.2	-5.6	-4.8	-7.1	100.0	-30.5	-21.3	-5.4	1.4	0.1
$t\bar{t} + \text{light}$ NLO gen.	3.6	2.8	-0.3	5.4	2.4	1.4	-1.1	-17.4	1.4	52.0	3.1	-4.0	-43.0	-30.5	100.0	-38.9	-1.6	13.9	-27.1
$t\bar{t} + \text{light}$ PS & had.	-4.5	-3.3	-1.2	-11.1	-1.9	-1.4	-3.5	17.4	-1.4	-42.4	-25.4	-5.9	-5.0	-21.3	-38.9	100.0	-3.7	-10.5	20.5
μ_{H_p}	-0.4	0.1	0.7	1.3	-1.6	3.5	2.2	-4.3	-2.5	-7.2	59.0	-27.2	-7.7	-5.4	-1.6	-3.7	100.0	-15.3	9.9
$k(t\bar{t} + \geq 1c/b)$	51.4	32.6	26.2	-41.4	-21.4	11.5	-20.3	-19.1	1.3	14.9	-3.1	7.3	4.1	1.4	13.9	-10.5	-15.3	100.0	-11.8
$k(t\bar{t} + \text{light})$	-9.5	-6.0	-1.9	11.0	-34.3	-21.0	-1.3	-66.7	-25.6	-62.7	3.3	5.1	-3.2	0.1	-27.1	20.5	9.9	-11.8	100.0

(b) Correlation matrix

Figure 40: Signal strength and normalization factors (top) and correlation matrix (bottom) for the 1400 GeV H^+ mass hypotheses.

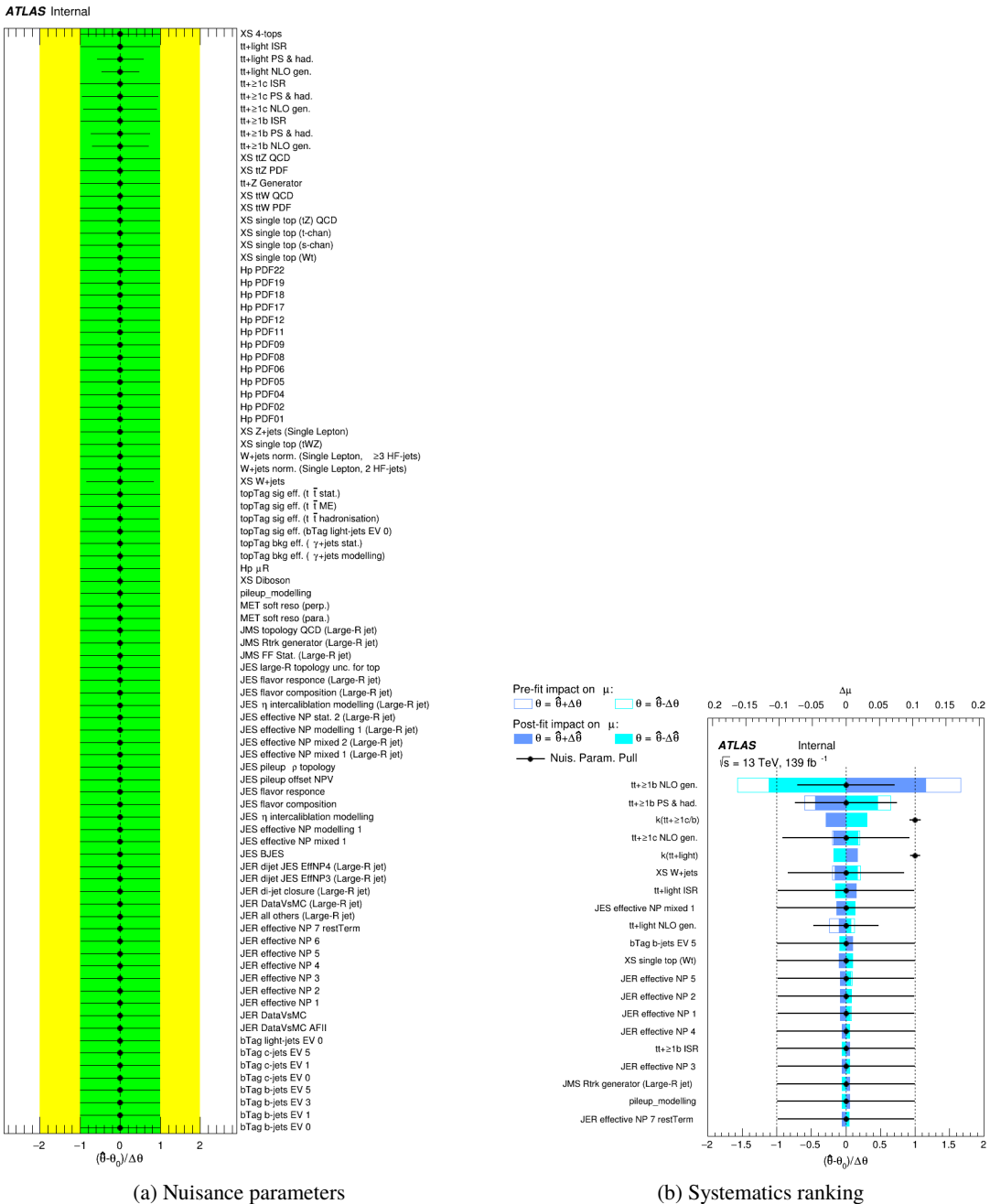
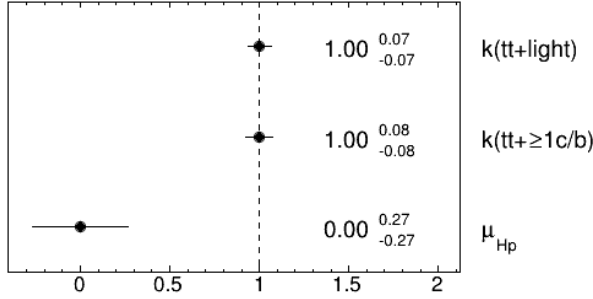


Figure 41: Nuisance parameters (left) and ranking plot (right) of the effect of various nuisance parameters before and after the fit for the 1600 GeV H^+ mass hypotheses.

ATLAS Internal

(a) Norm. factors

ATLAS Internal

	bTag b-jets EV 0	-0.2	0.0	-0.5	-0.1	-0.2	0.1	1.3	-0.2	-2.9	2.2	1.1	0.8	0.4	3.7	-4.5	0.3	51.6	-9.4
bTag b-jets EV 1	-0.2	100.0	0.0	-0.4	-0.1	-0.1	0.0	1.0	-0.1	-2.1	1.3	0.6	0.6	0.3	2.8	-3.3	0.5	32.8	-5.9
bTag light-jets EV 0	0.0	0.0	100.0	0.1	-0.0	-0.0	-0.0	-0.2	0.0	0.5	-0.8	0.4	0.0	-0.1	0.1	-0.9	1.9	26.4	-1.9
JES pileup p topology	-0.5	-0.4	0.1	100.0	-0.3	-0.2	-0.2	4.6	-0.1	-8.3	-2.0	-2.3	1.9	-0.7	4.1	-10.9	0.9	-41.8	11.4
active NP modelling 1 (Large-R jet)	-0.1	-0.1	-0.0	-0.3	100.0	-0.0	-0.1	0.5	0.0	-1.5	-1.8	-1.0	0.2	-0.3	3.2	-2.8	0.1	-21.6	-34.5
calibration modelling (Large-R jet)	-0.2	-0.1	-0.0	-0.2	-0.0	100.0	0.0	0.6	-0.1	-1.1	1.5	0.9	0.4	0.2	1.5	-1.9	-0.5	12.0	-20.8
topTag bkg eff. ($\gamma + \text{jets}$ modelling)	0.1	0.0	-0.0	-0.2	-0.1	0.0	100.0	-0.2	0.1	0.1	-3.3	-0.7	-0.3	-1.0	-0.7	-3.3	1.4	-20.3	-1.4
topTag sig eff. ($t\bar{t}$ hadronisation)	1.3	1.0	-0.2	4.6	0.5	0.6	-0.2	100.0	0.6	16.1	-9.7	-3.4	-5.2	-1.7	-14.5	16.1	-0.3	-19.5	-58.5
topTag sig eff. ($t\bar{t}$ stat.)	-0.2	-0.1	0.0	-0.1	0.0	-0.1	0.1	0.6	100.0	-1.1	2.2	1.3	0.3	0.1	1.7	-1.8	-2.0	1.2	-25.8
XS W+jets	-2.9	-2.1	0.5	-8.3	-1.5	-1.1	0.1	16.1	-1.1	100.0	4.7	-16.5	6.7	4.1	47.5	-36.3	-6.6	13.5	-62.1
$t\bar{t} + \geq 1b$ NLO gen.	2.2	1.3	-0.8	-2.0	-1.8	1.5	-3.3	-9.7	2.2	4.7	100.0	-54.8	-8.5	-12.5	11.6	-27.9	44.2	1.6	1.3
$t\bar{t} + \geq 1b$ PS & had.	1.1	0.6	0.4	-2.3	-1.0	0.9	-0.7	-3.4	1.3	-16.5	-54.8	100.0	-14.6	0.6	-18.9	5.4	-17.7	2.7	10.8
$t\bar{t} + \geq 1c$ NLO gen.	0.8	0.6	0.0	1.9	0.2	0.4	-0.3	-5.2	0.3	6.7	-8.5	-14.6	100.0	-7.6	-44.8	-15.0	-6.9	3.1	-2.1
$t\bar{t} + \geq 1c$ PS & had.	0.4	0.3	-0.1	-0.7	-0.3	0.2	-1.0	-1.7	0.1	4.1	-12.5	0.6	-7.6	100.0	-27.2	-26.6	-0.5	1.9	-1.9
$t\bar{t} + \text{light}$ NLO gen.	3.7	2.8	0.1	4.1	3.2	1.5	-0.7	-14.5	1.7	47.5	11.6	-18.9	-44.8	-27.2	100.0	-25.8	-3.6	13.3	-25.4
$t\bar{t} + \text{light}$ PS & had.	-4.5	-3.3	-0.9	-10.9	-2.8	-1.9	-3.3	16.1	-1.8	-36.3	-27.9	5.4	-15.0	-26.6	-25.8	100.0	1.8	-9.7	17.4
μ_{H_p}	0.3	0.5	1.9	0.9	0.1	-0.5	1.4	-0.3	-2.0	-6.6	44.2	-17.7	-6.9	-0.5	-3.6	1.8	100.0	-11.6	6.8
$k(t\bar{t} + \geq 1c/b)$	51.6	32.8	26.4	-41.8	-21.6	12.0	-20.3	-19.5	1.2	13.5	1.6	2.7	3.1	1.9	13.3	-9.7	-11.6	100.0	-10.4
$k(t\bar{t} + \text{light})$	-9.4	-5.9	-1.9	11.4	-34.5	-20.8	-1.4	-58.5	-25.8	-62.1	1.3	10.8	-2.1	-1.9	-25.4	17.4	6.8	-10.4	100.0

(b) Correlation matrix

Figure 42: Signal strength and normalization factors (top) and correlation matrix (bottom) for the 1600 GeV H^+ mass hypotheses.

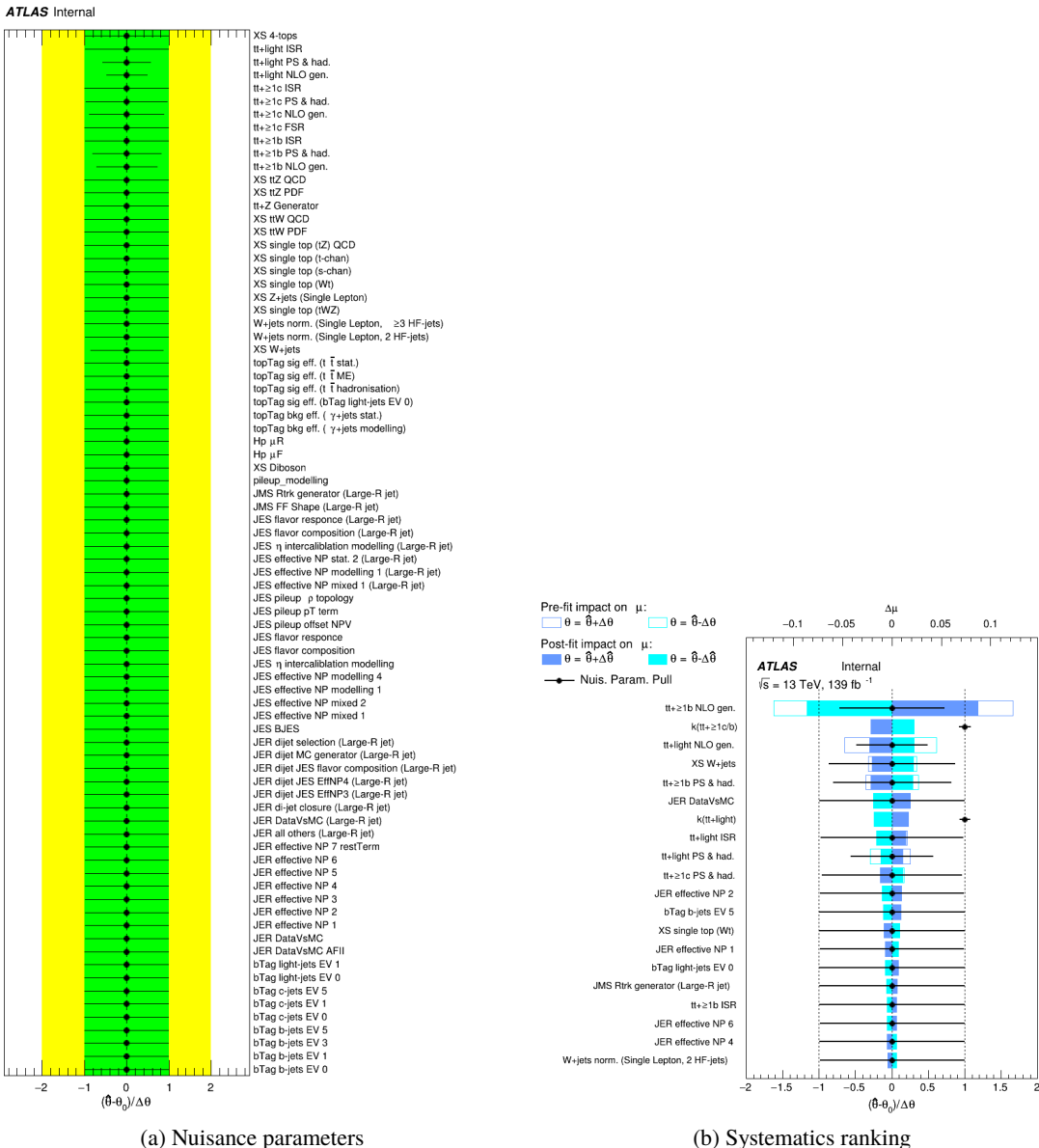
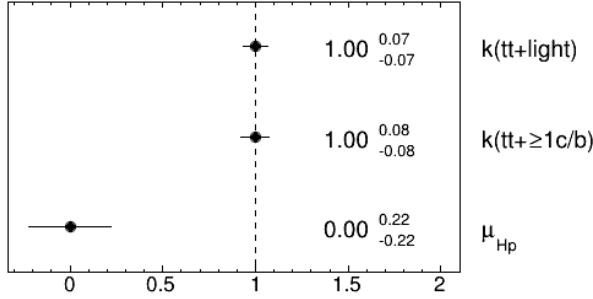


Figure 43: Nuisance parameters (left) and ranking plot (right) of the effect of various nuisance parameters before and after the fit for the 1800 GeV H^+ mass hypotheses.

ATLAS Internal

(a) Norm. factors

ATLAS Internal

	bTag b-jets EV 0	-0.2	-0.0	-0.4	-0.2	-0.2	0.1	1.1	-0.2	-2.4	1.6	1.1	1.3	0.3	3.2	-5.0	1.0	51.6	-9.5
bTag b-jets EV 1	-0.2	100.0	-0.0	-0.3	-0.1	-0.1	0.1	0.8	-0.1	-1.8	1.1	0.7	0.9	0.2	2.5	-3.7	0.7	32.8	-6.0
bTag light-jets EV 0	-0.0	-0.0	100.0	0.1	0.0	-0.0	-0.0	-0.1	-0.0	0.4	-0.6	0.1	0.1	0.0	-0.4	-0.3	2.9	26.3	-1.8
JES pileup p topology	-0.4	-0.3	0.1	100.0	-0.3	-0.1	0.2	3.1	-0.1	-6.4	1.6	-0.8	0.4	0.3	1.9	-13.8	1.2	-41.3	11.0
active NP modelling 1 (Large-R jet)	-0.2	-0.1	0.0	-0.3	100.0	-0.1	0.1	0.7	-0.1	-1.5	1.2	0.4	0.5	0.2	2.1	-2.2	-2.0	-21.6	-34.4
calibration modelling (Large-R jet)	-0.2	-0.1	-0.0	-0.1	-0.1	100.0	0.0	0.6	-0.1	-0.9	1.2	0.9	0.7	0.2	1.2	-2.0	-0.1	12.0	-20.7
topTag bkg eff. (γ+jets modelling)	0.1	0.1	-0.0	0.2	0.1	0.0	100.0	-0.5	0.1	0.5	-3.1	-0.4	-0.7	-1.0	-1.7	-2.9	1.7	-20.2	-1.6
topTag sig eff. (t̄t hadronisation)	1.1	0.8	-0.1	3.1	0.7	0.6	-0.5	100.0	0.6	12.3	-10.7	-5.9	-5.4	-1.7	-13.9	23.9	1.4	-20.0	-56.7
topTag sig eff. (t̄t stat.)	-0.2	-0.1	-0.0	-0.1	-0.1	-0.1	0.1	0.6	100.0	-0.9	1.7	1.1	0.8	0.2	1.4	-1.8	-1.6	1.1	-25.8
XS W+jets	-2.4	-1.8	0.4	-6.4	-1.5	-0.9	0.5	12.3	-0.9	100.0	2.2	-5.4	6.0	2.0	48.0	-51.3	-9.8	14.5	-62.2
tt+≥1b NLO gen.	1.6	1.1	-0.6	1.6	1.2	1.2	-3.1	-10.7	1.7	2.2	100.0	-51.2	-12.9	-12.2	0.2	-24.8	39.5	-0.2	2.8
tt+≥1b PS & had.	1.1	0.7	0.1	-0.8	0.4	0.9	-0.4	-5.9	1.1	-5.4	-51.2	100.0	-18.2	-5.2	-8.3	-1.5	-9.8	2.6	5.0
tt+≥1c NLO gen.	1.3	0.9	0.1	0.4	0.5	0.7	-0.7	-5.4	0.8	6.0	-12.9	-18.2	100.0	-6.8	-39.7	-2.5	-0.9	3.5	-2.2
tt+≥1c PS & had.	0.3	0.2	0.0	0.3	0.2	0.2	-1.0	-1.7	0.2	2.0	-12.2	-5.2	-6.8	100.0	-27.3	-18.2	-5.2	1.4	-0.8
tt+light NLO gen.	3.2	2.5	-0.4	1.9	2.1	1.2	-1.7	-13.9	1.4	48.0	0.2	-8.3	-39.7	-27.3	100.0	-31.9	-10.4	14.4	-26.2
tt+light PS & had.	-5.0	-3.7	-0.3	-13.8	-2.2	-2.0	-2.9	23.9	-1.8	-51.3	-24.8	-1.5	-2.5	-18.2	-31.9	100.0	5.2	-13.5	23.1
μ_{H_p}	1.0	0.7	2.9	1.2	-2.0	-0.1	1.7	1.4	-1.6	-9.8	39.5	-9.8	-0.9	-5.2	-10.4	5.2	100.0	-10.0	8.1
$k(\text{tt+} \geq 1\text{c/b})$	51.6	32.8	26.3	-41.3	-21.6	12.0	-20.2	-20.0	1.1	14.5	-0.2	2.6	3.5	1.4	14.4	-13.5	-10.0	100.0	-10.8
$k(\text{tt+light})$	-9.5	-6.0	-1.8	11.0	-34.4	-20.7	-1.6	-66.7	-25.8	-62.2	2.8	5.0	-2.2	-0.8	-26.2	23.1	8.1	-10.8	100.0

(b) Correlation matrix

Figure 44: Signal strength and normalization factors (top) and correlation matrix (bottom) for the 1800 GeV H^+ mass hypotheses.

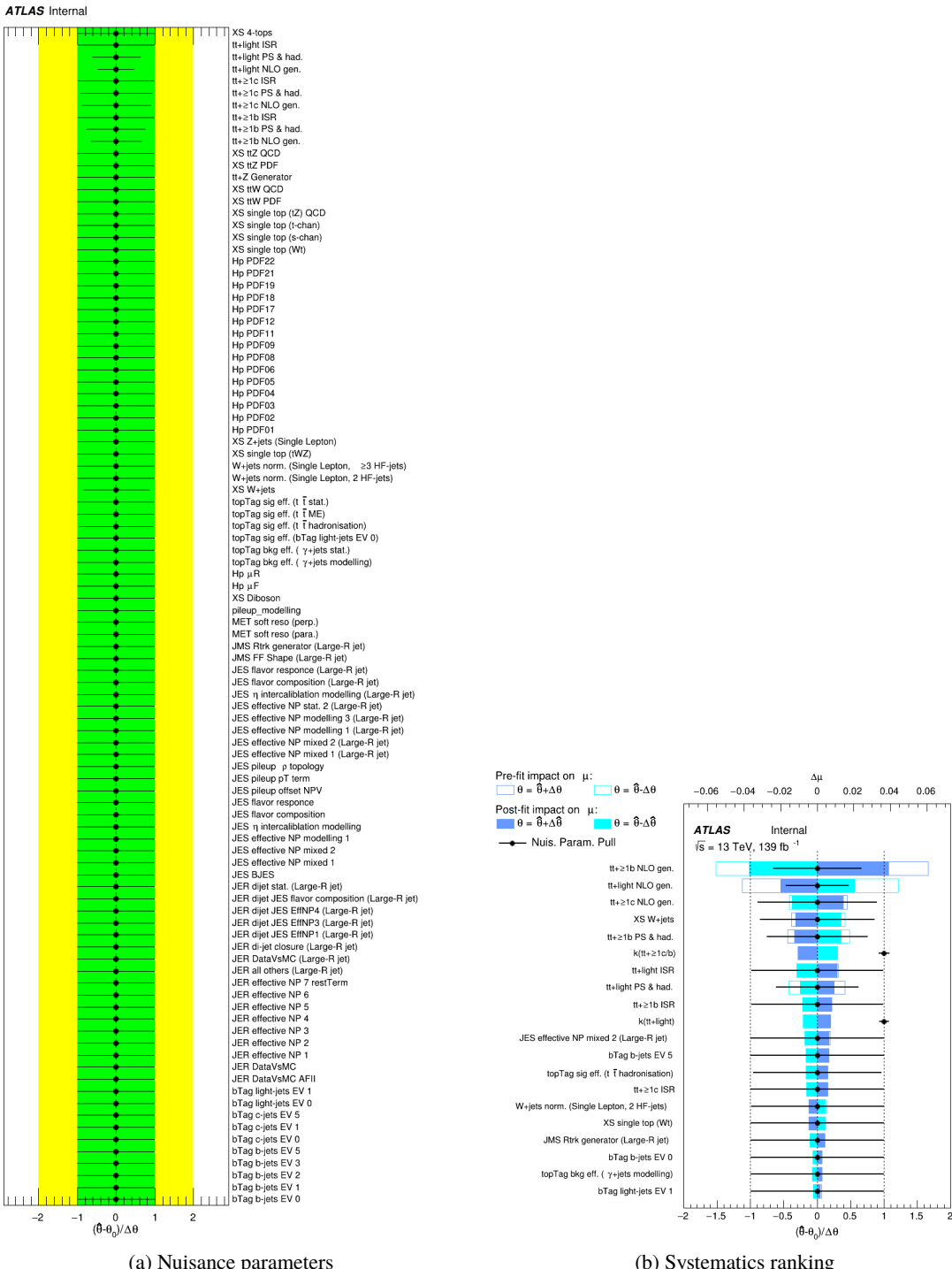


Figure 45: Nuisance parameters (left) and ranking plot (right) of the effect of various nuisance parameters before and after the fit for the 2000 GeV H^+ mass hypotheses.

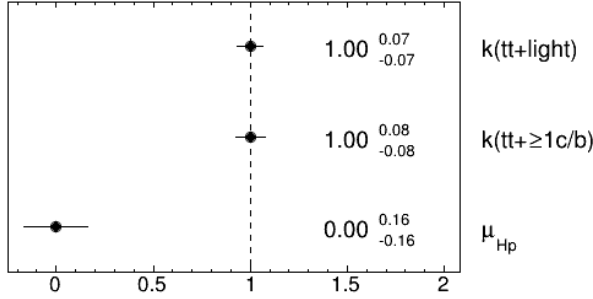
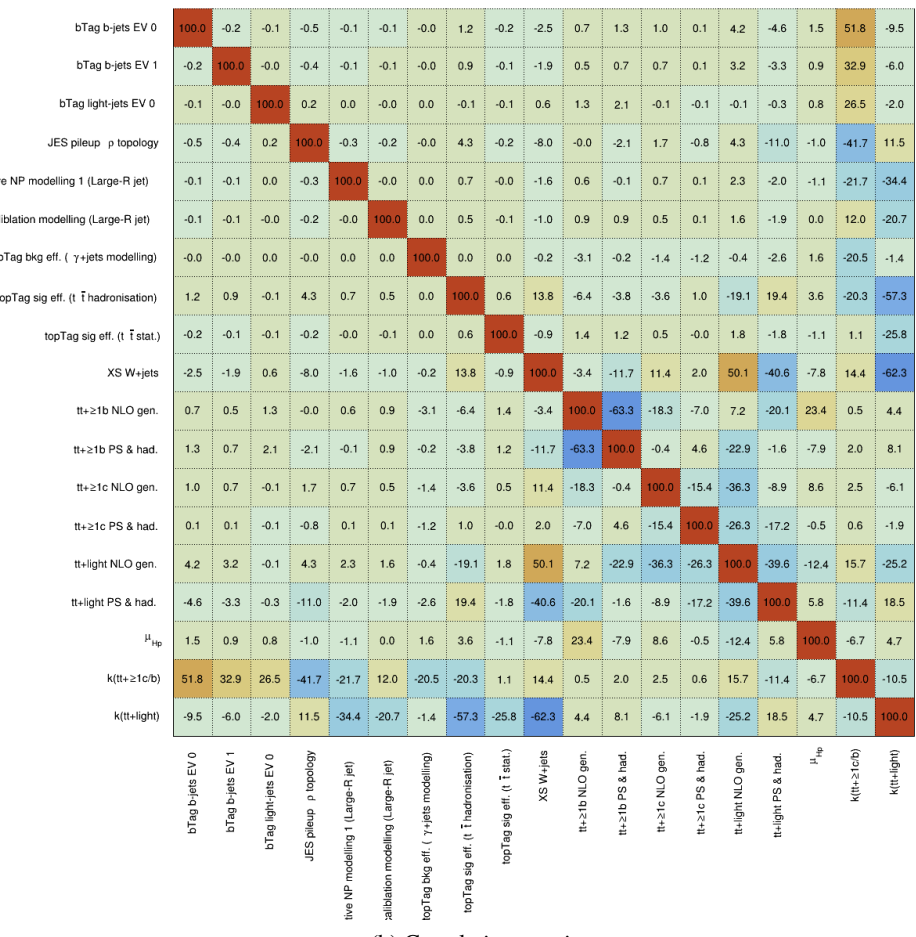
ATLAS Internal**ATLAS Internal**

Figure 46: Signal strength and normalization factors (top) and correlation matrix (bottom) for the 2000 GeV H^+ mass hypotheses.

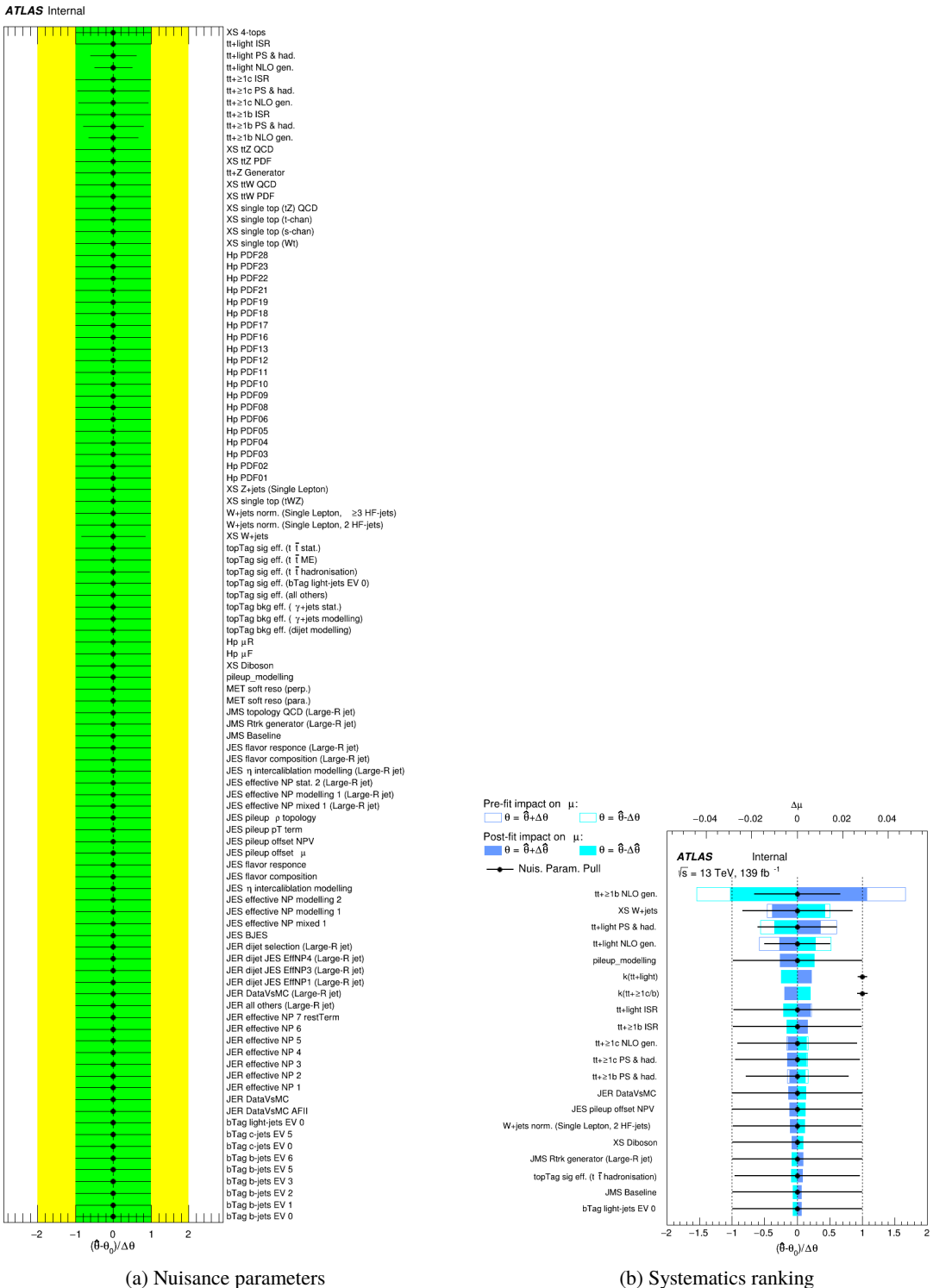
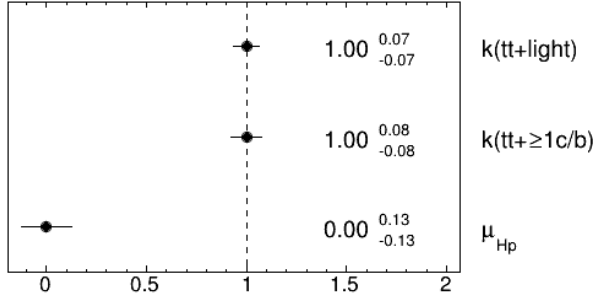
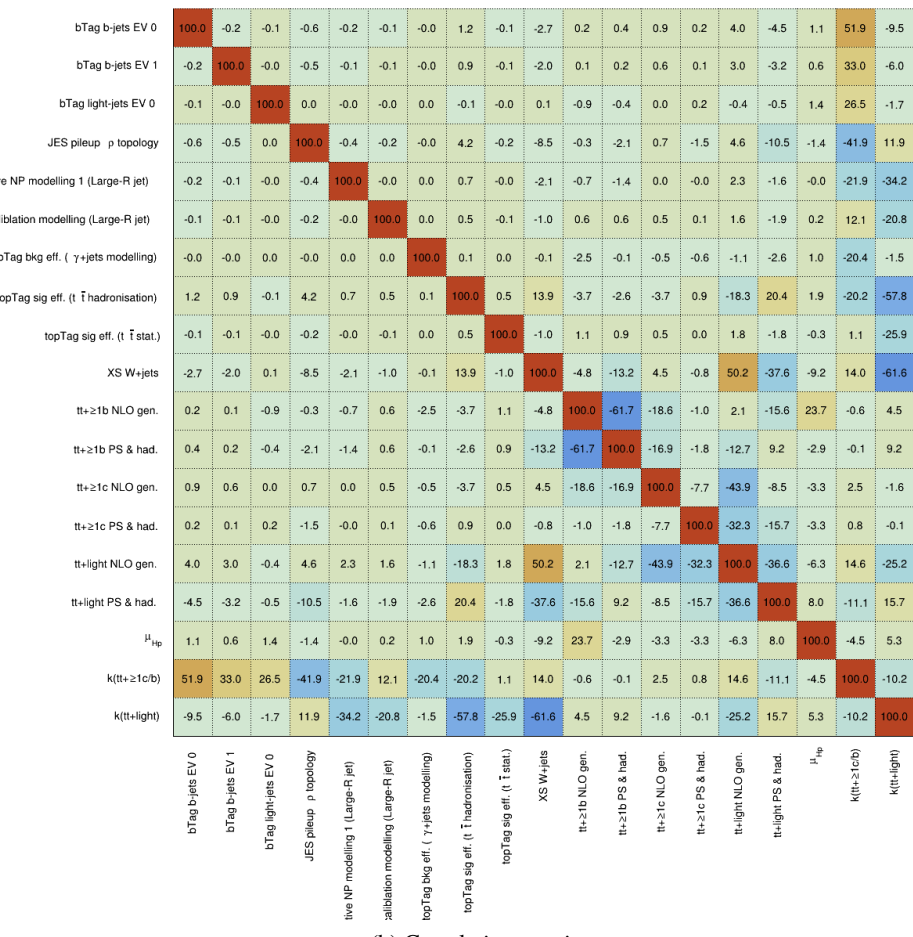


Figure 47: Nuisance parameters (left) and ranking plot (right) of the effect of various nuisance parameters before and after the fit for the 2500 GeV H^+ mass hypotheses.

ATLAS Internal**ATLAS Internal****(b) Correlation matrix**Figure 48: Signal strength and normalization factors (top) and correlation matrix (bottom) for the 2500 GeV H^+ mass hypotheses.

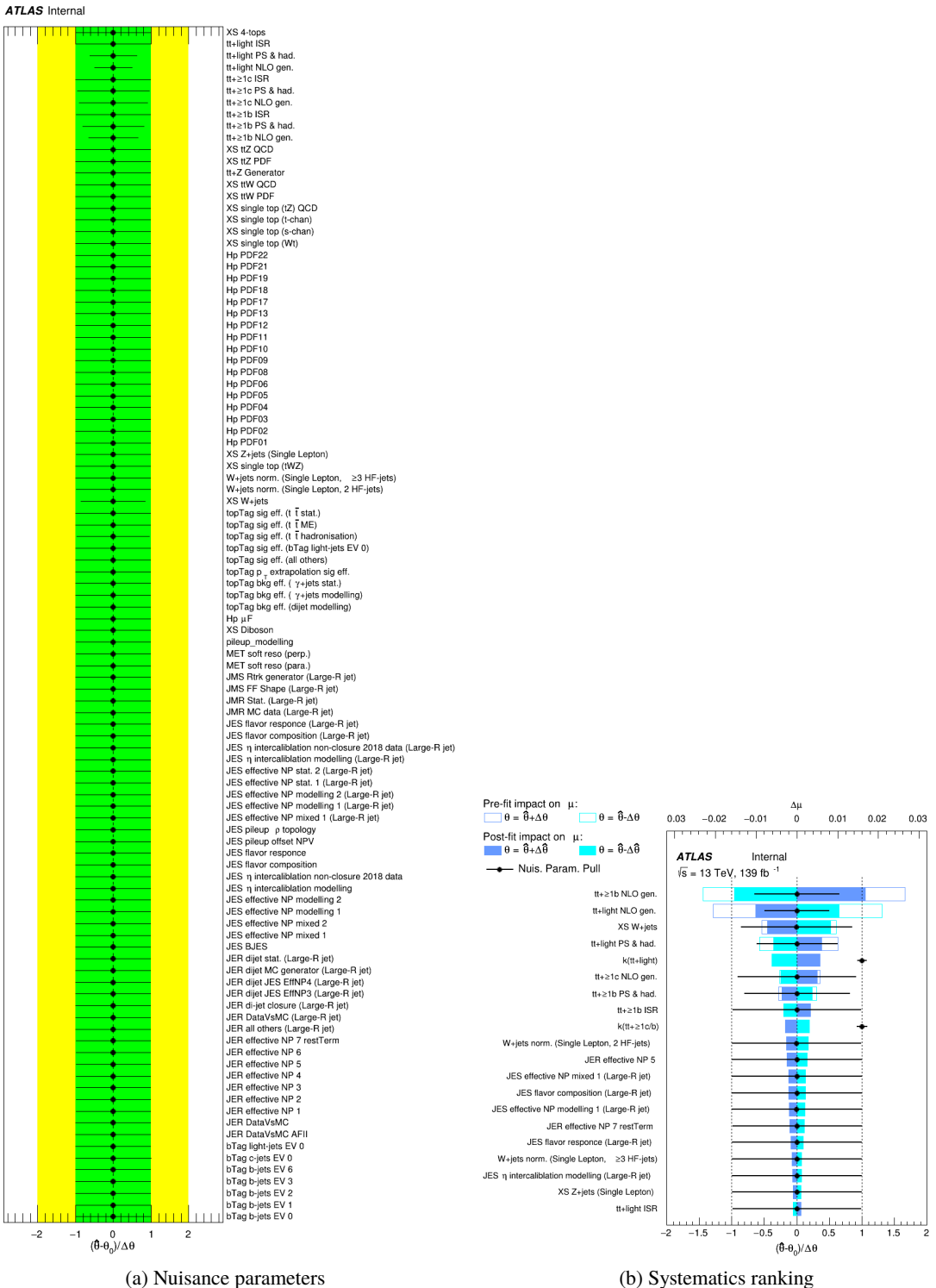
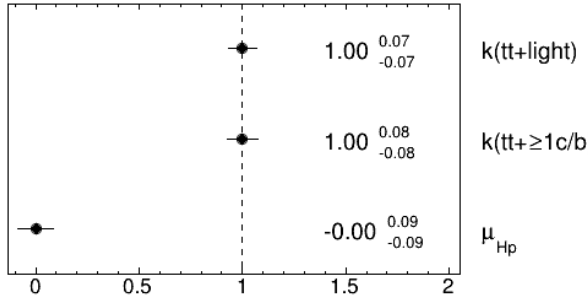


Figure 49: Nuisance parameters (left) and ranking plot (right) of the effect of various nuisance parameters before and after the fit for the 3000 GeV H^+ mass hypotheses.

ATLAS Internal

(a) Norm. factors

ATLAS Internal

	bTag b-jets EV 0	-0.2	-0.1	-0.5	-0.1	-0.1	-0.0	1.1	-0.1	-2.5	-0.8	0.6	0.8	0.3	4.1	-5.0	52.0	-9.5
bTag b-jets EV 1	-0.2	100.0	-0.0	-0.4	-0.1	-0.1	-0.0	0.9	-0.1	-2.0	-0.6	0.3	0.6	0.2	3.1	-3.5	33.0	-6.0
bTag light-jets EV 0	-0.1	-0.0	100.0	-0.0	0.0	0.0	-0.0	-0.0	-0.5	-3.5	-1.6	-0.6	0.2	-0.4	-0.6	26.5	-1.4	
JES pileup p topology	-0.5	-0.4	-0.0	100.0	-0.4	-0.2	-0.2	4.4	-0.2	-8.8	-2.7	-3.3	1.2	-1.4	4.2	-10.2	-42.0	11.9
active NP modelling 1 (Large-R jet)	-0.1	-0.1	0.0	-0.4	100.0	-0.1	-0.0	0.7	-0.1	-1.7	0.6	-0.1	0.3	-0.1	2.3	-1.8	-21.8	-34.3
calibration modelling (Large-R jet)	-0.1	-0.1	0.0	-0.2	-0.1	100.0	0.0	0.5	-0.1	-0.9	1.7	1.3	0.5	0.1	1.6	-2.0	12.2	-20.7
topTag bkg eff. ($\gamma + \text{jets}$ modelling)	-0.0	-0.0	-0.0	-0.2	-0.0	0.0	100.0	0.2	0.0	-0.6	-2.0	-1.1	-0.6	-0.7	-1.5	-2.1	-20.5	-1.2
topTag sig eff. ($t\bar{t}$ hadronisation)	1.1	0.9	-0.0	4.4	0.7	0.5	0.2	100.0	0.5	14.7	-1.1	0.4	-4.1	0.8	-17.9	19.5	-20.1	-57.8
topTag sig eff. ($t\bar{t}$ stat.)	-0.1	-0.1	-0.0	-0.2	-0.1	-0.1	0.0	0.5	100.0	-1.0	0.8	0.8	0.4	0.1	1.8	-2.0	1.1	-25.7
XS W+jets	-2.5	-2.0	-0.5	-8.8	-1.7	-0.9	-0.6	14.7	-1.0	100.0	-12.0	12.4	6.9	-0.1	50.1	-36.9	14.0	-62.4
$t\bar{t} + \geq 1b$ NLO gen.	-0.8	-0.6	-3.5	-2.7	0.6	1.7	-2.0	-1.1	0.8	-12.0	100.0	-60.4	-23.6	-3.2	-3.2	-5.6	-2.8	7.1
$t\bar{t} + \geq 1b$ PS & had.	0.6	0.3	-1.6	-3.3	-0.1	1.3	-1.1	0.4	0.8	-12.4	-60.4	100.0	-10.6	-2.3	-17.4	15.0	-0.2	6.6
$t\bar{t} + \geq 1c$ NLO gen.	0.8	0.6	-0.6	1.2	0.3	0.5	-0.6	-4.1	0.4	6.9	-23.6	-10.6	100.0	-8.0	-41.5	-11.7	2.1	-2.8
$t\bar{t} + \geq 1c$ PS & had.	0.3	0.2	0.2	-1.4	-0.1	0.1	-0.7	0.8	0.1	-0.1	-3.2	-2.3	-8.0	100.0	-31.3	-16.8	1.0	-0.6
tt+light NLO gen.	4.1	3.1	-0.4	4.2	2.3	1.6	-1.5	-17.9	1.8	50.1	-3.2	-17.4	-41.5	-31.3	100.0	-35.3	15.0	-25.5
tt+light PS & had.	-5.0	-3.5	-0.6	-10.2	-1.8	-2.0	-2.1	19.5	-2.0	-36.9	-5.6	15.0	-11.7	-16.8	-35.3	100.0	-11.5	16.0
$k(t\bar{t} + \geq 1c/b)$	52.0	33.0	26.5	-42.0	-21.8	12.2	-20.5	-20.1	1.1	14.0	-2.8	-0.2	2.1	1.0	15.0	-11.5	100.0	-10.3
$k(t\bar{t} + \text{light})$	-9.5	-6.0	-1.4	11.9	-34.3	-20.7	-1.2	-57.8	-25.7	-62.4	7.1	6.6	-2.8	-0.6	-25.5	16.0	-10.3	100.0

(b) Correlation matrix

Figure 50: Signal strength and normalization factors (top) and correlation matrix (bottom) for the 3000 GeV H^+ mass hypotheses.

568 **5.4 Post-fit plots for Asimov fit**

569 Figures 51 to 58 show the post-fit distributions of the BDT output and H_T^{jets} for the fits using Asimov
570 dataset under all H^+ mass hypotheses.

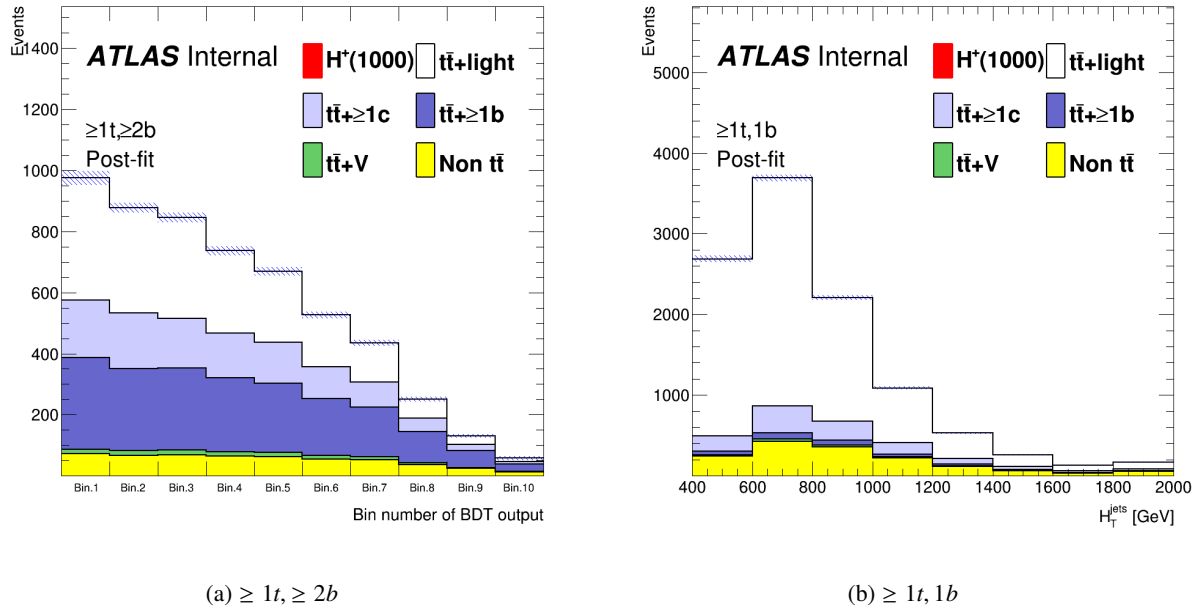


Figure 51: Post-fit distribution of BDT output and H_T^{jets} for the fits using Asimov dataset under the 1000 GeV H^+ mass hypotheses.

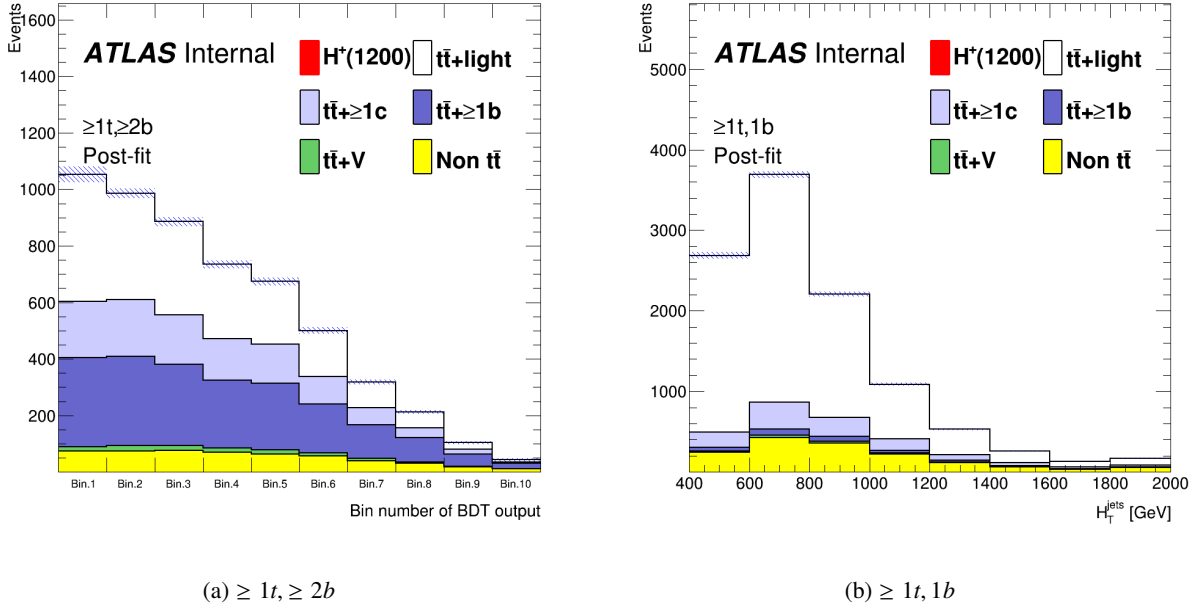


Figure 52: Post-fit distribution of BDT output and H_T^{jets} for the fits using Asimov dataset under the 1200 GeV H^+ mass hypotheses.

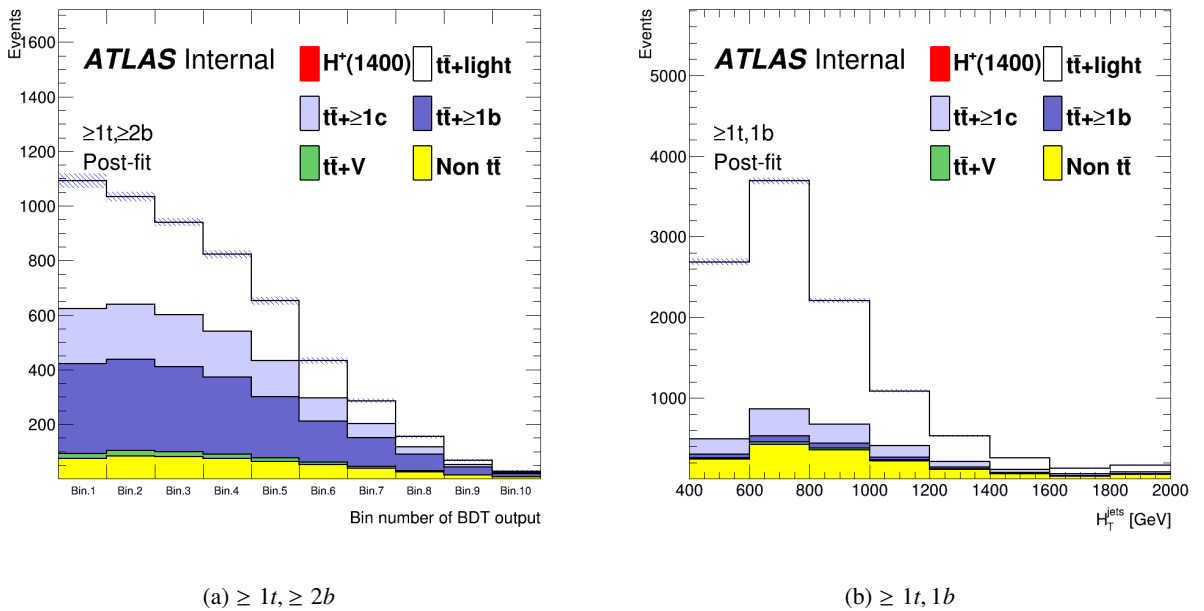


Figure 53: Post-fit distribution of BDT output and H_T^{jets} for the fits using Asimov dataset under the 1400 GeV H^+ mass hypotheses.

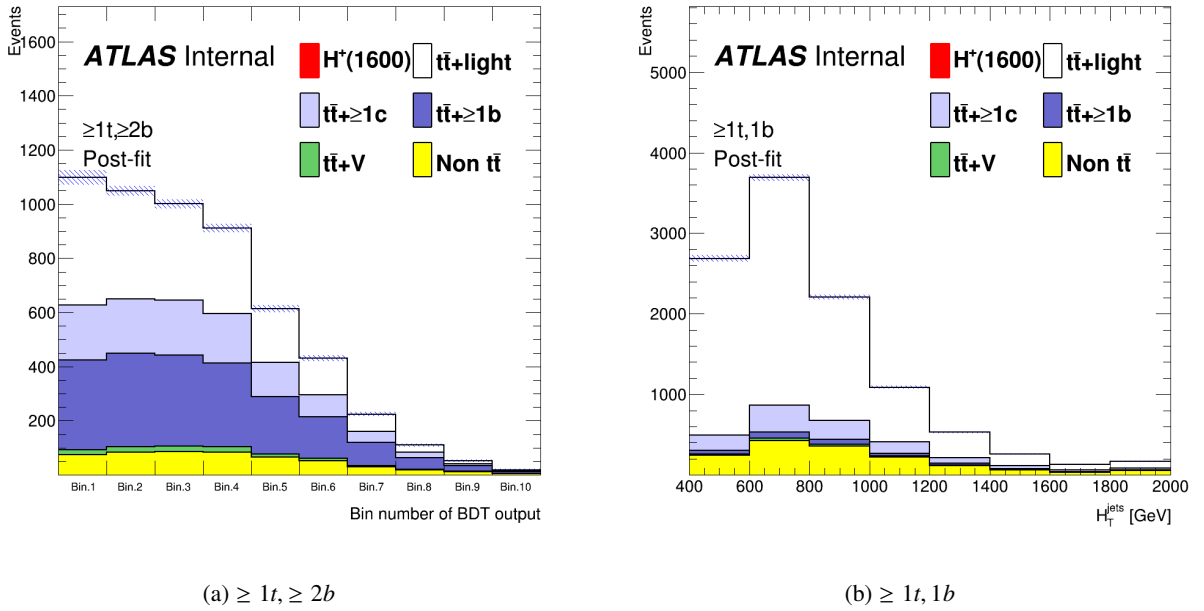


Figure 54: Post-fit distribution of BDT output and H_T^{jets} for the fits using Asimov dataset under the 1600 GeV H^+ mass hypotheses.

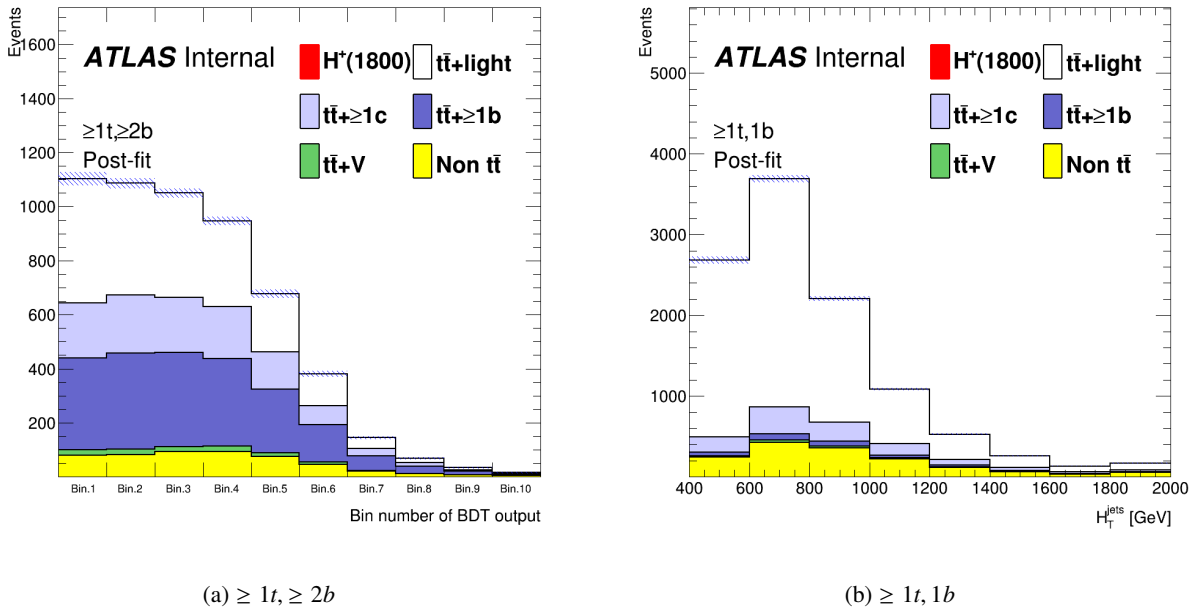


Figure 55: Post-fit distribution of BDT output and H_T^{jets} for the fits using Asimov dataset under the 1800 GeV H^+ mass hypotheses.

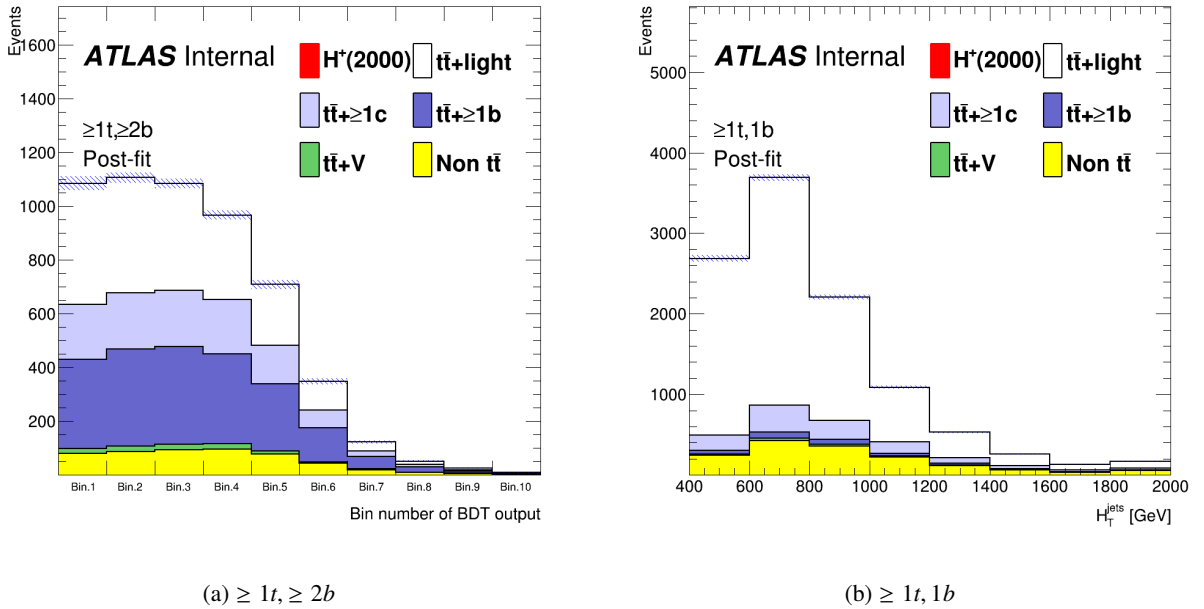


Figure 56: Post-fit distribution of BDT output and H_T^{jets} for the fits using Asimov dataset under the 2000 GeV H^+ mass hypotheses.

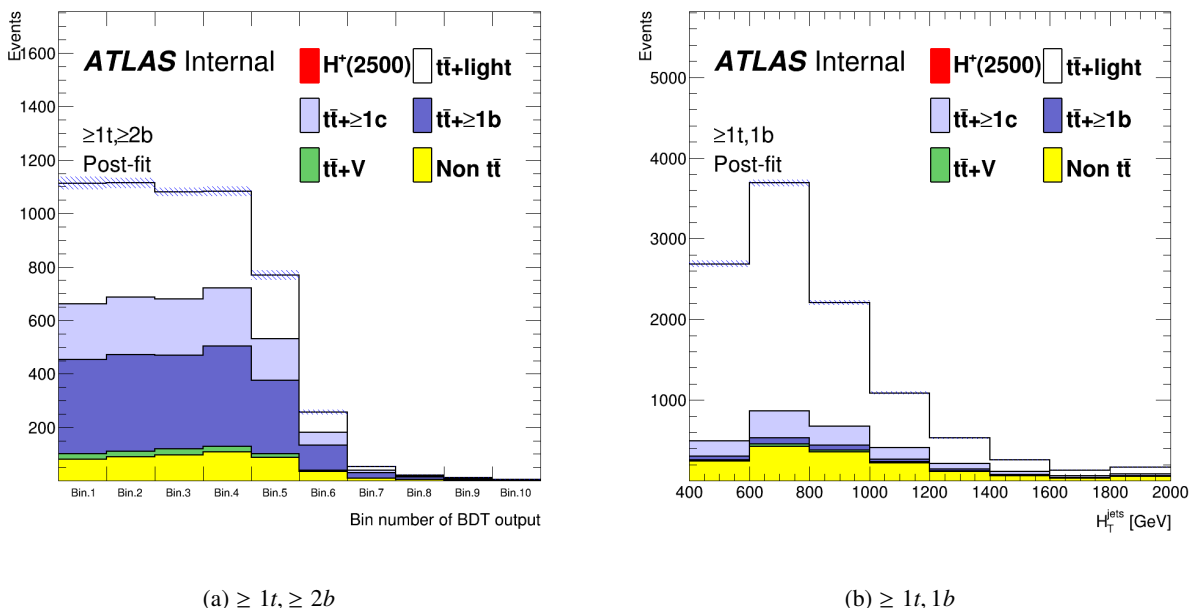


Figure 57: Post-fit distribution of BDT output and H_T^{jets} for the fits using Asimov dataset under the 2500 GeV H^+ mass hypotheses.

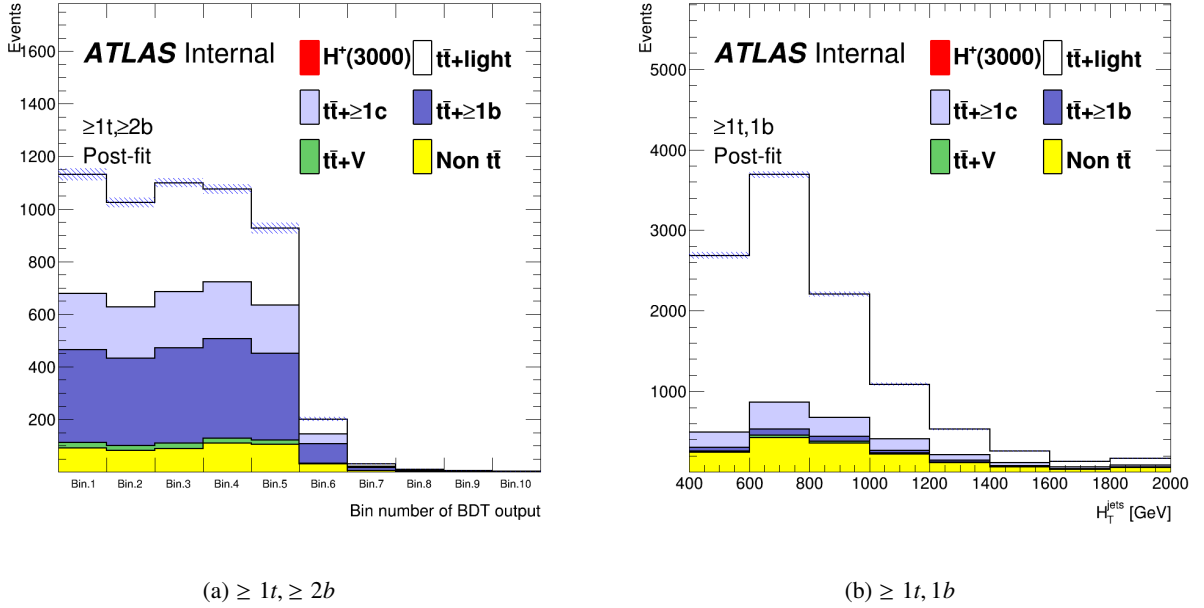


Figure 58: Post-fit distribution of BDT output and H_T^{jets} for the fits using Asimov dataset under the 3000 GeV H^+ mass hypotheses.

571 5.5 Asimov fit results summary

572 Figure 59 shows the fitted signal strength and $t\bar{t} + \text{light}$ and $t\bar{t} + \geq 1c/b$ normalisation factors as a function
 573 of the H^+ mass hypothesis of the Asimov fit.

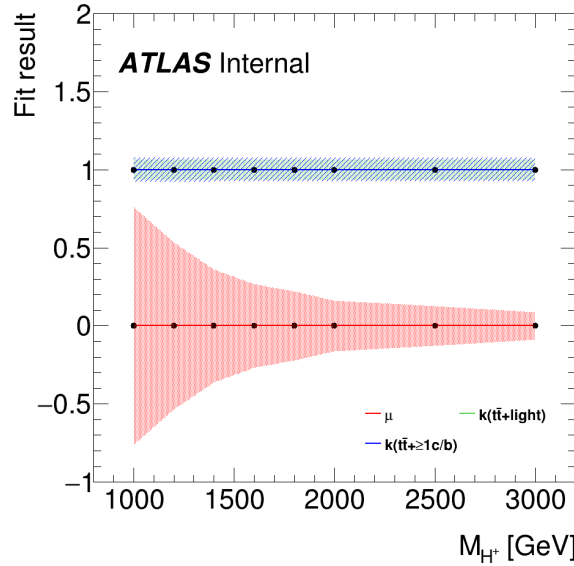


Figure 59: Fitted signal strength and $t\bar{t} + \text{light}$ and $t\bar{t} + \geq 1c/b$ normalisation factors as a function of the H^+ mass hypothesis of the Asimov fit

⁵⁷⁴ **5.6 Upper cross-section limits as a function of the H^+ mass**

⁵⁷⁵ The 95% confidence level (CL) upper limit for the production of $H^+ \rightarrow tb$ in association with a top quark
⁵⁷⁶ and a bottom quark using the CL_S method is shown in Figure 60.

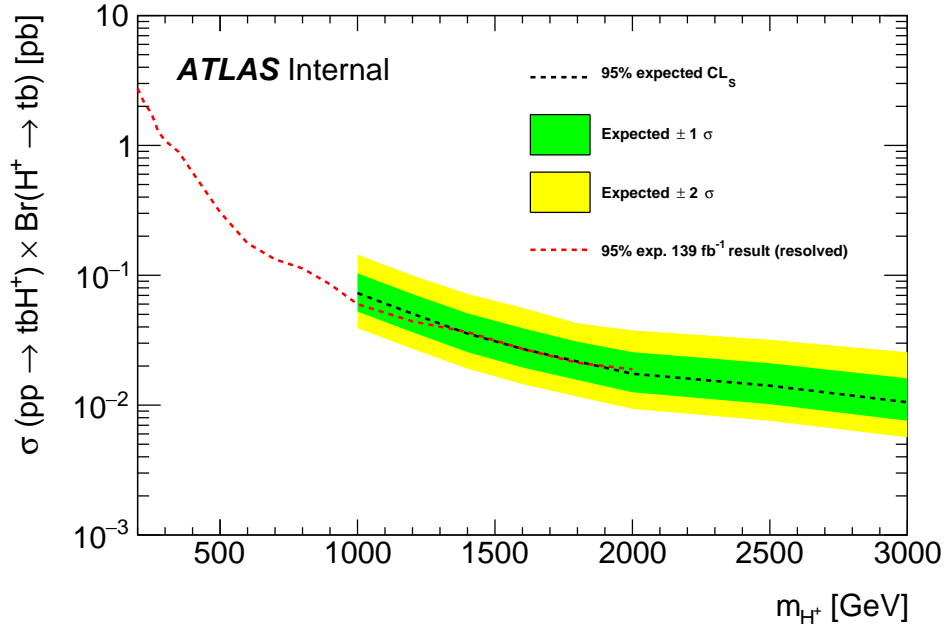


Figure 60: Expected limit for the production of $H^+ \rightarrow tb$ in association with a top quark and a bottom quark. The bands surrounding the expected limit show the 68% and 95% confidence intervals. The expected limit from ATLAS search using Run2 full data with resolved channel is also shown[24].

577 References

- 578 [1] ATLAS Collaboration, *Electron reconstruction and identification efficiency measurements with the*
 579 *ATLAS detector using the 2011 LHC proton–proton collision data*, *Eur. Phys. J. C* **74** (2014) 2941,
 580 arXiv: [1404.2240 \[hep-ex\]](https://arxiv.org/abs/1404.2240) (cit. on p. 6).
- 581 [2] ATLAS Collaboration, *Electron efficiency measurements with the ATLAS detector using the 2015*
 582 *LHC proton–proton collision data*, ATLAS-CONF-2016-024, 2016, URL: <https://cds.cern.ch/record/2157687> (cit. on p. 6).
- 584 [3] *Lepton isolation recommendations*, URL: <https://twiki.cern.ch/twiki/bin/viewauth/AtlasProtected/IsolationSelectionTool> (cit. on p. 6).
- 585 [4] ATLAS Collaboration, *Muon reconstruction performance of the ATLAS detector in proton–proton*
 586 *collision data at $\sqrt{s} = 13 \text{ TeV}$* , *Eur. Phys. J. C* **76** (2016) 292, arXiv: [1603.05598 \[hep-ex\]](https://arxiv.org/abs/1603.05598) (cit. on
 587 pp. 6, 35, 37).
- 589 [5] ATLAS Collaboration, *Reconstruction, Energy Calibration, and Identification of Hadronically*
 590 *Decaying Tau Leptons in the ATLAS Experiment for Run-2 of the LHC*, ATL-PHYS-PUB-2015-045,
 591 2015, URL: <https://cds.cern.ch/record/2064383> (cit. on p. 6).
- 592 [6] M. Cacciari, G. P. Salam and G. Soyez, *The anti- k_t jet clustering algorithm*, *JHEP* **04** (2008) 063,
 593 arXiv: [0802.1189 \[hep-ph\]](https://arxiv.org/abs/0802.1189) (cit. on p. 6).
- 594 [7] ATLAS Collaboration, *Jet reconstruction and performance using particle flow with the ATLAS*
 595 *Detector*, *Eur. Phys. J. C* **77** (2017) 466, arXiv: [1703.10485 \[hep-ex\]](https://arxiv.org/abs/1703.10485) (cit. on p. 6).
- 596 [8] ATLAS Collaboration, *Jet energy scale and resolution measured in proton–proton collisions at*
 597 *$\sqrt{s} = 13 \text{ TeV}$ with the ATLAS detector*, (2020), arXiv: [2007.02645 \[hep-ex\]](https://arxiv.org/abs/2007.02645) (cit. on p. 6).
- 598 [9] ATLAS Collaboration, *Performance of pile-up mitigation techniques for jets in pp collisions at*
 599 *$\sqrt{s} = 8 \text{ TeV}$ using the ATLAS detector*, *Eur. Phys. J. C* **76** (2016) 581, arXiv: [1510.03823 \[hep-ex\]](https://arxiv.org/abs/1510.03823)
 600 (cit. on pp. 6, 37).
- 601 [10] ATLAS Collaboration, *ATLAS b-jet identification performance and efficiency measurement with*
 602 *$t\bar{t}$ events in pp collisions at $\sqrt{s} = 13 \text{ TeV}$* , *Eur. Phys. J. C* **79** (2019) 970, arXiv: [1907.05120 \[hep-ex\]](https://arxiv.org/abs/1907.05120) (cit. on pp. 6, 38).
- 604 [11] ATLAS Collaboration, *Topological cell clustering in the ATLAS calorimeters and its performance*
 605 *in LHC Run 1*, *Eur. Phys. J. C* **77** (2017) 490, arXiv: [1603.02934 \[hep-ex\]](https://arxiv.org/abs/1603.02934) (cit. on p. 7).
- 606 [12] D. Krohn, J. Thaler and L.-T. Wang, *Jet trimming*, *Journal of High Energy Physics* **2010** (2010) 84,
 607 URL: [https://link.springer.com/article/10.1007/JHEP02\(2010\)084](https://link.springer.com/article/10.1007/JHEP02(2010)084), ISSN:1029-8479
 608 (cit. on p. 7).
- 609 [13] S. Catani, Y. Dokshitzer, M. Seymour and B. Webber, *Longitudinally invariant K(t) clustering*
 610 *algorithms for hadron-hadron collisions*, *Nuclear Physics B* **406** (1993) 187, URL: <https://www.sciencedirect.com/science/article/pii/055032139390166M>, ISSN:0550-3213 (cit. on
 611 p. 7).
- 613 [14] ATLAS Collaboration, *Identification of boosted, hadronically decaying W bosons and comparisons*
 614 *with ATLAS data taken at $\sqrt{s} = 8 \text{ TeV}$* , *Eur. Phys. J. C* **76** (2016) 154, arXiv: [1510.05821 \[hep-ex\]](https://arxiv.org/abs/1510.05821)
 615 (cit. on p. 7).
- 616 [15] ATLAS Collaboration, *Jet mass reconstruction with the ATLAS Detector in early Run 2 data*,
 617 ATLAS-CONF-2016-035, 2016, URL: <https://cds.cern.ch/record/2200211> (cit. on p. 7).

- [16] ATLAS Collaboration, *Boosted hadronic vector boson and top quark tagging with ATLAS using Run 2 data*, ATL-PHYS-PUB-2020-017, 2020, URL: <https://cds.cern.ch/record/2724149> (cit. on pp. 7, 39).
- [17] J. Thaler and K. Van Tilburg, *Identifying Boosted Objects with N-subjettiness*, **JHEP** **03** (2011) 015, arXiv: [1011.2268 \[hep-ph\]](https://arxiv.org/abs/1011.2268) (cit. on p. 7).
- [18] J. Thaler and L.-T. Wang, *Strategies to Identify Boosted Tops*, **JHEP** **07** (2008) 092, arXiv: [0806.0023 \[hep-ph\]](https://arxiv.org/abs/0806.0023) (cit. on p. 7).
- [19] A. Larkoski, G. Salam and J. Thaler, *Energy Correlation Functions for Jet Substructure*, **JHEP** **06** (2013) 108, arXiv: [1305.0007 \[hep-ph\]](https://arxiv.org/abs/1305.0007) (cit. on p. 7).
- [20] D. Adams and et al., *Recommendations of the Physics Objects and Analysis Harmonisation Study Groups 2014*, ATL-PHYS-INT-2014-018, 2014, URL: <https://cds.cern.ch/record/1743654> (cit. on p. 8).
- [21] *Documentation of the ATLAS AssociationUtils package*, URL: <https://gitlab.cern.ch/atlas/athena/blob/release/21.2.86/PhysicsAnalysis/AnalysisCommon/AssociationUtils/README.rst> (cit. on p. 8).
- [22] J. Gallicchio and Y.-T. Chien, *Quit Using Pseudorapidity, Transverse Energy, and Massless Constituents*, 2018, arXiv: [1802.05356 \[hep-ph\]](https://arxiv.org/abs/1802.05356) (cit. on p. 8).
- [23] A. Hoecker et al., *TMVA - Toolkit for Multivariate Data Analysis*, 2007, arXiv: [physics/0703039 \[physics.data-an\]](https://arxiv.org/abs/physics/0703039) (cit. on p. 12).
- [24] ATLAS Collaboration, *Search for a charged Higgs bosons decaying into a top-quark and a bottom-quark at $\sqrt{s} = 13 \text{ TeV}$ with the ATLAS detector*, **JHEP** **16** (2021) 145, arXiv: [2102.10076 \[hep-ex\]](https://arxiv.org/abs/2102.10076) (cit. on pp. 22, 66).
- [25] *Automatic binning implematation in TTHFitter*. URL: https://indico.cern.ch/event/455289/contributions/1953694/attachments/1209081/1762963/Calvet_binning_Htop_160108.pdf (cit. on pp. 24, 43).
- [26] ATLAS Collaboration, *Luminosity determination in pp collisions at $\sqrt{s} = 13 \text{ TeV}$ using the ATLAS detector at the LHC*, ATLAS-CONF-2019-021, 2019, URL: <https://cds.cern.ch/record/2677054> (cit. on p. 35).
- [27] G. Avoni and et al., *The new LUCID-2 detector for luminosity measurement and monitoring in ATLAS*, **JINST** **13** (2018) P07017 (cit. on p. 35).
- [28] ATLAS Collaboration, *Measurement of the Inelastic Proton–Proton Cross Section at $\sqrt{s} = 13 \text{ TeV}$ with the ATLAS Detector at the LHC*, **Phys. Rev. Lett.** **117** (2016) 182002, arXiv: [1606.02625 \[hep-ex\]](https://arxiv.org/abs/1606.02625) (cit. on p. 35).
- [29] ATLAS Collaboration, *Electron reconstruction and identification in the ATLAS experiment using the 2015 and 2016 LHC proton–proton collision data at $\sqrt{s} = 13 \text{ TeV}$* , **Eur. Phys. J. C** **79** (2019) 639, arXiv: [1902.04655 \[hep-ex\]](https://arxiv.org/abs/1902.04655) (cit. on p. 35).
- [30] ATLAS Collaboration, *Electron and photon performance measurements with the ATLAS detector using the 2015–2017 LHC proton–proton collision data*, **JINST** **14** (2019) P12006, arXiv: [1908.00005 \[hep-ex\]](https://arxiv.org/abs/1908.00005) (cit. on p. 37).
- [31] ATLAS Collaboration, *Jet energy scale measurements and their systematic uncertainties in proton–proton collisions at $\sqrt{s} = 13 \text{ TeV}$ with the ATLAS detector*, **Phys. Rev. D** **96** (2017) 072002, arXiv: [1703.09665 \[hep-ex\]](https://arxiv.org/abs/1703.09665) (cit. on p. 37).

- [32] ATLAS Collaboration, *Determination of jet calibration and energy resolution in proton–proton collisions at $\sqrt{s} = 8\text{ TeV}$ using the ATLAS detector*, (2019), arXiv: [1910.04482 \[hep-ex\]](https://arxiv.org/abs/1910.04482) (cit. on p. 37).
- [33] ATLAS Collaboration, *In situ calibration of large-radius jet energy and mass in 13 TeV proton–proton collisions with the ATLAS detector*, *Eur. Phys. J. C* **79** (2019) 135, arXiv: [1807.09477 \[hep-ex\]](https://arxiv.org/abs/1807.09477) (cit. on pp. 37, 38).
- [34] ATLAS Collaboration, *Measurement of the ATLAS Detector Jet Mass Response using Forward Folding with 80fb^{-1} of $\sqrt{s} = 13\text{ TeV}$ pp data*, ATLAS-CONF-2020-022, 2020, URL: <https://cds.cern.ch/record/2724442> (cit. on p. 38).
- [35] ATLAS Collaboration, *Measurement of b -tagging efficiency of c -jets in $t\bar{t}$ events using a likelihood approach with the ATLAS detector*, ATLAS-CONF-2018-001, 2018, URL: <https://cds.cern.ch/record/2306649> (cit. on p. 39).
- [36] ATLAS Collaboration, *Calibration of light-flavour b -jet mistagging rates using ATLAS proton–proton collision data at $\sqrt{s} = 13\text{ TeV}$* , ATLAS-CONF-2018-006, 2018, URL: <https://cds.cern.ch/record/2314418> (cit. on p. 39).
- [37] ATLAS Collaboration, *Performance of top-quark and W -boson tagging with ATLAS in Run 2 of the LHC*, *Eur. Phys. J. C* **79** (2019) 375, arXiv: [1808.07858 \[hep-ex\]](https://arxiv.org/abs/1808.07858) (cit. on p. 39).
- [38] J. Butterworth et al., *PDF4LHC recommendations for LHC Run II*, *J. Phys. G* **43** (2016) 023001, arXiv: [1510.03865 \[hep-ph\]](https://arxiv.org/abs/1510.03865) (cit. on p. 39).
- [39] ATLAS Collaboration, *Search for charged Higgs bosons decaying into top and bottom quarks at $\sqrt{s} = 13\text{ TeV}$ with the ATLAS detector*, *JHEP* **11** (2018) 085, arXiv: [1808.03599 \[hep-ex\]](https://arxiv.org/abs/1808.03599) (cit. on p. 39).
- [40] ATLAS Collaboration, *ATLAS Pythia 8 tunes to 7 TeV data*, ATL-PHYS-PUB-2014-021, 2014, URL: <https://cds.cern.ch/record/1966419> (cit. on p. 40).
- [41] D. de Florian et al., *Handbook of LHC Higgs Cross Sections: 4. Deciphering the Nature of the Higgs Sector*, (2016), arXiv: [1610.07922 \[hep-ph\]](https://arxiv.org/abs/1610.07922) (cit. on p. 41).
- [42] R. Raitio and W. W. Wada, *Higgs Boson Production at Large Transverse Momentum in QCD*, *Phys. Rev. D* **19** (1979) (cit. on p. 41).
- [43] W. Beenakker and et al., *NLO QCD corrections to t anti- t H production in hadron collisions*, *Nucl. Phys. B* **653** (2003), arXiv: [hep-ph/0211352 \[hep-ph\]](https://arxiv.org/abs/hep-ph/0211352) (cit. on p. 41).
- [44] S. Dawson, C. Jackson, L. H. Orr, L. Reina and D. Wackeroth, *Associated Higgs production with top quarks at the large hadron collider: NLO QCD corrections*, *Phys. Rev. D* **68** (2003), arXiv: [hep-ph/0305087 \[hep-ph\]](https://arxiv.org/abs/hep-ph/0305087) (cit. on p. 41).
- [45] Y. Zhang, W.-G. Ma, R.-Y. Zhang, C. Chen and L. Guo, *QCD NLO and EW NLO corrections to $t\bar{t}H$ production with top quark decays at hadron collider*, *Phys. Lett. B* **738** (2014), arXiv: [1407.1110 \[hep-ph\]](https://arxiv.org/abs/1407.1110) (cit. on p. 41).
- [46] S. Frixione, V. Hirschi, D. Pagani, H.-S. Shao and M. Zaro, *Electroweak and QCD corrections to top-pair hadroproduction in association with heavy bosons*, *JHEP* **06** (2015), arXiv: [1504.03446 \[hep-ph\]](https://arxiv.org/abs/1504.03446) (cit. on p. 41).
- [47] LHCTopWG, *NLO single-top channel cross sections*, 2017, URL: <https://twiki.cern.ch/twiki/bin/view/LHCPhysics/SingleTopRefXsec> (cit. on p. 42).

- 701 [48] A. D. Martin, W. J. Stirling, R. S. Thorne and G. Watt, *Parton distributions for the LHC*, *Eur. Phys.*
 702 *J. C* **63** (2009) 189, arXiv: [0901.0002 \[hep-ph\]](#) (cit. on p. 42).
- 703 [49] A. D. Martin, W. Stirling, R. Thorne and G. Watt, *Uncertainties on α_S in global PDF analyses and*
 704 *implications for predicted hadronic cross sections*, *Eur. Phys. J. C* **64** (2009) 653, arXiv: [0905.3531 \[hep-ph\]](#) (cit. on p. 42).
- 706 [50] M. Aliev et al., *HATHOR – HAdronic Top and Heavy quarks crOss section calculatoR*, *Comput.*
 707 *Phys. Commun.* **182** (2011) 1034, arXiv: [1007.1327 \[hep-ph\]](#) (cit. on p. 42).
- 708 [51] P. Kant et al., *HatHor for single top-quark production: Updated predictions and uncertainty estimates*
 709 *for single top-quark production in hadronic collisions*, *Comput. Phys. Commun.* **191** (2015) 74,
 710 arXiv: [1406.4403 \[hep-ph\]](#) (cit. on p. 42).
- 711 [52] S. Frixione, E. Laenen, P. Motylinski, C. D. White and B. R. Webber, *Single-top hadroproduction in*
 712 *association with a W boson*, *JHEP* **07** (2008) 029, arXiv: [0805.3067 \[hep-ph\]](#) (cit. on p. 42).
- 713 [53] LHCHXSWG1, *Recommended predictions for $t\bar{t}V$ cross sections*, URL: https://twiki.cern.ch/twiki/bin/view/LHCPhysics/LHCHXSWGTT#Plans_for_YR4 (cit. on p. 42).
- 715 [54] J. M. Campbell and R. K. Ellis, *$t\bar{t}W^{+-}$ production and decay at NLO*, *JHEP* **07** (2012), arXiv:
 716 [1204.5678 \[hep-ph\]](#) (cit. on p. 42).
- 717 [55] J. Alwall et al., *The automated computation of tree-level and next-to-leading order differential cross*
 718 *sections, and their matching to parton shower simulations*, *JHEP* **07** (2014) 079, arXiv: [1405.0301 \[hep-ph\]](#) (cit. on p. 42).
- 720 [56] ATLAS PMG Top processes twiki page, URL: <https://twiki.cern.ch/twiki/bin/view/AtlasProtected/PmgTopProcesses> (cit. on p. 42).
- 722 [57] ATLAS Collaboration, *Multi-boson simulation for 13 TeV ATLAS analyses*, ATL-PHYS-PUB-2016-
 723 002, 2016, URL: <https://cds.cern.ch/record/2119986> (cit. on p. 42).

724 Appendices

725 A TOPQ1 DAOD list

726 A.1 Data

727 Table 13 is the TOPQ1 DAOD list for data sample in this analysis.

data15_13TeV.AllYear.physics_Main.PhysCont.DAOD_TOPQ1.grp15_v01_p4513
data16_13TeV.AllYear.physics_Main.PhysCont.DAOD_TOPQ1.grp16_v01_p4513
data17_13TeV.AllYear.physics_Main.PhysCont.DAOD_TOPQ1.grp17_v01_p4513
data18_13TeV.AllYear.physics_Main.PhysCont.DAOD_TOPQ1.grp18_v01_p4513

728 Table 13: TOPQ1 DAOD list for data sample in this analysis.

728 A.2 $t\bar{t}H^+$

729 Table 14 is the TOPQ1 DAOD list for H^+ sample in this analysis.

Nominal
mc16_13TeV.450004.aMcAtNloPythia8EvtGen_A14NNPDF23LO_Hplus4FS_H1000_tb.deriv.DAOD_TOPQ1.e7137_s3126_r9364_p4514
mc16_13TeV.450598.aMcAtNloPythia8EvtGen_A14NNPDF23LO_Hplus4FS_H1200_tb.deriv.DAOD_TOPQ1.e7429_s3126_r9364_p4514
mc16_13TeV.450599.aMcAtNloPythia8EvtGen_A14NNPDF23LO_Hplus4FS_H1400_tb.deriv.DAOD_TOPQ1.e7429_s3126_r9364_p4514
mc16_13TeV.450600.aMcAtNloPythia8EvtGen_A14NNPDF23LO_Hplus4FS_H1600_tb.deriv.DAOD_TOPQ1.e7429_s3126_r9364_p4514
mc16_13TeV.450601.aMcAtNloPythia8EvtGen_A14NNPDF23LO_Hplus4FS_H1800_tb.deriv.DAOD_TOPQ1.e7429_s3126_r9364_p4514
mc16_13TeV.450602.aMcAtNloPythia8EvtGen_A14NNPDF23LO_Hplus4FS_H2000_tb.deriv.DAOD_TOPQ1.e7429_s3126_r9364_p4514
mc16_13TeV.451490.aMcAtNloPythia8EvtGen_A14NNPDF23LO_Hplus4FS_H2500_tb.deriv.DAOD_TOPQ1.e7970_s3126_r9364_p4514
mc16_13TeV.451491.aMcAtNloPythia8EvtGen_A14NNPDF23LO_Hplus4FS_H3000_tb.deriv.DAOD_TOPQ1.e7970_s3126_r9364_p4514
mc16_13TeV.508710.MGPy8EG_A14NNPDF30_Hplus4FS_H4000_tb.deriv.DAOD_TOPQ1.e8276_s3126_r9364_p4514
mc16_13TeV.508711.MGPy8EG_A14NNPDF30_Hplus4FS_H5000_tb.deriv.DAOD_TOPQ1.e8276_s3126_r9364_p4514

728 Table 14: TOPQ1 DAOD list for H^+ sample in this analysis.

730 A.3 $t\bar{t} + \text{jets}$

731 Table 15 is the TOPQ1 DAOD list for $t\bar{t} + \text{jets}$ sample in this analysis.

Nominal
mc16_13TeV.410470.PhPy8EG_A14_ttbar_hdamp258p75_nonallhad.deriv.DAOD_TOPQ1.e6337_s3126_r9364_p4514
mc16_13TeV.410471.PhPy8EG_A14_ttbar_hdamp258p75_allhad.deriv.DAOD_TOPQ1.e6337_s3126_r9364_p4514
mc16_13TeV.411073.PhPy8EG_A14_ttbar_hdamp258p75_ljets_BBFilt.deriv.DAOD_TOPQ1.e6798_s3126_r9364_p4514
mc16_13TeV.411074.PhPy8EG_A14_ttbar_hdamp258p75_ljets_BFiltBBVeto.deriv.DAOD_TOPQ1.e6798_s3126_r9364_p4514
mc16_13TeV.411075.PhPy8EG_A14_ttbar_hdamp258p75_ljets_CFiltBVeto.deriv.DAOD_TOPQ1.e6798_s3126_r9364_p4514
mc16_13TeV.411076.PhPy8EG_A14_ttbar_hdamp258p75_dil_BBFilt.deriv.DAOD_TOPQ1.e6798_s3126_r9364_p4514
mc16_13TeV.411077.PhPy8EG_A14_ttbar_hdamp258p75_dil_BFiltBBVeto.deriv.DAOD_TOPQ1.e6798_s3126_r9364_p4514
mc16_13TeV.411078.PhPy8EG_A14_ttbar_hdamp258p75_dil_CFiltBVeto.deriv.DAOD_TOPQ1.e6798_s3126_r9364_p4514
Reference
mc16_13TeV.410470.PhPy8EG_A14_ttbar_hdamp258p75_nonallhad.deriv.DAOD_TOPQ1.e6337_a875_r9364_p4514
mc16_13TeV.410471.PhPy8EG_A14_ttbar_hdamp258p75_allhad.deriv.DAOD_TOPQ1.e6337_a875_r9364_p4514
mc16_13TeV.411073.PhPy8EG_A14_ttbar_hdamp258p75_ljets_BBFilt.deriv.DAOD_TOPQ1.e6798_a875_r9364_p4514
mc16_13TeV.411074.PhPy8EG_A14_ttbar_hdamp258p75_ljets_BFiltBBVeto.deriv.DAOD_TOPQ1.e6798_a875_r9364_p4514
mc16_13TeV.411075.PhPy8EG_A14_ttbar_hdamp258p75_ljets_CFiltBVeto.deriv.DAOD_TOPQ1.e6798_a875_r9364_p4514
mc16_13TeV.411076.PhPy8EG_A14_ttbar_hdamp258p75_dil_BBFilt.deriv.DAOD_TOPQ1.e6798_a875_r9364_p4514
mc16_13TeV.411077.PhPy8EG_A14_ttbar_hdamp258p75_dil_BFiltBBVeto.deriv.DAOD_TOPQ1.e6798_a875_r9364_p4514
mc16_13TeV.411078.PhPy8EG_A14_ttbar_hdamp258p75_dil_CFiltBVeto.deriv.DAOD_TOPQ1.e6798_a875_r9364_p4514
Alternative
mc16_13TeV.410557.PowhegHerwig7EvtGen_H7UE_tt_hdamp258p75_704_SingleLep.deriv.DAOD_TOPQ1.e6366_a875_r9364_p4514
mc16_13TeV.410558.PowhegHerwig7EvtGen_H7UE_tt_hdamp258p75_704_dil.deriv.DAOD_TOPQ1.e6366_a875_r9364_p4514
mc16_13TeV.411082.PhHerwig7EG_H7UE_ttbar_hdamp258p75_ljets_BBFilt.deriv.DAOD_TOPQ1.e6799_a875_r9364_p4514
mc16_13TeV.411083.PhHerwig7EG_H7UE_ttbar_hdamp258p75_ljets_BFiltBBVeto.deriv.DAOD_TOPQ1.e6799_a875_r9364_p4514
mc16_13TeV.411084.PhHerwig7EG_H7UE_ttbar_hdamp258p75_ljets_CFiltBVeto.deriv.DAOD_TOPQ1.e6799_a875_r9364_p4514
mc16_13TeV.411085.PhHerwig7EG_H7UE_ttbar_hdamp258p75_dil_BBFilt.deriv.DAOD_TOPQ1.e6799_a875_r9364_p4514
mc16_13TeV.411086.PhHerwig7EG_H7UE_ttbar_hdamp258p75_dil_BFiltBBVeto.deriv.DAOD_TOPQ1.e6799_a875_r9364_p4514
mc16_13TeV.411087.PhHerwig7EG_H7UE_ttbar_hdamp258p75_dil_CFiltBVeto.deriv.DAOD_TOPQ1.e6799_a875_r9364_p4514
mc16_13TeV.411088.PhHerwig7EG_H7UE_ttbar_hdamp258p75_allhad_BBFilt.deriv.DAOD_TOPQ1.e6799_a875_r9364_p4514
mc16_13TeV.411089.PhHerwig7EG_H7UE_ttbar_hdamp258p75_allhad_BFiltBBVeto.deriv.DAOD_TOPQ1.e6799_a875_r9364_p4514
mc16_13TeV.411090.PhHerwig7EG_H7UE_ttbar_hdamp258p75_allhad_CFiltBVeto.deriv.DAOD_TOPQ1.e6799_a875_r9364_p4514
mc16_13TeV.410464.aMcAtNloPy8EvtGen_MEN30NLO_A14N23LO_ttbar_noShWe_SingleLep.deriv.DAOD_TOPQ1.e6762_a875_r9364_p4514
mc16_13TeV.410465.aMcAtNloPy8EvtGen_MEN30NLO_A14N23LO_ttbar_noShWe_dil.deriv.DAOD_TOPQ1.e6762_a875_r9364_p4514
mc16_13TeV.410466.aMcAtNloPy8EvtGen_MEN30NLO_A14N23LO_ttbar_noShWe_AllHadronic.deriv.DAOD_TOPQ1.e6762_a875_r9364_p4514
mc16_13TeV.412066.aMcAtNloPy8EG_A14_ttbar_hdamp258p75_ljets_BBFilt.deriv.DAOD_TOPQ1.e7129_a875_r9364_p4514
mc16_13TeV.412067.aMcAtNloPy8EG_A14_ttbar_hdamp258p75_ljets_BFiltBBVeto.deriv.DAOD_TOPQ1.e7129_a875_r9364_p4514
mc16_13TeV.412068.aMcAtNloPy8EG_A14_ttbar_hdamp258p75_ljets_CFiltBVeto.deriv.DAOD_TOPQ1.e7129_a875_r9364_p4514
mc16_13TeV.412069.aMcAtNloPy8EG_A14_ttbar_hdamp258p75_dil_BBFilt.deriv.DAOD_TOPQ1.e7129_a875_r9364_p4514
mc16_13TeV.412070.aMcAtNloPy8EG_A14_ttbar_hdamp258p75_dil_BFiltBBVeto.deriv.DAOD_TOPQ1.e7129_a875_r9364_p4514
mc16_13TeV.412071.aMcAtNloPy8EG_A14_ttbar_hdamp258p75_dil_CFiltBVeto.deriv.DAOD_TOPQ1.e7129_a875_r9364_p4514
mc16_13TeV.411178.PhPy8EG_A14_NNPDF30ME_ttbb_4FS_MS_dilep.deriv.DAOD_TOPQ1.e7818_a875_r9364_p4514
mc16_13TeV.411179.PhPy8EG_A14_NNPDF30ME_ttbb_4FS_MS_lplus.deriv.DAOD_TOPQ1.e7818_a875_r9364_p4514
mc16_13TeV.411180.PhPy8EG_A14_NNPDF30ME_ttbb_4FS_MS_lminus.deriv.DAOD_TOPQ1.e7818_a875_r9364_p4514

Table 15: TOPQ1 DAOD list for $t\bar{t}$ + jets sample in this analysis.

A.4 $t\bar{t}H$

732 Table 16 is the TOPQ1 DAOD list for $t\bar{t}H$ sample in this analysis.

733

Nominal	
mc16_13TeV.346343.PhPy8EG_A14NNPDF23_NNPDF30ME_ttH125_allhad.deriv.DAOD_TOPQ1.e7148_s3126_r9364_p4514	
mc16_13TeV.346344.PhPy8EG_A14NNPDF23_NNPDF30ME_ttH125_semilep.deriv.DAOD_TOPQ1.e7148_s3126_r9364_p4514	
mc16_13TeV.346345.PhPy8EG_A14NNPDF23_NNPDF30ME_ttH125_dilep.deriv.DAOD_TOPQ1.e7148_s3126_r9364_p4514	
Reference	
mc16_13TeV.346343.PhPy8EG_A14NNPDF23_NNPDF30ME_ttH125_allhad.deriv.DAOD_TOPQ1.e7148_a875_r9364_p4514	
mc16_13TeV.346344.PhPy8EG_A14NNPDF23_NNPDF30ME_ttH125_semilep.deriv.DAOD_TOPQ1.e7148_a875_r9364_p4514	
mc16_13TeV.346345.PhPy8EG_A14NNPDF23_NNPDF30ME_ttH125_dilep.deriv.DAOD_TOPQ1.e7148_a875_r9364_p4514	
Alternative	
mc16_13TeV.346443.aMcAtNloPythia8EvtGen_ttH_noShWe_dilep.deriv.DAOD_TOPQ1.e7310_a875_r9364_p4514	
mc16_13TeV.346444.aMcAtNloPythia8EvtGen_ttH_noShWe_semilep.deriv.DAOD_TOPQ1.e7310_a875_r9364_p4514	
mc16_13TeV.346445.aMcAtNloPythia8EvtGen_ttH_noShWe_allhad.deriv.DAOD_TOPQ1.e7310_a875_r9364_p4514	
mc16_13TeV.346346.PhH7EG_H7UE_NNPDF30ME_ttH125_allhad.deriv.DAOD_TOPQ1.e7148_a875_r9364_p4514	
mc16_13TeV.346347.PhH7EG_H7UE_NNPDF30ME_ttH125_semilep.deriv.DAOD_TOPQ1.e7148_a875_r9364_p4514	
mc16_13TeV.346348.PhH7EG_H7UE_NNPDF30ME_ttH125_dilep.deriv.DAOD_TOPQ1.e7148_a875_r9364_p4514	

Table 16: TOPQ1 DAOD list for $t\bar{t}H$ sample in this analysis.

734 **A.5 $t\bar{t}V$**

735 Table 17 is the TOPQ1 DAOD list for $t\bar{t}V$ sample in this analysis.

Nominal	
mc16_13TeV.410155.aMcAtNloPythia8EvtGen_MEN30NLO_A14N23LO_ttW.deriv.DAOD_TOPQ1.e5070_s3126_r9364_p4514	
mc16_13TeV.410156.aMcAtNloPythia8EvtGen_MEN30NLO_A14N23LO_ttZnunu.deriv.DAOD_TOPQ1.e5070_s3126_r9364_p4514	
mc16_13TeV.410157.aMcAtNloPythia8EvtGen_MEN30NLO_A14N23LO_ttZqq.deriv.DAOD_TOPQ1.e5070_s3126_r9364_p4514	
mc16_13TeV.410218.aMcAtNloPythia8EvtGen_MEN30NLO_A14N23LO_ttee.deriv.DAOD_TOPQ1.e5070_s3126_r9364_p4514	
mc16_13TeV.410219.aMcAtNloPythia8EvtGen_MEN30NLO_A14N23LO_ttmumu.deriv.DAOD_TOPQ1.e5070_s3126_r9364_p4514	
mc16_13TeV.410220.aMcAtNloPythia8EvtGen_MEN30NLO_A14N23LO_ttautau.deriv.DAOD_TOPQ1.e5070_s3126_r9364_p4514	
mc16_13TeV.410276.aMcAtNloPythia8EvtGen_MEN30NLO_A14N23LO_tee_mll_1_5.deriv.DAOD_TOPQ1.e6087_s3126_r9364_p4514	
mc16_13TeV.410277.aMcAtNloPythia8EvtGen_MEN30NLO_A14N23LO_ttmumu_mll_1_5.deriv.DAOD_TOPQ1.e6087_s3126_r9364_p4514	
mc16_13TeV.410278.aMcAtNloPythia8EvtGen_MEN30NLO_A14N23LO_ttautau_mll_1_5.deriv.DAOD_TOPQ1.e6087_s3126_r9364_p4514	
Alternative	
mc16_13TeV.410142.Sherpa_NNPDF30NNLO_ttll_mll5.deriv.DAOD_TOPQ1.e4686_s3126_r9364_p4514	
mc16_13TeV.410143.Sherpa_NNPDF30NNLO_ttZnnqq.deriv.DAOD_TOPQ1.e4686_s3126_r9364_p4514	
mc16_13TeV.410144.Sherpa_NNPDF30NNLO_ttW.deriv.DAOD_TOPQ1.e4686_s3126_r9364_p4514	

Table 17: TOPQ1 DAOD list for $t\bar{t}V$ sample in this analysis.

736 **A.6 Single top**

737 Table 18 is the TOPQ1 DAOD list for single top sample in this analysis.

Nominal
mc16_13TeV.410644.PowhegPythia8EvtGen_A14_singletop_schan_lept_top.deriv.DAOD_TOPQ1.e6527_s3126_r9364_p4514
mc16_13TeV.410645.PowhegPythia8EvtGen_A14_singletop_schan_lept_antitop.deriv.DAOD_TOPQ1.e6527_s3126_r9364_p4514
mc16_13TeV.410646.PowhegPythia8EvtGen_A14_Wt_DR_inclusive_top.deriv.DAOD_TOPQ1.e6552_s3126_r9364_p4514
mc16_13TeV.410647.PowhegPythia8EvtGen_A14_Wt_DR_inclusive_antitop.deriv.DAOD_TOPQ1.e6552_s3126_r9364_p4514
mc16_13TeV.410658.PhPy8EG_A14_tchan_BW50_lept_top.deriv.DAOD_TOPQ1.e6671_s3126_r9364_p4514
mc16_13TeV.410659.PhPy8EG_A14_tchan_BW50_lept_antitop.deriv.DAOD_TOPQ1.e6671_s3126_r9364_p4514
Reference
mc16_13TeV.410644.PowhegPythia8EvtGen_A14_singletop_schan_lept_top.deriv.DAOD_TOPQ1.e6527_a875_r9364_p4514
mc16_13TeV.410645.PowhegPythia8EvtGen_A14_singletop_schan_lept_antitop.deriv.DAOD_TOPQ1.e6527_a875_r9364_p4514
mc16_13TeV.410646.PowhegPythia8EvtGen_A14_Wt_DR_inclusive_top.deriv.DAOD_TOPQ1.e6552_a875_r9364_p4514
mc16_13TeV.410647.PowhegPythia8EvtGen_A14_Wt_DR_inclusive_antitop.deriv.DAOD_TOPQ1.e6552_a875_r9364_p4514
mc16_13TeV.410658.PhPy8EG_A14_tchan_BW50_lept_top.deriv.DAOD_TOPQ1.e6671_a875_r9364_p4514
mc16_13TeV.410659.PhPy8EG_A14_tchan_BW50_lept_antitop.deriv.DAOD_TOPQ1.e6671_a875_r9364_p4514
Alternative
mc16_13TeV.410654.PowhegPythia8EvtGen_A14_Wt_DS_inclusive_top.deriv.DAOD_TOPQ1.e6552_s3126_r9364_p4514
mc16_13TeV.410655.PowhegPythia8EvtGen_A14_Wt_DS_inclusive_antitop.deriv.DAOD_TOPQ1.e6552_s3126_r9364_p4514
mc16_13TeV.411032.PowhegHerwig7EvtGen_H7UE_704_tchan_lept_antitop.deriv.DAOD_TOPQ1.e6719_a875_r9364_p4514
mc16_13TeV.411033.PowhegHerwig7EvtGen_H7UE_704_tchan_lept_top.deriv.DAOD_TOPQ1.e6719_a875_r9364_p4514
mc16_13TeV.411034.PhHerwig7EG_H7UE_singletop_schan_lept_top.deriv.DAOD_TOPQ1.e6734_a875_r9364_p4514
mc16_13TeV.411035.PhHerwig7EG_H7UE_singletop_schan_lept_antitop.deriv.DAOD_TOPQ1.e6734_a875_r9364_p4514
mc16_13TeV.411036.PowhegHerwig7EvtGen_H7UE_Wt_DR_inclusive_top.deriv.DAOD_TOPQ1.e6702_a875_r9364_p4514
mc16_13TeV.411037.PowhegHerwig7EvtGen_H7UE_Wt_DR_inclusive_antitop.deriv.DAOD_TOPQ1.e6702_a875_r9364_p4514
mc16_13TeV.412002.aMcAtNloPythia8EvtGen_HThalfscale_tW_inclusive.deriv.DAOD_TOPQ1.e6817_a875_r9364_p4514
mc16_13TeV.412004.aMcAtNloPy8EG_tchan_NLO.deriv.DAOD_TOPQ1.e6888_a875_r9364_p4514

Table 18: TOPQ1 DAOD list for single top sample in this analysis.

738 A.7 tH

739 Table 19 is the TOPQ1 DAOD list for tH sample in this analysis.

Nominal
mc16_13TeV.346676.aMcAtNloPythia8EvtGen_tHjb125_4fl_CPalpha_0.deriv.DAOD_TOPQ1.e7815_a875_r9364_p4514
mc16_13TeV.346678.aMcAtNloPythia8EvtGen_tWH125_4fl_CPalpha_0.deriv.DAOD_TOPQ1.e7816_a875_r9364_p4514

Table 19: TOPQ1 DAOD list for tH sample in this analysis.

740 A.8 Rare t processes

741 Table 20 is the TOPQ1 DAOD list for rare t processes' sample in this analysis.

Nominal
mc16_13TeV.410560.MadGraphPythia8EvtGen_A14_tZ_4fl_tchan_noAllHad.deriv.DAOD_TOPQ1.e5803_s3126_r9364_p4514
mc16_13TeV.410408.aMcAtNloPythia8EvtGen_tWZ_Ztoll_minDR1.deriv.DAOD_TOPQ1.e6423_s3126_r9364_p4514
mc16_13TeV.412043.aMcAtNloPythia8EvtGen_A14NNPDF31_SM4topsNLO.deriv.DAOD_TOPQ1.e7101_a875_r9364_p4514

Table 20: TOPQ1 DAOD list for rare processes' sample in this analysis.

742 A.9 Vector bosons plus jets

743 A.9.1 $W +$ jets

744 Table 21 is the TOPQ1 DAOD list for $W +$ jets sample in this analysis.

Nominal
mc16_13TeV.364170.Sherpa_221_NNPDF30NNLO_Wenu_MAXHTPTV0_70_CVetoBVeto.deriv.DAOD_TOPQ1.e5340_s3126_r9364_p4512
mc16_13TeV.364171.Sherpa_221_NNPDF30NNLO_Wenu_MAXHTPTV0_70_CFilterBVeto.deriv.DAOD_TOPQ1.e5340_s3126_r9364_p4512
mc16_13TeV.364172.Sherpa_221_NNPDF30NNLO_Wenu_MAXHTPTV0_70_BFilter.deriv.DAOD_TOPQ1.e5340_s3126_r9364_p4512
mc16_13TeV.364173.Sherpa_221_NNPDF30NNLO_Wenu_MAXHTPTV70_140_CVetoBVeto.deriv.DAOD_TOPQ1.e5340_s3126_r9364_p4512
mc16_13TeV.364174.Sherpa_221_NNPDF30NNLO_Wenu_MAXHTPTV70_140_CFilterBVeto.deriv.DAOD_TOPQ1.e5340_s3126_r9364_p4512
mc16_13TeV.364175.Sherpa_221_NNPDF30NNLO_Wenu_MAXHTPTV70_140_BFilter.deriv.DAOD_TOPQ1.e5340_s3126_r9364_p4512
mc16_13TeV.364176.Sherpa_221_NNPDF30NNLO_Wenu_MAXHTPTV140_280_CVetoBVeto.deriv.DAOD_TOPQ1.e5340_s3126_r9364_p4512
mc16_13TeV.364177.Sherpa_221_NNPDF30NNLO_Wenu_MAXHTPTV140_280_CFilterBVeto.deriv.DAOD_TOPQ1.e5340_s3126_r9364_p4512
mc16_13TeV.364178.Sherpa_221_NNPDF30NNLO_Wenu_MAXHTPTV140_280_BFilter.deriv.DAOD_TOPQ1.e5340_s3126_r9364_p4512
mc16_13TeV.364179.Sherpa_221_NNPDF30NNLO_Wenu_MAXHTPTV280_500_CVetoBVeto.deriv.DAOD_TOPQ1.e5340_s3126_r9364_p4512
mc16_13TeV.364180.Sherpa_221_NNPDF30NNLO_Wenu_MAXHTPTV280_500_CFilterBVeto.deriv.DAOD_TOPQ1.e5340_s3126_r9364_p4512
mc16_13TeV.364181.Sherpa_221_NNPDF30NNLO_Wenu_MAXHTPTV280_500_BFilter.deriv.DAOD_TOPQ1.e5340_s3126_r9364_p4512
mc16_13TeV.364182.Sherpa_221_NNPDF30NNLO_Wenu_MAXHTPTV500_1000.deriv.DAOD_TOPQ1.e5340_s3126_r9364_p4512
mc16_13TeV.364183.Sherpa_221_NNPDF30NNLO_Wenu_MAXHTPTV1000_E_CMS.deriv.DAOD_TOPQ1.e5340_s3126_r9364_p4512
mc16_13TeV.364156.Sherpa_221_NNPDF30NNLO_Wmumu_MAXHTPTV0_70_CVetoBVeto.deriv.DAOD_TOPQ1.e5340_s3126_r9364_p4512
mc16_13TeV.364157.Sherpa_221_NNPDF30NNLO_Wmumu_MAXHTPTV0_70_CFilterBVeto.deriv.DAOD_TOPQ1.e5340_s3126_r9364_p4512
mc16_13TeV.364158.Sherpa_221_NNPDF30NNLO_Wmumu_MAXHTPTV0_70_BFilter.deriv.DAOD_TOPQ1.e5340_s3126_r9364_p4512
mc16_13TeV.364159.Sherpa_221_NNPDF30NNLO_Wmumu_MAXHTPTV70_140_CVetoBVeto.deriv.DAOD_TOPQ1.e5340_s3126_r9364_p4512
mc16_13TeV.364160.Sherpa_221_NNPDF30NNLO_Wmumu_MAXHTPTV70_140_CFilterBVeto.deriv.DAOD_TOPQ1.e5340_s3126_r9364_p4512
mc16_13TeV.364161.Sherpa_221_NNPDF30NNLO_Wmumu_MAXHTPTV70_140_BFilter.deriv.DAOD_TOPQ1.e5340_s3126_r9364_p4512
mc16_13TeV.364162.Sherpa_221_NNPDF30NNLO_Wmumu_MAXHTPTV140_280_CVetoBVeto.deriv.DAOD_TOPQ1.e5340_s3126_r9364_p4512
mc16_13TeV.364163.Sherpa_221_NNPDF30NNLO_Wmumu_MAXHTPTV140_280_CFilterBVeto.deriv.DAOD_TOPQ1.e5340_s3126_r9364_p4512
mc16_13TeV.364164.Sherpa_221_NNPDF30NNLO_Wmumu_MAXHTPTV140_280_BFilter.deriv.DAOD_TOPQ1.e5340_s3126_r9364_p4512
mc16_13TeV.364165.Sherpa_221_NNPDF30NNLO_Wmumu_MAXHTPTV280_500_CVetoBVeto.deriv.DAOD_TOPQ1.e5340_s3126_r9364_p4512
mc16_13TeV.364166.Sherpa_221_NNPDF30NNLO_Wmumu_MAXHTPTV280_500_CFilterBVeto.deriv.DAOD_TOPQ1.e5340_s3126_r9364_p4512
mc16_13TeV.364167.Sherpa_221_NNPDF30NNLO_Wmumu_MAXHTPTV280_500_BFilter.deriv.DAOD_TOPQ1.e5340_s3126_r9364_p4512
mc16_13TeV.364168.Sherpa_221_NNPDF30NNLO_Wmumu_MAXHTPTV500_1000.deriv.DAOD_TOPQ1.e5340_s3126_r9364_p4512
mc16_13TeV.364169.Sherpa_221_NNPDF30NNLO_Wmumu_MAXHTPTV1000_E_CMS.deriv.DAOD_TOPQ1.e5340_s3126_r9364_p4512
mc16_13TeV.364184.Sherpa_221_NNPDF30NNLO_Wtaunu_MAXHTPTV0_70_CVetoBVeto.deriv.DAOD_TOPQ1.e5340_s3126_r9364_p4512
mc16_13TeV.364185.Sherpa_221_NNPDF30NNLO_Wtaunu_MAXHTPTV0_70_CFilterBVeto.deriv.DAOD_TOPQ1.e5340_s3126_r9364_p4512
mc16_13TeV.364186.Sherpa_221_NNPDF30NNLO_Wtaunu_MAXHTPTV0_70_BFilter.deriv.DAOD_TOPQ1.e5340_s3126_r9364_p4512
mc16_13TeV.364187.Sherpa_221_NNPDF30NNLO_Wtaunu_MAXHTPTV70_140_CVetoBVeto.deriv.DAOD_TOPQ1.e5340_s3126_r9364_p4512
mc16_13TeV.364188.Sherpa_221_NNPDF30NNLO_Wtaunu_MAXHTPTV70_140_CFilterBVeto.deriv.DAOD_TOPQ1.e5340_s3126_r9364_p4512
mc16_13TeV.364189.Sherpa_221_NNPDF30NNLO_Wtaunu_MAXHTPTV70_140_BFilter.deriv.DAOD_TOPQ1.e5340_s3126_r9364_p4512
mc16_13TeV.364190.Sherpa_221_NNPDF30NNLO_Wtaunu_MAXHTPTV140_280_CVetoBVeto.deriv.DAOD_TOPQ1.e5340_s3126_r9364_p4512
mc16_13TeV.364191.Sherpa_221_NNPDF30NNLO_Wtaunu_MAXHTPTV140_280_CFilterBVeto.deriv.DAOD_TOPQ1.e5340_s3126_r9364_p4512
mc16_13TeV.364192.Sherpa_221_NNPDF30NNLO_Wtaunu_MAXHTPTV140_280_BFilter.deriv.DAOD_TOPQ1.e5340_s3126_r9364_p4512
mc16_13TeV.364193.Sherpa_221_NNPDF30NNLO_Wtaunu_MAXHTPTV280_500_CVetoBVeto.deriv.DAOD_TOPQ1.e5340_s3126_r9364_p4512
mc16_13TeV.364194.Sherpa_221_NNPDF30NNLO_Wtaunu_MAXHTPTV280_500_CFilterBVeto.deriv.DAOD_TOPQ1.e5340_s3126_r9364_p4512
mc16_13TeV.364195.Sherpa_221_NNPDF30NNLO_Wtaunu_MAXHTPTV280_500_BFilter.deriv.DAOD_TOPQ1.e5340_s3126_r9364_p4512
mc16_13TeV.364196.Sherpa_221_NNPDF30NNLO_Wtaunu_MAXHTPTV500_1000.deriv.DAOD_TOPQ1.e5340_s3126_r9364_p4512
mc16_13TeV.364197.Sherpa_221_NNPDF30NNLO_Wtaunu_MAXHTPTV1000_E_CMS.deriv.DAOD_TOPQ1.e5340_s3126_r9364_p4512

Table 21: TOPQ1 DAOD list for $W + \text{jets}$ sample in this analysis.

745 A.9.2 $Z + \text{jets}$

746 Table 22 is the TOPQ1 DAOD list for $Z + \text{jets}$ sample in this analysis.

Table 22: TOPQ1 DAOD list for $Z + \text{jets}$ sample in this analysis.

A.10 Diboson

⁷⁴⁷ Table 23 is the TOPQ1 DAOD list for diboson sample in this analysis.

Nominal
mc16_13TeV.364250.Sherpa_222_NNPDF30NNLO_llll.deriv.DAOD_TOPQ1.e5894_s3126_r9364_p4512
mc16_13TeV.364253.Sherpa_222_NNPDF30NNLO_lllv.deriv.DAOD_TOPQ1.e5916_s3126_r9364_p4512
mc16_13TeV.364254.Sherpa_222_NNPDF30NNLO_llvv.deriv.DAOD_TOPQ1.e5916_s3126_r9364_p4512
mc16_13TeV.364255.Sherpa_222_NNPDF30NNLO_lvvv.deriv.DAOD_TOPQ1.e5916_s3126_r9364_p4512
mc16_13TeV.364288.Sherpa_222_NNPDF30NNLO_llll_lowMllPtComplement.deriv.DAOD_TOPQ1.e6096_s3126_r9364_p4512
mc16_13TeV.364289.Sherpa_222_NNPDF30NNLO_lllv_lowMllPtComplement.deriv.DAOD_TOPQ1.e6133_s3126_r9364_p4512
mc16_13TeV.364290.Sherpa_222_NNPDF30NNLO_llvv_lowMllPtComplement.deriv.DAOD_TOPQ1.e6096_s3126_r9364_p4512
mc16_13TeV.363355.Sherpa_221_NNPDF30NNLO_ZqqZv.deriv.DAOD_TOPQ1.e5525_s3126_r9364_p4512
mc16_13TeV.363356.Sherpa_221_NNPDF30NNLO_ZqqZll.deriv.DAOD_TOPQ1.e5525_s3126_r9364_p4512
mc16_13TeV.363357.Sherpa_221_NNPDF30NNLO_WqqZvv.deriv.DAOD_TOPQ1.e5525_s3126_r9364_p4512
mc16_13TeV.363358.Sherpa_221_NNPDF30NNLO_WqqZll.deriv.DAOD_TOPQ1.e5525_s3126_r9364_p4512
mc16_13TeV.363359.Sherpa_221_NNPDF30NNLO_WpqqWmlv.deriv.DAOD_TOPQ1.e5583_s3126_r9364_p4512
mc16_13TeV.363360.Sherpa_221_NNPDF30NNLO_WplvWmqq.deriv.DAOD_TOPQ1.e5983_s3126_r9364_p4512
mc16_13TeV.363489.Sherpa_221_NNPDF30NNLO_WlvZqq.deriv.DAOD_TOPQ1.e5525_s3126_r9364_p4512
mc16_13TeV.363494.Sherpa_221_NNPDF30NNLO_vvvv.deriv.DAOD_TOPQ1.e5332_s3126_r9364_p4512
mc16_13TeV.364283.Sherpa_222_NNPDF30NNLO_llljjj_EW6.deriv.DAOD_TOPQ1.e6055_s3126_r9364_p4512
mc16_13TeV.364284.Sherpa_222_NNPDF30NNLO_lllvjj_EW6.deriv.DAOD_TOPQ1.e6055_s3126_r9364_p4512
mc16_13TeV.364285.Sherpa_222_NNPDF30NNLO_llvvjj_EW6.deriv.DAOD_TOPQ1.e6055_s3126_r9364_p4512
mc16_13TeV.364287.Sherpa_222_NNPDF30NNLO_llvlij_ss_EW6.deriv.DAOD_TOPQ1.e6055_s3126_r9364_p4512
mc16_13TeV.345705.Sherpa_222_NNPDF30NNLO_ggllll_0M41130.deriv.DAOD_TOPQ1.e6213_s3126_r9364_p4512
mc16_13TeV.345706.Sherpa_222_NNPDF30NNLO_ggllll_130M41.deriv.DAOD_TOPQ1.e6213_s3126_r9364_p4512
mc16_13TeV.345723.Sherpa_222_NNPDF30NNLO_ggllvvZZ.deriv.DAOD_TOPQ1.e6213_s3126_r9364_p4512

Table 23: TOPQ1 DAOD list for diboson sample in this analysis.

749 **B Signal/background comparisons**

750 **B.1 BDT input variables**

751 Figures 61(a) to Fig.61(n) compare the shape of the variables included in the BDT for all H^+ signal masses
752 and background.

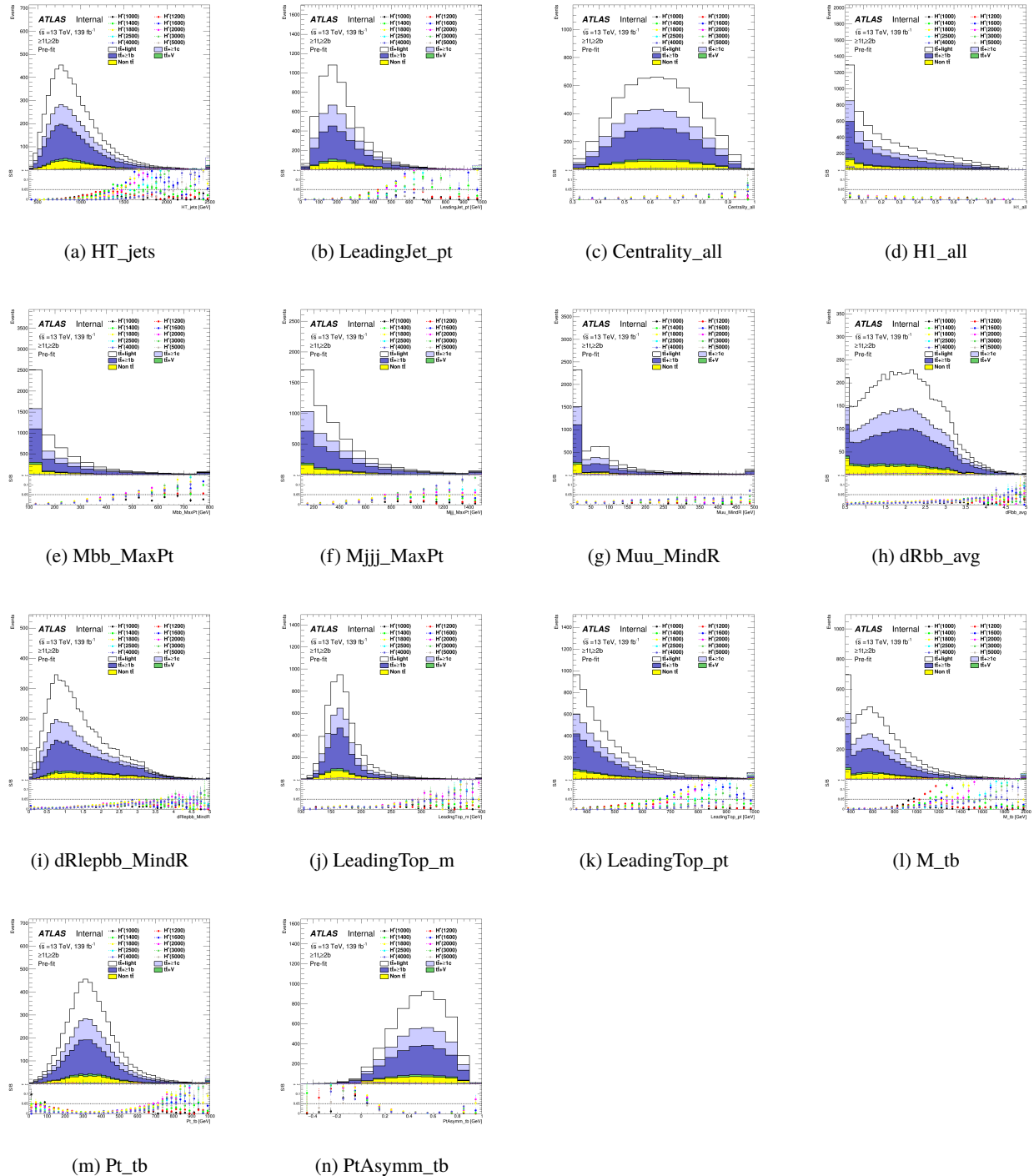


Figure 61: Comparison of the kinematic variables included in the BDT in the SR for the various H^+ signal masses between signal and background.

753 B.2 BDT output

754 Figures 62(a) to Figure 62(j) compare the shape of BDT output distribution in SR region between the
755 signal and background on each H^+ signal mass hypothesis at equal bin intervals.

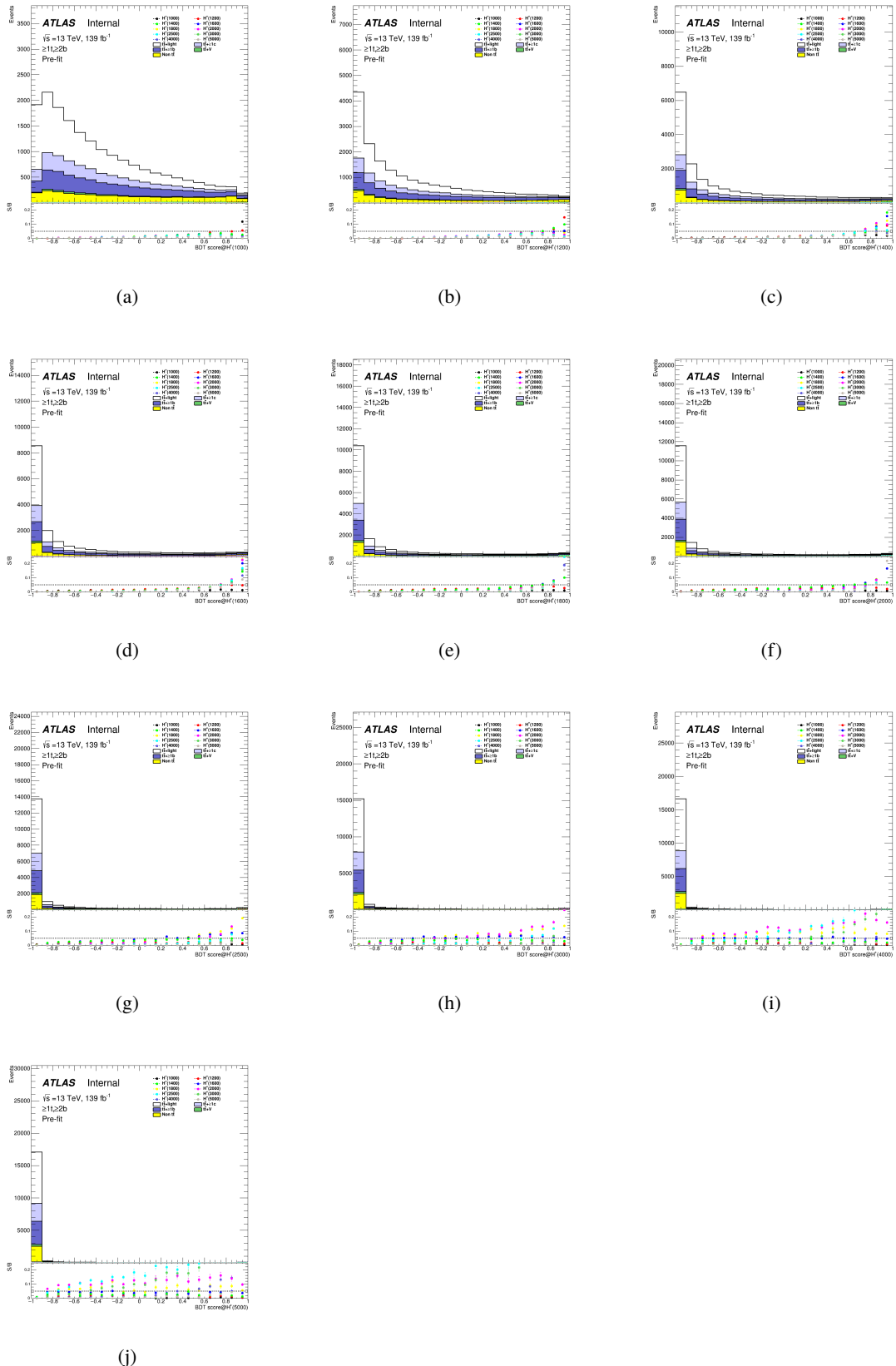


Figure 62

756 Figures 63(a) to Fig.63(j) compare the shape of BDT output distribution in SR region between the signal
757 and background on each H^+ signal mass hypothesis at not equal bin intervals. These binning is optimised
758 using TRExFitter.

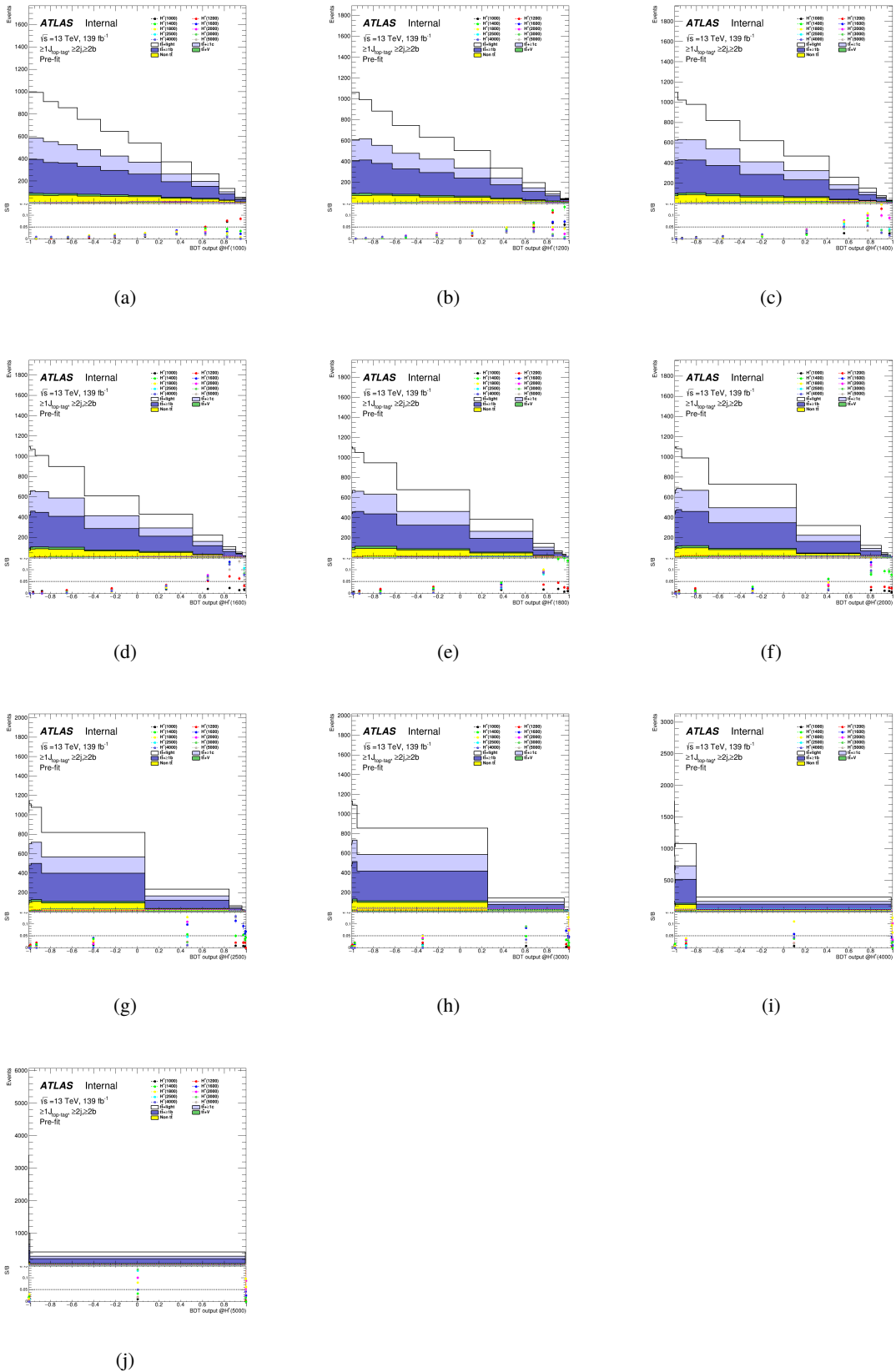


Figure 63

759 Figures 64(a) to Figure 64(j) are BDT output distributions for events used in the derivation of weight factors.
760 These compare the shape of BDT output distribution in SR region between the signal and background on
761 each H^+ signal mass hypothesis at equal bin intervals.

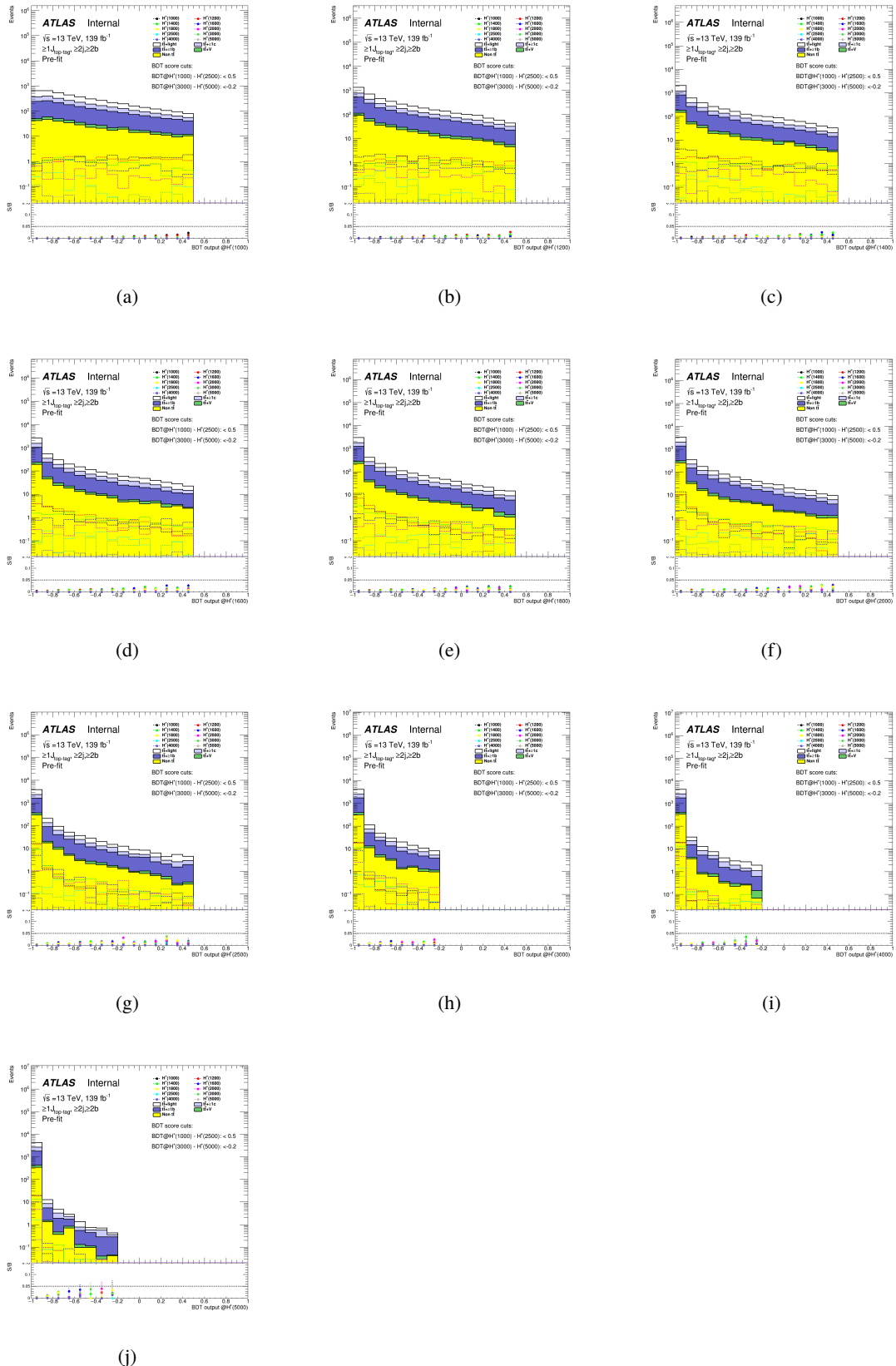


Figure 64

762 **B.3 H_T^{jets} distribution in CR**

763 Figures 65 compare the shape of H_T^{jets} distribution in CR region between the signal and background on
 764 each H^+ signal mass hypothesis at equal bin intervals.

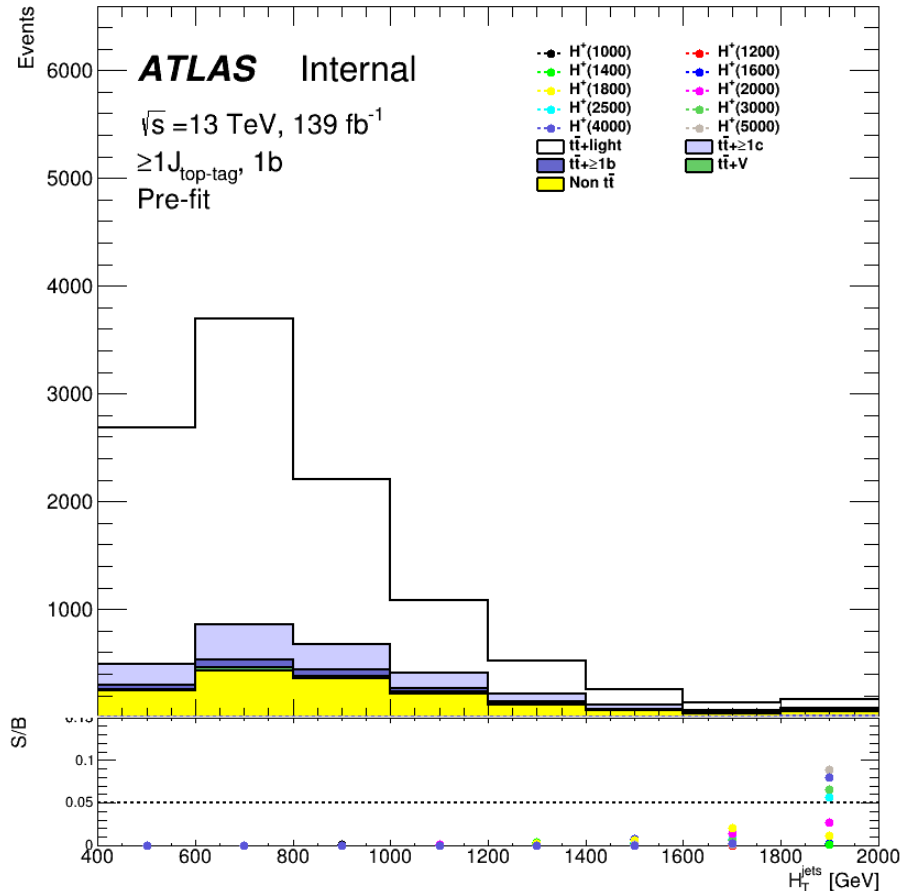


Figure 65: Comparison of the H_T^{jets} in the CR for the various H^+ signal masses between signal and background.

765 **C Pruning**

766 **C.1 Asimov fit**

767 Figures 66 to 72 show the pruning applied in the systematic uncertainties for the Asimov fits for all the H^+
768 mass fits.

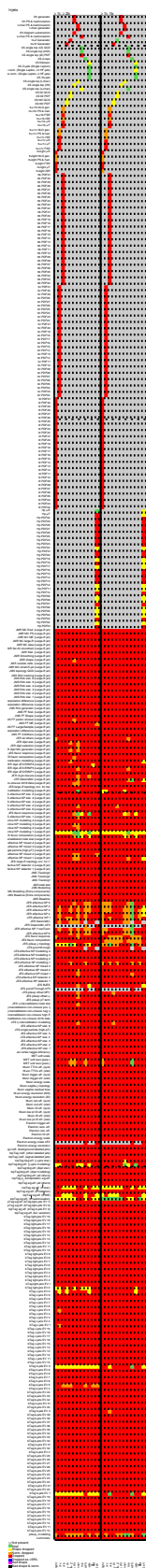


Figure 66: Pruned systematic uncertainties in the 1000 GeV H^+ mass Asimov fits

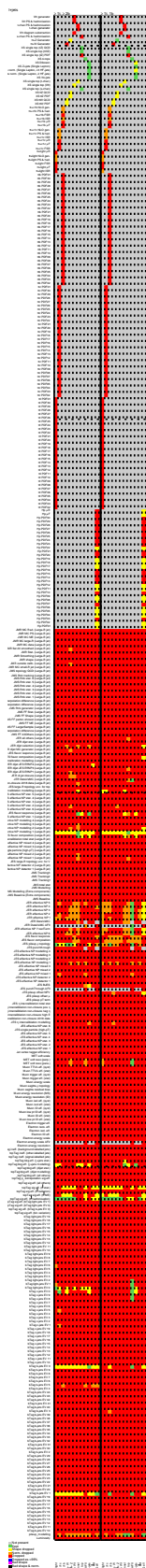


Figure 67: Pruned systematic uncertainties in the 1200 GeV H^+ mass Asimov fits

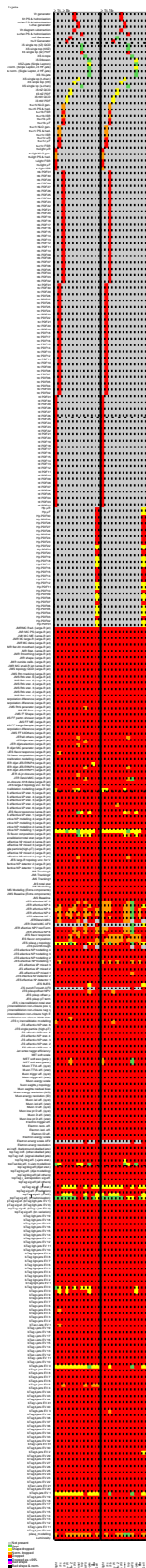


Figure 68: Pruned systematic uncertainties in the 1400 GeV H^+ mass Asimov fits

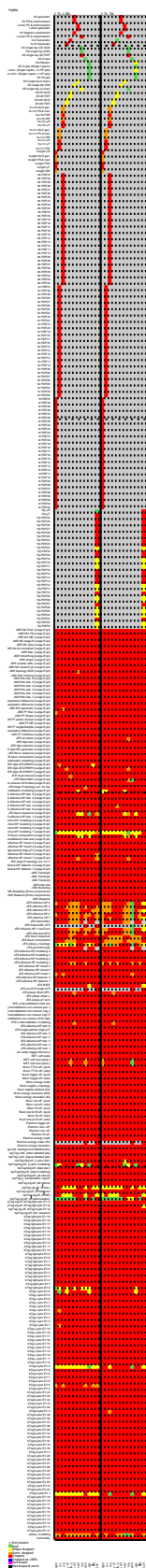


Figure 69: Pruned systematic uncertainties in the 1600 GeV H^+ mass Asimov fits

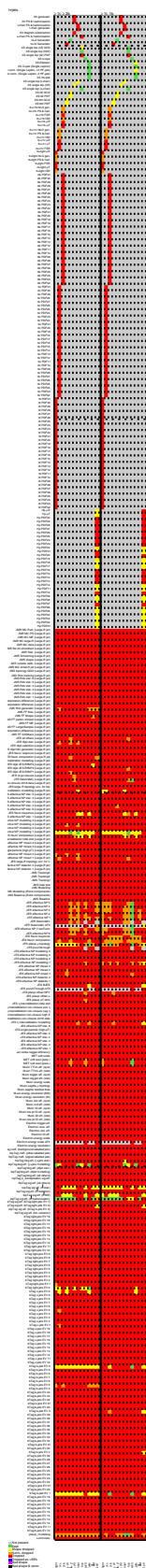


Figure 70: Pruned systematic uncertainties in the 2000 GeV H^+ mass Asimov fits

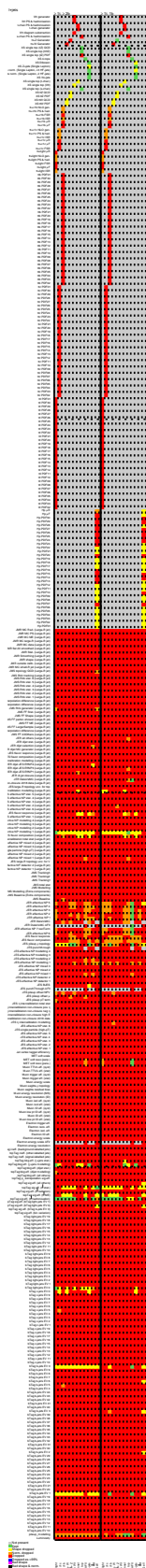


Figure 71: Pruned systematic uncertainties in the 2500 GeV H^+ mass Asimov fits

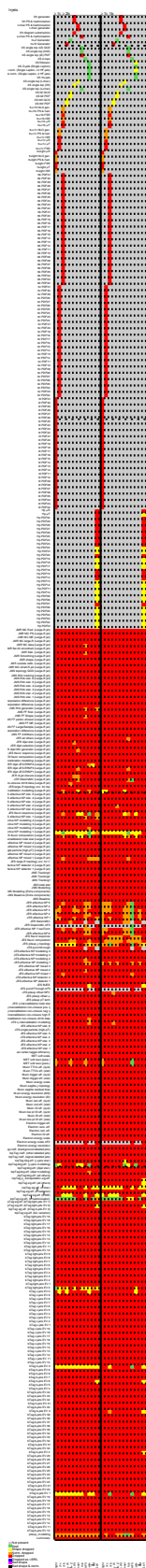


Figure 72: Pruned systematic uncertainties in the 3000 GeV H^+ mass Asimov fits

769 D Studies for systematic uncertainties**770 D.1 Systematics for the composition ratio of $t\bar{t}$ + HF events**

771 This appendix shows the impact of the systematic uncertainty for the composition ratio of $t\bar{t}+ \geq 1b$ and
772 $t\bar{t}+ \geq 1c$ on the extraction of the signal strength in the fitting. To evaluate it, profile likelihood fits were
773 performed using asimov datasets. The fit templates were build from the nominal MC distributions except
774 for the ones of $t\bar{t}+ \geq 1b$ and $t\bar{t}+ \geq 1c$ events. The input distributions of $t\bar{t}+ \geq 1b$ events in the SR and the
775 CR were scaled by 1.20 or 0.80, and the one of $t\bar{t}+ \geq 1c$ sample was scaled by 0.66 (0.95) or 1.34 (1.05) in
776 the SR (CR) to fix the total number of these events. On the other hand, asimov datasets were built from the
777 nominal MC distributions of all background events, that is, the composition ratio of $t\bar{t}+ \geq 1b$ and $t\bar{t}+ \geq 1c$
778 in the asimov datasets is same as the nominal.